



HAL
open science

Can the 2D shallow water equations model flow intrusion into buildings during urban floods?

Benjamin Dewals, Vasileios Kitsikoudis, Miguel Angel Mejía-Morales, Pierre Archambeau, Emmanuel Mignot, Sébastien Proust, Sébastien Erpicum, Michel Pirotton, André Paquier

► To cite this version:

Benjamin Dewals, Vasileios Kitsikoudis, Miguel Angel Mejía-Morales, Pierre Archambeau, Emmanuel Mignot, et al.. Can the 2D shallow water equations model flow intrusion into buildings during urban floods?. *Journal of Hydrology*, 2023, 619, pp.129231. 10.1016/j.jhydrol.2023.129231 . hal-04007606

HAL Id: hal-04007606

<https://hal.inrae.fr/hal-04007606>

Submitted on 28 Feb 2023

HAL is a multi-disciplinary open access archive for the deposit and dissemination of scientific research documents, whether they are published or not. The documents may come from teaching and research institutions in France or abroad, or from public or private research centers.

L'archive ouverte pluridisciplinaire **HAL**, est destinée au dépôt et à la diffusion de documents scientifiques de niveau recherche, publiés ou non, émanant des établissements d'enseignement et de recherche français ou étrangers, des laboratoires publics ou privés.

Journal of Hydrology

Can the 2D shallow water equations model flow intrusion into buildings during urban floods?

--Manuscript Draft--

Manuscript Number:	HYDROL48783R1
Article Type:	Research paper
Keywords:	Experimental hydraulics; Numerical modelling; Open channel flow; Shallow water equations; Turbulence; Urban flood
Corresponding Author:	Vasileios Kitsikoudis University of Twente: Universiteit Twente NETHERLANDS
First Author:	Benjamin Dewals
Order of Authors:	Benjamin Dewals Vasileios Kitsikoudis Miguel Angel Mejía-Morales Pierre Archambeau Emmanuel Mignot Sébastien Proust Sébastien Erpicum Michel Pirotton André Paquier
Abstract:	<p>The multiple flow paths existing in urban environments lead to complex flow fields during urban flooding. Modelling these flow processes with three-dimensional numerical models may be scientifically sound; however, such numerical models are computationally demanding. To ascertain whether urban floods can be modelled with faster tools, this study investigated for the first time the capacity of the 2D shallow water equations (SWE) in modelling the flow patterns within and around urban blocks with openings, i.e., involving flow exchanges between the flows in the streets and within the urban blocks (e.g., through alleys leading to courtyards or through broken windows or doors). Laboratory experiments of idealized urban floods were simulated with two academic 2D SWE models, with their most notable difference being the parameterization of the eddy viscosity. Specifically, the first model had a zero-order turbulence closure while the second model had a second-order depth-averaged $k-\epsilon$ turbulence closure. Thirteen urban layouts were considered with steady flow and five with unsteady flow. Both models simulated the flow depths accurately for the steady cases. The discharge distribution in the streets and the flow velocities were predicted with lower accuracy, particularly in layouts with large open spaces. The average deviation of the modelled discharge distribution at the outlets was 2.5% and 7.3% for the first and second model, respectively. For the unsteady cases, only the first model was tested. It predicted well the velocity pattern during the falling limb of a flood wave, while it did not reproduce all recirculation zones in the rising limb. The peak flow depths in the streets and the peak discharges at the outlets were predicted with an average deviation of 6.7% and 8.6%, respectively. Even though some aspects of the flow in an urban setup are 3D, the findings of this study support the modelling of such processes with 2D SWE models.</p>
Suggested Reviewers:	Matteo Rubinato Coventry University ad2323@coventry.ac.uk Expert on urban hydraulics James Shucksmith The University of Sheffield j.shucksmith@sheffield.ac.uk Jorge Leandro University of Siegen jorge.leandro@uni-siegen.de

	Pierfranco Costabile University of Calabria pierfranco.costabile@unical.it
	Eduardo Martínez-Gomariz Technology Centre for Water eduardo.martinez@cetaqua.com
Response to Reviewers:	Our response to the Reviewers' comments is uploaded in a separate document ("HYDROL48783_Revision_Notes").

Highlights

- In urban floods, urban blocks have flow exchanges with the surrounding streets
- Steady and unsteady 2D SWE numerical simulations of urban floods are presented
- 2D SWE models can model well flow depths and discharge partition in urban floods
- 2D SWE models do not always reproduce accurately the velocity patterns
- Two 2D SWE solvers with different turbulence closure performed similarly well

Declaration of interests

The authors declare that they have no known competing financial interests or personal relationships that could have appeared to influence the work reported in this paper.

The authors declare the following financial interests/personal relationships which may be considered as potential competing interests:

Revision notes for “Can the 2D shallow water equations model flow intrusion into buildings during urban floods?”

We would like to thank the Editor and the three Reviewers for their constructive comments. All comments have been considered when preparing our revised manuscript. Below, we provide a point-by-point response to each comment of the Editor and the Reviewers. Changes made in the manuscript are highlighted in a different color for each Reviewer. Except if otherwise stated, all line numbers mentioned in our responses refer to the revised manuscript with track changes enabled.

Overall, the Abstract, the end of the Introduction and the Conclusion have been rewritten (no track changes for the Introduction and Conclusion Sections, just new text for simplicity) to clarify the novelty of the study and highlight the significance of the findings. Also, the limitations of the study are now better emphasized.

During the revision we additionally made the following minor modifications:

- Minor modifications in the text to improve the clarity at certain points; these modifications are shown with track changes, but they are not color highlighted.
- We corrected the measurement units and some values in Figure 5a. Similarly, we made one small correction in one of the bars in Figure 5c and made the label of the y-axis more informative. The updated values are not much different than the initial values and the analysis in the paper is not affected.
- The Appendix became Supplementary Material in a separate document. In this document, we corrected the units of measurement in Table S1 and we clarified in the caption of Figure S4 that the discharge distribution is presented in % of the total inflow discharge.

EDITOR

Please carefully address all the reviewers' comments. Reviewer #3 points out the lack of novelties that should be clearly emphasized in the Abstract and in the last part of Introduction

A point-by-point response to each comment of the Reviewers is provided hereafter. They have all been addressed.

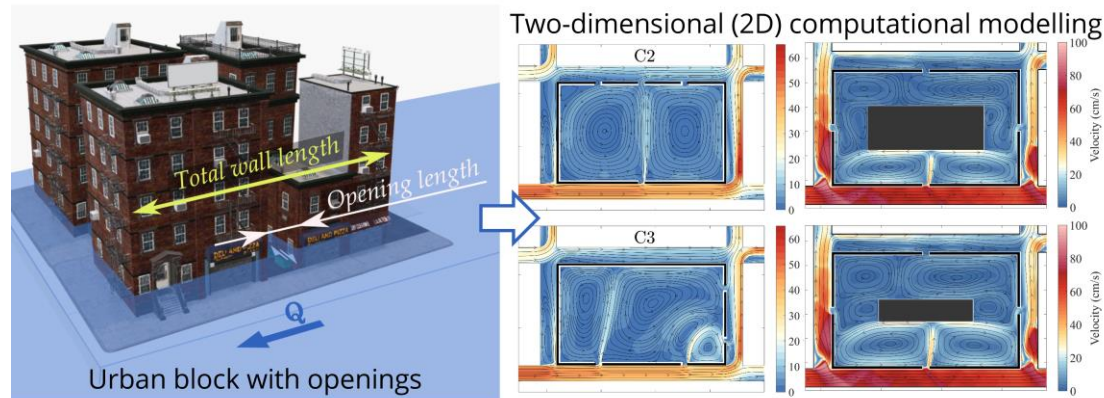
In line with the general comment of Reviewer #3, the Abstract and the end of the Introduction have been entirely rewritten to clarify the novelty of the study and highlight the significance of the findings.

REVIEWER #1

In the manuscript, revisions related to comments by Reviewer #1 are highlighted in **yellow**.

1. As per journal guidelines, graphical abstract is missing.

The following graphical abstract has been added.



2. What is limitation of your study?

Limitations of the study are now better emphasized in the final part of the Conclusion. In the original manuscript, we already highlighted as a limitation the fact that we proved the validity of the 2D modelling only for highly simplified geometric settings: “The geometric configurations considered here are highly simplified compared to real-world urbanized floodplains, which show considerably more intricate geometric features for the street profiles, opening shapes and indoor arrangement of buildings.” (Lines 685-687 in the original manuscript; Lines 705-707 in the revised manuscript).

In the revised manuscript, we additionally point at other processes which are not considered in our study, such as the influence of obstructions near the openings (e.g., parked cars and street furniture), and the interaction of surface flows with surcharging sewers. These limitations are now reported explicitly in Lines 707-711 in the Conclusion of the revised manuscript.

Another major limitation is the absence of comparison of the computational results against real-world data because such data simply do not exist. Therefore, scale effects cannot be assessed, and the transferability of the conclusions across scales (from lab to field scale) remains unknown (Lines 710-711).

Finally, we mention the necessity to further investigate issues which may hinder the operability of flow modelling through building openings, such as the required high mesh density. Therefore, in line with Comment 7 of Reviewer #1, we also suggest investigating the potential of one-dimensional modelling, combined with side-discharge equations, to make valuable predictions of flow intrusion within built-up areas (Lines 715-716).

3. Figures are not properly visible. do replace it by high dpi resolution.

Thank you for noticing this. High resolution files have now been submitted to the system.

4. Any missing data you found in your work?

As detailed in our response to Comment 2 by Reviewer #1, there are currently no data available for assessing the performance of computational models to predict exchanges between streets and urban blocks for realistic urban layouts (i.e., with effects of sidewalks, urban furniture, parked cars, surcharging sewers ...). Such data exist neither at the laboratory scale nor at the field scale.

5. What is the outcome of your study?

The Abstract and the Conclusion have been rewritten to clearly highlight the key findings of the study and their significance. See for instance Lines 30-31 in the revised version of the Abstract, and Lines 682-684 in the Conclusion. In short, this can be summarized in one sentence, which stands now at the end of the revised Abstract:

“Even though some aspects of the flow in an urban setup are 3D, the findings of this study support the modelling of such processes with 2D SWE models”

In addition, a key finding is that the eddy viscosity parameterization is not particularly important in modelling urban floods, as highlighted in Lines 691-694.

6. Have you validated your model by apply or considering sensitivity analysis?

Comprehensive sensitivity analysis has been conducted. The results of the sensitivity analysis are reported in Section 3.1 of the manuscript, as well as in the Supplementary Material (Figures S1 to S3, and Table S1). We tested the sensitivity of the model results to variations in the grid spacing (Section 3.1.1), roughness parameter (Section 3.1.2), downstream boundary conditions (Section 3.1.3), initial conditions (Section 3.1.4) and topographic data (Section 3.1.5).

7. Have you carried out 1D model analysis?

One-dimensional (1D) modelling was not undertaken because we believe that the flow in the considered layouts is nowhere one-dimensional. The relatively short distances between model

inlets, street intersections, openings and model outlets hamper the development of a one-dimensional flow, either in the streets or in the urban block.

Moreover, the specific objective of the present study is to evaluate the performance of two-dimensional (2D) shallow-water models. This is stated in the manuscript title. Therefore, we consider that 1D modelling falls out of the scope of this research.

However, in the revised manuscript, we mention as a perspective the investigation of how a 1D modelling approach could perform in the considered layouts (Lines 715-716):

“The performance of 1D modelling in the streets, combined with side discharge equations for the exchanges through building opening, could also be investigated in a follow-up study.”

8. Add below mentioned references & cite them in your manuscript ... Read thoroughly all the above literature related to flooding (1D, 2D & urban flooding).

We appreciate the Reviewer’s suggestions, but we think that these papers are not directly related to our study since they focus on modelling of rivers and not so much on modelling of urban floods. Therefore, they were not included in the reference list in the revised manuscript.

The following suggested references are river studies, not focused on urban flooding:

Mehta, D. J., Yadav, S. M., Mangukiya, N. K., & Lukhi, Z. (2022). Hydrodynamic Simulation and Dam-Break Analysis Using HEC-RAS 5. In *A System Engineering Approach to Disaster Resilience* (pp. 405-415). Springer, Singapore.

Mehta, D. J., & Kumar, V. Y. (2021). Water productivity enhancement through controlling the flood inundation of the surrounding region of Navsari Purna river, India. *Water Productivity Journal*, 1(2), 11-20.

Chabokpour, J., & Azamathulla, H. M. (2022). Numerical simulation of pollution transport and hydrodynamic characteristics through the river confluence using FLOW 3D. *Water Supply*, 22(10), 7821-7832.

Chabokpour, J., Chaplot, B., Dasineh, M., Ghaderi, A., & Azamathulla, H. M. (2020). Functioning of the multilinear lag-cascade flood routing model as a means of transporting pollutants in the river. *Water Supply*, 20(7), 2845-2857.

Mehta, D. J., & Yadav, S. M. (2020). Hydrodynamic simulation of river Ambica for riverbed assessment: a case study of Navsari Region. In *Advances in Water Resources Engineering and Management* (pp. 127-140). Springer, Singapore.

Mehta, D., Yadav, S. M., Waikhom, S., & Prajapati, K. (2020). Stable channel design of Tapi River using HEC-RAS for Surat Region. In *Environmental processes and management* (pp.

25-36). Springer, Cham.

Mehta, D. J., Eslamian, S., & Prajapati, K. (2022). Flood modelling for a data-scare semi-arid region using 1-D hydrodynamic model: a case study of Navsari Region. *Modeling Earth Systems and Environment*, 8(2), 2675-2685.

This reference is related to flood frequency analysis and, as such, it is also not connected to the hydrodynamics of urban flooding as studied in our research:

Heidarpour, B., Saghafian, B., Yazdi, J., & Azamathulla, H. M. (2017). Effect of extraordinary large floods on at-site flood frequency. *Water Resources Management*, 31(13), 4187-4205.

9. Conclusion is vague. Rewrite it.

The Conclusion has been entirely rewritten and the findings of the study, limitations and future directions are clearly phrased.

REVIEWER #2

In the manuscript, revisions related to comments by Reviewer #2 (in annotated manuscript) are highlighted in blue.

Abstract: Re-write the abstract to view the aim of the current study clearly and to reduce the description of the study details. Moreover, you have to show the important numerical results obtained with statistical indicators that support those results.

In line with a similar suggestion by Reviewer #3, the Abstract has been rewritten to clarify the novelty of the study and highlight the most significant findings. More quantitative results are now reported in the revised version of the Abstract (Lines 26 and 30). These numbers have been also included in the main text.

Moreover, the Abstract has been considerably shortened (by about 20%), as the number of words has been reduced from 384 words to 304 words.

Introduction : You have to reduce the lot of details you have displayed and you have to add other up-to-date references, especially for the recent three years, to the review that you displayed in the introduction in brief.

This comment appeared in the annotated pdf in the second paragraph, but we considered that the comment referred to the whole Introduction Section and not just the second paragraph.

Even though we have already cited several research papers from the last three years in the first part of our Introduction Section, we enriched our cited literature with additional newly published journal articles on urban flood management and vulnerability (Chen et al., 2022; Lv et al., 2022; Qi et al., 2022; Re et al., 2022) and modelling (review of Bates, 2022). Also, some existing citations were also used in the first part of the Introduction Section to provide a more recent link to the literature (Li et al., 2021a). In the literature review for the hydrodynamic aspects of our study, we believe that we have already cited all relevant studies that are directly related to ours (Sections 1.2 and 1.3). Since urban flooding is quite a broad field of research, to cover the studies that are relevant but not directly related to our study, we cited (already from the first submission) some recent literature review papers from high-impact journals (Addison-Atkinson et al., 2022; Guo et al., 2021; Luo et al., 2022; Mignot and Dewals, 2022; Mignot et al., 2019).

Regarding the reduction of the details in our Introduction Section, we believe that inevitably our Introduction has to be relatively long to include a thorough literature review, highlight the relevance of our study with respect to different contexts, and properly identify the existing knowledge gap in the scientific literature. Finally, we moved the last sentence of the first paragraph

to the beginning of the second paragraph to explain more clearly the importance of detailed 2D simulations in urban floods.

Equation (1): You have to cite a reference for each equation used in the current study. Also, you have to define the terms of these equations as they were written in the same form as the equation.

In the revised manuscript, a reference is cited for each equation, as detailed below.

Equation	Reference
(1) and (2)	Wu (2007)
(3) and (4)	Camnasio et al. (2014)
(5)	Idel'cik (1969)
(6)	Yen (2002)
(7)	Roger et al. (2009)
(8) and (9)	Chen et al. (2010)

We believe that all notations used in the equations are properly defined.

Conclusion: Reduce the non-important details that you inserted in this article. Conclusions must meet the aim of the current study directly, and they must display the core of the obtained results.

Consistently with a similar suggestion by Reviewer #1, the Conclusion has been entirely rewritten. Now, it better highlights the specific findings of our research, in a more concise way.

REVIEWER #3

In the manuscript, revisions related to comments by Reviewer #3 are highlighted in **green**.

In the study, the authors conducted many numerical tests of urban floods using two shallow water models. It is hard work. However, a new technique of urban flood modeling has not been found in the study. If the contribution of the study is only to repeat the experimental cases based on two developed numerical models, I cannot recommend the study for publication in the Top 10% ranking journal.

The Abstract and the end of the Introduction have been rewritten to clarify the novelty of the study.

- In the revised manuscript, the following has been added at the end of the Introduction (Lines 158-166):

“In practice, the 2D SWE are used for operational flood hazard and risk modelling. While previous studies have already analysed the ability of the 2D SWE to simulate flow fields in various settings, such as bifurcations, junctions, 4-branch crossroads, and street networks, they all assumed that the street boundaries (i.e., building facades) were impervious. No existing study has focused on the performance of the 2D SWE to predict the flow intrusion into flooded buildings or building blocks, nor on the flow patterns in the streets and within the urban blocks in urban configurations with openings in the building facades.”

The objective of this study is to examine, for the first time, whether the flow patterns within and around porous urban blocks (i.e., with openings) can be ...”

- The revised version of the abstract contains this sentence (Lines 15-19):

“To ascertain whether urban floods can be modelled with faster tools, this study investigated for the first time the capacity of the 2D shallow water equations (SWE) in modelling the flow patterns within and around urban blocks with openings, i.e., involving flow exchanges between the flows in the streets and within the urban blocks (e.g., through alleys leading to courtyards or through broken windows or doors).”

Other comments for the authors are as follows.

1.How to compute the effect of porous block on flow in the two shallow water models? Is the porous shallow water equations solved? The parameter of porosity is not involved in any equation of the study.

The Reviewer is right that porosity parameters are not involved in the equations used in this study. The reason for this is the following:

- In this study, we used the concept of porosity to provide a macroscopic description of the considered geometric layouts (see Fig. 2). A linear porosity ψ (also referred to as conveyance porosity) was used to characterize the portion of openings in the facades (Fig. 2a) and an areal porosity ϕ was used to quantify the void fraction in the urban block internal area (Fig. 2c).
- In contrast, the flow field was fully resolved, i.e., we used a grid spacing which is fine enough to enable the resolution of geometric features of interest.

Although some of the Authors performed past research with porosity shallow-water models (Bruwier et al., 2017; Dewals et al., 2021), this is not the type of flow model used in the present study. To make this perfectly clear in the manuscript, the following sentence has been introduced in Section 2.2 of the revised manuscript (Lines 275-278):

“Note that the concept of porosity is introduced here for the sole purpose of providing a macroscopic description of the considered geometric layouts (Fig. 2), while the flow models used in this study are not porosity shallow-water models (e.g., Dewals et al., 2021). They aim to fully resolve the flow field on the considered computational mesh.”

References

- Bruwier, M., Archambeau, P., Erpicum, S., Piroton, M., & Dewals, B. (2017). Shallow-water models with anisotropic porosity and merging for flood modelling on Cartesian grids. *Journal of hydrology*, 554, 693-709.
- Dewals, B., Bruwier, M., Piroton, M., Erpicum, S., & Archambeau, P. (2021). Porosity Models for Large-Scale Urban Flood Modelling: A Review. *Water*, 13(7), 960.

2. The convergence rate is suggested to be given as the sensitivity of grid spacing is performed.

The sensitivity to grid spacing reported in Section 3.1.1 and in Figure S1 in the Supplementary Material enables confirming the second order accuracy of the finite volume numerical scheme implemented in Model 2, consistently with the linear reconstruction used in this model. This is now explicitly stated in Section 3.1.1 (Lines 411-413) of the revised manuscript.

3. The conservative form of the 2D shallow water equations is commonly written as $\frac{\partial}{\partial x}(\frac{1}{2}u^2 + gh^2/2)$ in x-direction while $\frac{\partial}{\partial y}(\frac{1}{2}v^2 + gh^2/2)$ in y direction.

In the revised manuscript, we have grouped the terms in Eqs. (1) and (2) according to the Reviewer's suggestion.

4. Some typos include.

- (a) "CD w is the weir height" in the description of Eq. (7);
- (b) "(iii) discharge coefficient CD the outlets" in Lines 368 and 369;
- (c) "and CD converged flow" in Line 398;
- (d) ", CD the near field" in Lines 411 and 412;
- (e) "several values of CD depths for Models" in Lines 414 and 415.

We are afraid that there was some issue with the layout in the version of the manuscript made accessible to Reviewer #3. Indeed, as detailed below, we could not find any of the typos pointed at by the Reviewer.

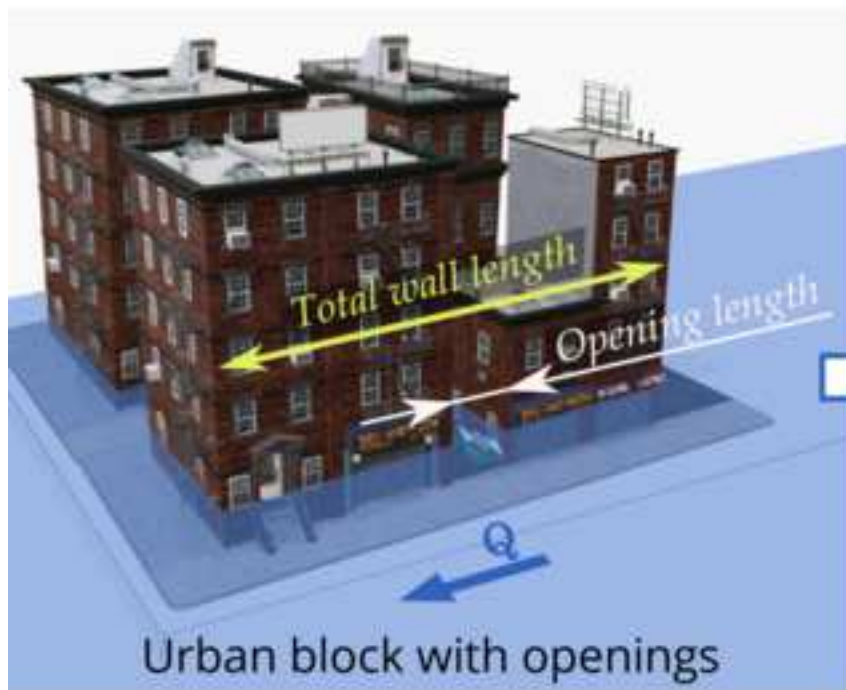
(a) The sentence below Eq. (7) seems correct as it was stated in the original manuscript: "where L is the weir length, C_D is the discharge coefficient, and w is the weir height".

(b) The sentence in Lines 368-369 of the initial submission seems correct as it was stated in the original manuscript: "... (iii) discharge coefficient, C_D , of the weirs at the outlets".

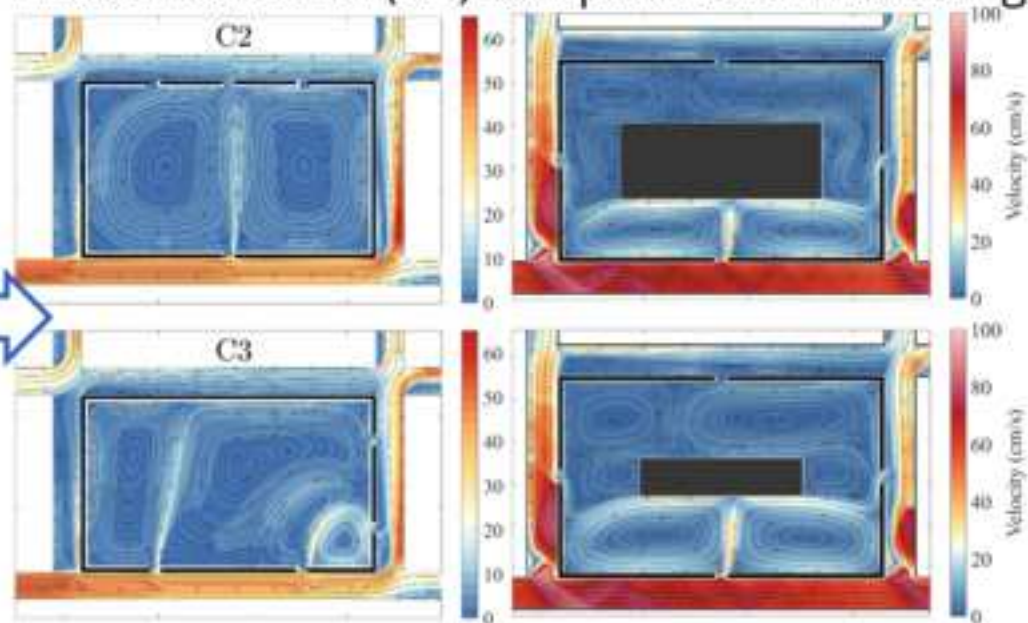
(c) The sentence in Line 398 of the initial submission seems correct as it was stated in the original manuscript: "... and $C_D = 0.527$ for all outlets, with a previously converged flow field as initial condition."

(d) The sentence in Lines 411-412 of the initial submission seems correct as it was stated in the original manuscript: "Hence, the discharge coefficient, C_D , which lumps all flow processes in the near field of the weirs ..."

(e) The sentence in Lines 414-415 of the initial submission seems correct as it was stated in the original manuscript: "To this end, several values of C_D were tested. The lowest difference between modelled and measured flow depths for Model 2 was obtained with $C_D = 0.453$, ..."



Two-dimensional (2D) computational modelling



Abstract

The multiple flow paths existing in urban environments lead to complex flow fields during urban flooding. Modelling these flow processes with three-dimensional numerical models may be scientifically sound; however, such numerical models are computationally demanding. To ascertain whether urban floods can be modelled with faster tools, this study investigated for the first time the capacity of the 2D shallow water equations (SWE) in modelling the flow patterns within and around urban blocks with openings, i.e., involving flow exchanges between the flows in the streets and within the urban blocks (e.g., through alleys leading to courtyards or through broken windows or doors). Laboratory experiments of idealized urban floods were simulated with two academic 2D SWE models, with their most notable difference being the parameterization of the eddy viscosity. Specifically, the first model had a zero-order turbulence closure while the second model had a second-order depth-averaged k - ϵ turbulence closure. Thirteen urban layouts were considered with steady flow and five with unsteady flow. Both models simulated the flow depths accurately for the steady cases. The discharge distribution in the streets and the flow velocities were predicted with lower accuracy, particularly in layouts with large open spaces. The average deviation of the modelled discharge distribution at the outlets was 2.5% and 7.3% for the first and second model, respectively. For the unsteady cases, only the first model was tested. It predicted well the velocity pattern during the falling limb of a flood wave, while it did not reproduce all recirculation zones in the rising limb. The peak flow depths in the streets and the peak discharges at the outlets were predicted with an average deviation of 6.7% and 8.6%, respectively. Even though some aspects of the flow in an urban setup are 3D, the findings of this study support the modelling of such processes with 2D SWE models.

1 Can the 2D shallow water equations model flow intrusion into buildings during urban floods?

2 Benjamin Dewals¹, Vasileios Kitsikoudis², Miguel Angel Mejía-Morales³, Pierre Archambeau¹,

3 Emmanuel Mignot⁴, Sébastien Proust³, Sébastien Erpicum¹, Michel Piroton¹, André Paquier³

4 ¹Hydraulics in Environmental and Civil Engineering, Urban and Environmental Engineering, University
5 of Liege, 4000 Liege, Belgium

6 ²Water Engineering and Management, Faculty of Engineering Technology, University of Twente, 7500
7 AE Enschede, The Netherlands

8 ³UR RiverLy – INRAE, 5 rue de la Doua CS 20244, 69625 Villeurbanne, France

9 ⁴University of Lyon, INSA Lyon, CNRS, LMFA, Ecole Centrale Lyon, Université Claude Bernard
10 Lyon 1, UMR5509, F-69621 Villeurbanne, France

11

12 Abstract

13 The multiple flow paths existing in urban environments lead to complex flow fields during urban flooding.

14 **Modelling these flow processes with three-dimensional numerical models may be scientifically sound;**

15 **however, such numerical models are computationally demanding. To ascertain whether urban floods can**

16 **be modelled with faster tools, this study investigated for the first time the capacity of the 2D shallow water**

17 **equations (SWE) in modelling the flow patterns within and around urban blocks with openings, i.e.,**

18 **involving flow exchanges between the flows in the streets and within the urban blocks (e.g., through alleys**

19 **leading to courtyards or through broken windows or doors).** Laboratory experiments of idealized urban

20 floods were simulated with two academic 2D SWE models, with their most notable difference being the

21 parameterization of the eddy viscosity. Specifically, the first model had a zero-order turbulence closure

22 while the second model had a second-order depth-averaged k - ε turbulence closure. Thirteen urban layouts

23 were considered with steady flow and five with unsteady flow. Both models simulated the flow depths

24 accurately for the steady cases. **The discharge distribution in the streets and the flow velocities were**

25 **predicted with lower accuracy, particularly in layouts with large open spaces. The average deviation of the**

26 **modelled discharge distribution at the outlets was 2.5% and 7.3% for the first and second model,**

27 respectively. For the unsteady cases, only the first model was tested. It predicted well the velocity pattern
28 during the falling limb of a flood wave, while it did not reproduce all recirculation zones in the rising limb.
29 The peak flow depths in the streets and the peak discharges at the outlets were predicted with an average
30 deviation of 6.7% and 8.6%, respectively. Even though some aspects of the flow in an urban setup are 3D,
31 the findings of this study support the modelling of such processes with 2D SWE models.

32 **Keywords**

33 Experimental hydraulics; Numerical modelling; Open channel flow; Shallow water equations;
34 Turbulence; Urban flood

35 **1. Introduction**

36 Urban flood risk is a growing concern (Addison-Atkinson et al., 2022; Chen et al., 2015; Doocy et al.,
37 2013) given the high urbanization rate (Birkmann et al., 2016; Chen et al., 2022; Gross, 2016) and the
38 intense anticipated rainfall events due to climate change (Hettiarachchi et al., 2018; Pfahl et al., 2017;
39 Sanderson et al., 2019). ~~The Flood-flood~~ risk mapping of an urban area remains a challenging task due to
40 the variability in the direct and indirect flood impacts (Kreibich et al., 2014); ~~and~~ in the flood vulnerability
41 (Chen et al., 2019; Huggel et al., 2013; Lv et al., 2022) associated with various socioeconomic contexts in
42 different parts of a city, ~~and as well as~~ due to intricate urban layouts that induce complex flow patterns
43 influencing the flood hazard (Leandro et al., 2016; Li et al., 2021a; Lin et al., 2021). ~~Urban flood numerical~~
44 ~~modelling is a vital component of flood risk assessment~~ (Rosenzweig et al., 2021) ~~and management~~ (Guo
45 et al., 2021; Jongman, 2018), ~~and supports design strategies for sustainable and resilient urban~~
46 ~~infrastructures~~ (Qi et al., 2022; Zhou et al., 2018).

47 Urban flood numerical modelling is a vital component of flood risk assessment (Rosenzweig et al.,
48 2021) and management (Guo et al., 2021; Jongman, 2018), and supports design strategies for sustainable
49 and resilient urban infrastructures (Qi et al., 2022; Zhou et al., 2018). Contrary to one-dimensional (1D)

50 (Kitsikoudis et al., 2020) and 1D-2D (Bates, 2022) simplifications that can be made in river modelling
51 aiming mostly at estimating inundation extents, numerical modelling of multidirectional flows in flooded
52 urban areas should be at least 2D (Li et al., 2021a; Mignot et al., 2006), with a focus on the spatial
53 distribution of not only flow depths but also flow velocities (Kreibich et al., 2009) and specific discharges
54 (Costabile et al., 2020) to express the flood hazard degree in the street network. This is particularly true for
55 large impervious surfaces upstream of and in urban areas that can lead to an excessive amount of runoff,
56 which cannot be conveyed by the drainage systems. Such high flow discharges may threaten the stability
57 of pedestrians (Arrighi et al., 2017; Bernardini et al., 2020; Postacchini et al., 2021; Xia et al., 2014) and
58 can cause the entrainment of vehicles (Martinez-Gomariz et al., 2018; Smith et al., 2019; Xia et al., 2011).
59 Hence, the accurate spatial quantification of hydraulic variables within an urban area is of utmost
60 importance.

61 *1.1. Role of laboratory experiments for model validation*

62 A large number of numerical modelling studies simulated urban flows in real-world cases (Guo et al.,
63 2021; Luo et al., 2022), with some of them using LiDAR data with high-resolution digital elevation models
64 of the urban topography (Almeida et al., 2018; Ozdemir et al., 2013; Yalcin, 2020). However, validation
65 field data including both flow depths and velocities are usually lacking or insufficient (Costabile et al.,
66 2020), which may lead to equifinality issues. Remote sensing techniques can provide inundation extents
67 and water levels, although with certain limitations as tall buildings within the urban environment may
68 obscure some measurements (Neal et al., 2009), but Flow-flow velocity measurements in urban floods are
69 ~~even~~ more challenging. Such measurements are dangerous and can be costly, and as a result, are limited
70 (Brown and Chanson, 2013). Flow depths and surface velocities can alternatively be determined by
71 monitoring parts of a flooded urban area with unmanned aerial vehicles (Perks et al., 2016) and by analyzing
72 existing footage and crowdsourced data from flooded street networks (Mignot and Dewals, 2022; Re et al.,
73 2022). However, there are uncertainties related to the boundary conditions in complex urban terrains with
74 large spatial variability and to the interplay between surface flow and flow in underground drainage systems

75 (Bazin et al., 2014; Chang et al., 2018; Kitsikoudis et al., 2021; Rubinato et al., 2022). Finally, the typically
76 short duration of pluvial flooding and its local character do not allow for detailed measurements over long
77 durations. ~~Numerical modelling studies based on e~~Experimental measurements in laboratory facilities
78 provide an alternative option for models' validation. In carefully designed experiments, the flow and
79 boundary conditions can be accurately controlled (Mignot et al., 2019); ~~and Besides-besides~~ offering a
80 better understanding of the governing physical processes, such studies can contribute to the validation of
81 numerical models, which may subsequently be used for scenario analyses of field cases.

82 *1.2. Performance of 2D shallow water models*

83 The 2D shallow water equations (SWE) can be used to simulate the flow in flooded streets, with
84 typically large width-to-depth ratios. However, at street intersections the interacting flows coming from
85 various branches generate complex patterns (Mignot et al., 2008) and 3D flow structures (El Kadi
86 Abderrezzak et al., 2011; Ramamurthy et al., 2007). While 3D models can capture most features of
87 diverging flows in bifurcations (Mignot et al., 2013; Neary et al., 1999; Ramamurthy et al., 2007) and
88 converging flows in junctions (Huang et al., 2002; Luo et al., 2018; Schindfessel et al., 2015), it is important
89 to examine whether these flow processes can be satisfactorily reproduced by 2D operational models that
90 are much faster than 3D models and can be used for real-time modelling. The 2D SWE approach has been
91 proven capable to replicate experimental measurements of flow depths and discharge partitioning in
92 bifurcations (Bazin et al., 2017; El Kadi Abderrezzak and Paquier, 2009; Khan et al., 2000; Li et al., 2021b;
93 Shettar and Murthy, 1996), in junctions (Li et al., 2021b), in crossroads (Mignot et al., 2008), as well as in
94 larger and more complicated street networks such as that of Arrault et al. (2016) with 49 intersections and
95 that of Li et al. (2021b) with four intersections. Li et al. (2021a) incorporated various urban layouts in their
96 experimental setup and also modelled successfully the flow depths and discharge partition with a 2D SWE
97 model.

98 Despite the successful applications of 2D SWE in modelling water surface profiles and discharge
99 distributions, some open questions remain (Li et al., 2020) regarding the accuracy of 2D SWE in predicting
100 flow velocities in intersections, the extents of recirculating flow areas occurring due to flow separation in
101 some of the branches, and the role of the turbulence closure model (Rodi, 2017). Shettar and Murthy (1996)
102 modelled depth-averaged flow velocities in a bifurcation with a $k-\varepsilon$ turbulence closure and their modelled
103 velocities in the main channel and the length of the recirculation zone agreed well with the experimental
104 measurements. However, their modelled velocities in the branch of the bifurcation were less accurate. Khan
105 et al. (2000) also modelled the flow in a bifurcation but with a mixing length model and reported that the
106 modelled depth-averaged velocities compared well with the measurements, while the dimensions of the
107 recirculation zone were predicted by the model satisfactorily. Bazin et al. (2017) used a constant eddy
108 viscosity model to simulate flows ~~at-in~~ a bifurcation with a branch with a 90 degree angle, with and without
109 obstacles at the intersection, and the modelled depth-averaged flow velocities in the recirculation zone on
110 the upstream side of the bifurcation branch deviated from the measurements. Bruwier et al. (2017) argued
111 that a $k-\varepsilon$ turbulence closure model should be more suitable than a constant eddy viscosity model for
112 modelling flow interactions in intersections, given that since a $k-\varepsilon$ model does not necessarily require
113 calibration, its computational demand can be similar to a constant eddy viscosity model that requires
114 calibration. Arrault et al. (2016) showed in a more complex setup that the turbulence closure model was not
115 particularly influential in the estimation of discharge distribution in the various streets; however, a $k-\varepsilon$
116 turbulence closure model ~~improved-modified~~ significantly the estimates of the recirculation lengths
117 compared to a simulation without a turbulence model. No velocity measurements were available, however,
118 to compare the modelled velocities. More recently, Li et al. (2021a) modelled depth-averaged velocities in
119 an urban district with various urban forms with a $k-\varepsilon$ turbulence closure model and achieved good agreement
120 with surface velocities in areas of flow contraction, however, the results were less accurate in large open
121 areas. Supercritical (Bazin et al., 2017; Mignot et al., 2008) and transcritical (El Kadi Abderrezzak et al.,
122 2011) flows in crossroads may pose additional challenges in 2D SWE models, since the occurrence and
123 structure of hydraulic jumps can significantly affect the discharge partitioning and water surface profiles.

124 *1.3. Flow intrusion into buildings: an extra challenge*

125 Numerical and experimental studies of urban flooding typically consider flow around non-porous
126 residential blocks (Haltas et al., 2016; Van Emelen et al., 2012). However, in reality urban blocks may have
127 corridors leading to backyards, while during intense flooding windows and doors (labeled as "openings" ~~in~~
128 ~~the sequel~~from now on) of buildings may break, leading to lateral flow exchanges between a street and the
129 inside area of the buildings (Mignot et al., 2020) causing significant damages in their interiors (Dottori et
130 al., 2016; Martinez-Gomariz et al., 2021). Mejia-Morales et al. (2021) conducted a systematic experimental
131 analysis of the effect of the location and size of openings in an urban block located within an idealized
132 urban district. They showed that the flow exchanges between the streets and the block interior can alter the
133 flow depth and the flow velocity in the surrounding streets by 12% and 70%, respectively, when compared
134 to a reference case with a non-porous block. Besides the recent study of Mejia-Morales et al. (2021), there
135 is only a limited number of studies that investigated how the porosity of urban blocks affects the hydraulic
136 characteristics of a flood. Mignot et al. (2020) measured the flow discharge entering a building through an
137 open door, window, or gate in case of an urban flood, and they noticed that in some cases the intruding
138 discharge can be approximated by formulas for side weirs. However, the authors also observed that this
139 intruding discharge can be significantly affected by surrounding urban obstacles. Wüthrich et al. (2020)
140 showed with a flume experiment how the hydrostatic force and the form drag exerted by a steady flow on
141 a building are modified by the porosity and the orientation of the building, while Sturm et al. (2018)
142 measured the flood impact forces on physical models of buildings with openings on a torrential fan. In other
143 experiments, Liu et al. (2018) showed how the orientation of a house with respect to the incoming flow
144 affects the forcing on the house door for a dam-break case and Zhou et al. (2016) found differences in the
145 wakes of simplified porous and non-porous buildings. In a numerical study of a torrential flood, Gems et
146 al. (2016) modelled how the different openings of a building affect the flow pattern within its interior, the
147 associated hydrodynamic forcing, and the near-building flow pattern. The findings of these studies show
148 that the openings in buildings affect the spatial distribution of flood hazard and thus the number and types

149 of openings should be considered in flood modelling. ~~However, this adds up to the already complex urban~~
150 ~~flow processes, and it is important to ascertain whether 2D SWE can capture properly these additional~~
151 ~~effects.~~

152 1.4. Objective of the study

153 ~~The flow exchanges between a street and the interior of a building, in combination with bifurcations~~
154 ~~and junctions at crossroads, lead to complex and potentially 3D flow patterns around urban blocks during~~
155 ~~urban floods. Since urban areas are typically densely populated, there is a need for fast computational tools~~
156 ~~that could be utilized for real-time modelling of not only the flow depths but also the flow velocities for the~~
157 ~~accurate estimation of the flood hazard. 3D numerical models can potentially capture the flow processes of~~
158 ~~urban floods; however, they are computationally demanding and slow for real-time modelling. In practice,~~
159 ~~the 2D SWE are used for operational flood hazard and risk modelling. While previous studies have already~~
160 ~~analysed the ability of the 2D SWE to simulate flow fields in various settings, such as bifurcations,~~
161 ~~junctions, 4-branch crossroads, and street networks, they all assumed that the street boundaries (i.e.,~~
162 ~~building facades) were impervious. No existing study has focused on the performance of the 2D SWE to~~
163 ~~predict the flow intrusion into flooded buildings or building blocks, nor on the flow patterns in the streets~~
164 ~~and within the urban blocks in urban configurations with openings in the building facades.~~

165 The objective of this study is to examine ~~for the first time~~ whether the flow patterns within and around
166 porous urban blocks ~~(i.e., with openings)~~ can be ~~quickly and efficiently accurately~~ predicted with numerical
167 modelling based on 2D SWE and to determine what is the most effective modelling strategy for the accurate
168 estimation of flow velocities and flow depths. To this end, the experiments of Mejia-Morales et al. (2021)
169 and Mejia-Morales et al. (2022a) for flow around and within a porous urban block are replicated using two
170 different academic numerical modelling tools to investigate the importance of eddy viscosity
171 parameterization on the accuracy of the models. Complementary steady flow experiments with additional
172 geometric configurations are also presented for the first time, based on the same experimental approach as

173 Mejia-Morales et al. (2021). The paper is organized as follows: in Section 2, the experimental procedure is
174 briefly described, and the numerical models are presented. The new experimental results and the results of
175 the numerical modelling are presented and discussed in Section 3. Finally, conclusions are drawn in
176 Section 4.

177 2. Experiments and numerical modelling

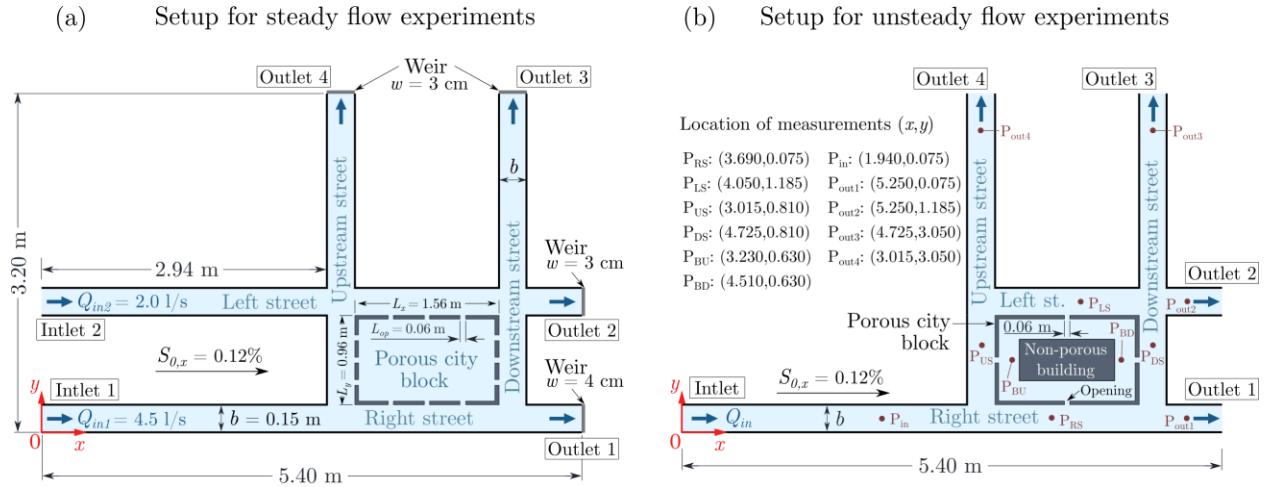
178 This section presents the experimental setup (Section 2.1), the various porous urban block
179 configurations that were tested (Section 2.2), the numerical models that were used to simulate the
180 experimental data (Section 2.3), ~~as well as~~and the prescribed boundary and initial conditions (Section 2.4).
181 Both steady and unsteady flow conditions were simulated with the numerical models. For steady flow
182 conditions, the experimental data are a combination of the data presented by Mejia-Morales et al. (2021)
183 and new data collected from the same urban physical model in the same facility. For unsteady flow
184 conditions, the experimental data of Mejia-Morales et al. (2022a) are used. Only a brief overview of the
185 experimental setup and methods is provided here since they are described in detail in the aforementioned
186 papers.

187 2.1. Experimental setup

188 Mejia-Morales et al. (2021) and Mejia-Morales et al. (2022a) experimentally investigated urban floods
189 at the city block scale using a physical model of a rectangular urban block surrounded by four streets, under
190 steady (Figure 1a) and unsteady (Figure 1b) flow conditions. For the steady flow experiments, the length
191 of the two streets in the x -direction (named “Right Street” and “Left Street”) was 5.4 m and the length of
192 the two streets in the y -direction (named “Downstream Street” and “Upstream Street”) was 3.2 m. All four
193 streets had the same rectangular cross section with a width $b = 0.15$ m. The experimental setup for the
194 unsteady flow experiments was the same, except for the initial part of the Left Street, which was closed
195 upstream of the Upstream Street (Figure 1b). The physical model had a slope $S_{0,x} = 0.12\%$ in the x
196 direction and $S_{0,y} = 0\%$ in the y direction, whereas the bed of the model was constructed with PVC and

197 the sidewalls of the streets, and the urban block were constructed with plastic. Various configurations of
198 the urban block were tested (Section 2.2 and Figure 2); however, its total lengths in the x and y directions
199 remained fixed at $L_x = 1.56$ m and $L_y = 0.96$ m, respectively, while the thickness and the height of the
200 walls of the porous block were 2 cm and 15 cm, respectively.

201 The model inlets were located at the upstream ends of the streets in the x direction. As such, the steady
202 flow experiments had two inlets with fixed inlet discharges Q_{in_1} and Q_{in_2} for the Right Street and Left Street,
203 respectively, while for the unsteady experiments discharge was fed only through the Right Street since the
204 upstream reach of the Left Street was closed. The inlet discharges were measured using separate valve-
205 flowmeter systems with an accuracy of 3%. Smooth inlet conditions were secured by placing a plastic
206 honeycomb grid at the point entrance of the Right Street and of the Left Street. Each one of the four streets
207 of the physical model had an outlet with a vertical tail weir that regulated the flow depth. For the steady
208 flow cases, the weir height of Outlet 1 in the Right Street was 4 cm and of Outlet 2 in the Left Street was
209 3 cm, with respective outlet discharges Q_{out_1} and Q_{out_2} . In the two streets in the y direction, the Outlet 3 in
210 the Downstream Street and the Outlet 4 in the Upstream Street had the same 3 cm weir height, with outlet
211 discharges Q_{out_3} and Q_{out_4} , respectively. For the unsteady flow cases, the weir height was set to zero in all
212 outlets to avoid the reflection of the floodwaves on the weir. The outflow discharges at the four outlets were
213 monitored using electromagnetic flowmeters. Specifically, the water overflowing the weir in each outlet
214 was collected in a separate tank and subsequently the flow exiting each tank was measured with an
215 OPTIFLUX 2000 flowmeter, manufactured by KROHNE.



217

218 **Figure 1.** (a) Experimental setup for the steady flow experiments (adapted from Mejia-Morales et al.
 219 (2021)) and (b) experimental setup for the unsteady flow experiments (adapted from Mejia-Morales et al.
 220 (2022a)). In (b) the locations of measurements denote the points where flow depths were recorded for the
 221 whole duration of the hydrograph.

222 The flow depths in the physical model were measured using ultrasonic distance-measuring sensors
 223 (BAUMER UNDK 20I6914/S35A) with a 0.65 mm uncertainty. For the steady flow cases, a sensor was
 224 attached on a mechanical gantry system that allowed horizontal movement, with measurements being taken
 225 every 5 cm along the longitudinal direction of each street and at three locations across the street width with
 226 6.5 cm spacing. Flow depth measurements within the porous urban block were conducted every 12 cm in
 227 both x and y directions. Each depth measurement was conducted with a sampling frequency of 50 Hz for a
 228 duration of 50 s (Mejia-Morales et al., 2021). For the unsteady flow cases, flow depths were measured at
 229 the eleven locations depicted in Figure 1b for the whole duration of each hydrograph. The reported flow
 230 depths are the results of ensemble averaging of 50 identical floodwaves that were fed sequentially into the
 231 model, with a steady base flow separating two sequential floodwaves. The number of required repeated
 232 floodwaves was selected by increasing the number until the ensemble average standard deviation of the
 233 flow depth became smaller than 1 mm. The floodwaves characteristics are detailed in Section 2.4.

234 For the steady flow cases, surface flow velocities were measured using large-scale particle image
235 velocimetry (LSPIV) (Fujita et al., 1998). Floating wood shavings (1 - 4 mm) were used as tracers. A
236 Panasonic HC-V770 camera was positioned 2.8 m above the physical model, monitoring the plan view at
237 a rate of 25 frames per second with a resolution of 1920 px by 1080 px. The time-averaged surface
238 velocities estimated by the LSPIV technique stabilized after different periods of time for the various areas
239 of the model, but none of them exceeded 60 s (Mejia-Morales et al., 2021). More details about the seeding
240 of the flow, the flow monitoring, the data post-processing, and a validation of the LSPIV measurements
241 against measurements with an acoustic Doppler velocimeter (ADV) are provided in Mejia-Morales et al.
242 (2021).

243 For the unsteady flow cases, it was not feasible to monitor the flow velocities in the whole flow area.
244 Only the surface velocities within the porous block and at two points in the Right Street and Left Street
245 (shown in Figure 1b) were monitored. Moreover, an ensemble average was not used for the LSPIV due to
246 prohibitive post-processing load (Mejia-Morales et al., 2022a). A Sony ZV-1 camera with a sampling rate
247 of 25 frames per second was used and the collected frames were averaged over periods of 2 seconds to filter
248 the data.

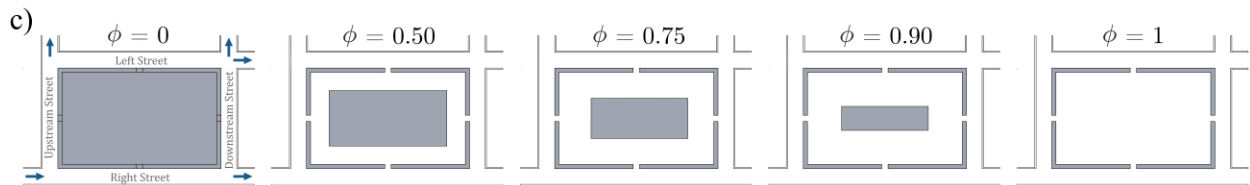
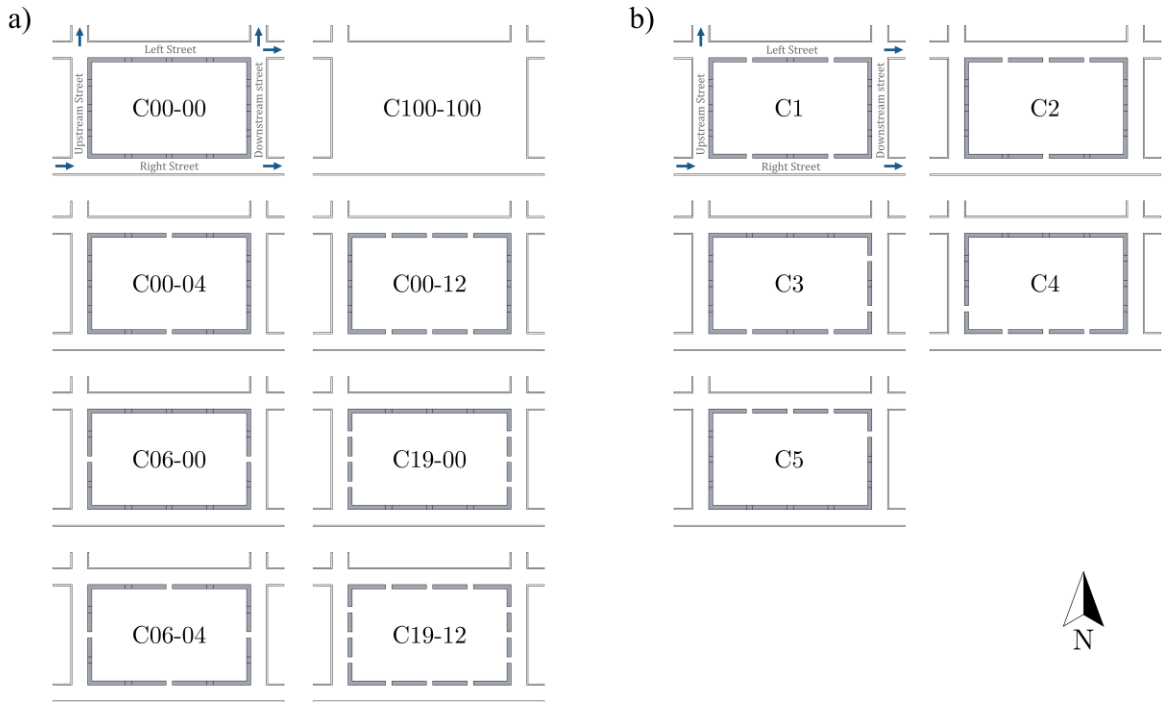
249 2.2. *Urban block configurations*

250 In every experiment, the urban block was in the same position near the downstream end in the x
251 direction and had the same dimensions L_x and L_y (Figure 1). However, the conveyance porosity (i.e., the
252 porosity of each sidewall of the urban block), ψ , as defined by the number and locations of openings,
253 differed in each experiment. Each opening had a width $L_{op} = 6$ cm ~~and each sidewall of the block had with~~
254 no more than three openings ~~per sidewall of the block~~. In all tests, the water surface elevation remained
255 lower than the height of the openings. In the present paper, three series of configurations for the porous
256 block are examined (Figure 2):

- 257
- The first series comprises the eight configurations presented by Mejia-Morales et al. (2021) without obstruction within the block (Figure 2a). The conveyance porosity of each configuration is presented as C_{xx-yy} , where xx and yy denote the ratio of the total length of the openings in a side of the porous block to the length of that side, in percent, in the x and y directions, respectively. The locations of the openings in the configuration with the largest conveyance porosity (C19-12) are shown in Figure 1a. The conveyance porosity in the rest of the configurations is determined by closing some of the openings of C19-12, while maintaining symmetry in the porous block openings.
- 264
- The second series comprises five new configurations, constructed and tested with the same experimental approach as Mejia-Morales et al. (2021), also without obstructions within the block (Figure 2b). The common trait of these configurations is that each configuration has four openings in its perimeter (the remaining ones after blocking eight openings in C19-12 shown in Figure 1a). Since there is no symmetry in every configuration, these configurations are simply named C1 – C5 in order of appearance.
- 270
- The configurations in the third series, presented in Mejia-Morales et al. (2022a), have one opening in the middle of each wall of the block and a non-porous rectangular obstacle in the center of the block. The footprint area of this obstacle was varied as shown in Figure 2c, leading to an areal porosity, ϕ_a , for each case that is determined as the ratio of the empty area within the block to its total internal area.

275 **Note that the concept of porosity is introduced here for the sole purpose of providing a macroscopic**
276 **description of the considered geometric layouts (Figure 2), while the flow models used in this study are not**
277 **porosity shallow-water models (e.g., Dewals et al. (2021)). They aim to fully resolve the flow field on the**
278 **considered computational mesh.**

279 The first and second series were used with steady flow conditions, while the third series was used with
280 both steady and unsteady flow conditions. Details about the upstream boundary conditions of each case are
281 presented in Section 2.4.



284 **Figure 2.** (a) Geometric configurations of the porous block of Mejia-Morales et al. (2021) with steady flow
 285 (series 1), (b) new geometric configurations of the porous block with steady flow (series 2), and
 286 (c) geometric configurations of the porous block with steady and unsteady flow (series 3). The arrows in
 287 the first geometric configuration of each subfigure show the flow direction in each street around the porous
 288 block and they are the same for the rest of the geometric configurations in each subfigure. In (a), the
 289 conveyance porosity, ψ , of each sidewall of each configuration is given by C_{xx-yy} , where xx and yy denote
 290 the ψ value in percent in the x and y directions, respectively. In (b), due to lack of symmetry in every case,
 291 the naming of the configurations is simply in order of appearance. In (c), the symbol ϕ denotes the areal
 292 porosity of the porous block as defined by the ratio of the empty space within the block to its total internal
 293 area. The grey rectangles in the center of the blocks in subfigure (c) denote solid non-porous obstacles. ~~The~~
 294 ~~arrow at the top right points to the North.~~ The blocks in (a) and (b) were tested in the experimental setup of
 295 Figure 1a and the blocks in (c) were tested in the experimental setup of Figure 1b.

296 The physical models were designed by assuming a geometrically distorted scale, with horizontal and
 297 vertical scale ratios equal to 50 and 10, respectively. This means that a studied flow in the physical model

298 may be interpreted as a representation of a real-world flow in streets with 7.5 m in width around an urban
 299 block with dimensions 78 m \times 48 m and openings 3 m wide. The upscaled studied flow depths are around
 300 60 cm. This approach ensures relatively large depths in the physical model to enable a satisfactory
 301 measurement accuracy (Heller, 2011; Li et al., 2021b).

302 2.3. Numerical modelling

303 The laboratory experiments were simulated using two academic numerical codes that solve the 2D
 304 SWE equations. The two models have differences in their mathematical formulation and their numerical
 305 discretization. The first model is implemented in the software Rubar20 (Mignot et al., 2008) developed by
 306 the Riverly research unit of Inrae in Lyon and the second one is implemented in Wolf 2D (Epicum et al.,
 307 2009) developed by the HECE group at the University of Liege. Table 1 provides an overview of the
 308 characteristics of each model, referred to as Model 1 for Rubar20 and Model 2 for Wolf 2D. The steady
 309 flow cases were simulated with both numerical models, while only Model 1 was used for the simulation of
 310 the unsteady flow cases.

311 **Table 1.** Details of the tested numerical models.

	Model 1	Model 2
Software	Rubar 20	Wolf 2D
Reference	Mignot et al. (2008)	Epicum et al. (2009)
Turbulence closure	Elder's formula (zero-order model)	Depth-averaged $k-\varepsilon$ model
Friction formula	Explicit Colebrook-White (Yen, 2002) (Eq. (6))	Colebrook-White (Eq. (5))
Numerical scheme	Godunov type	Flux-vector splitting

312

313 2.3.1. Governing equations

314 The two codes solve the conservative form of the 2D SWE, which means that the main unknowns are
 315 the flow depth, h , and the specific discharges, hu and hv , with u and v denoting the depth-averaged flow

316 velocities along the x and y direction, respectively. The 2D SWE in conservative form are written as follows
 317 (Wu, 2008):

$$\frac{\partial hu}{\partial t} + \frac{\partial}{\partial x} \left(hu^2 + \frac{gh^2}{2} \right) + \frac{\partial hv}{\partial y} = \frac{\tau_{bx}}{\rho} + \frac{1}{\rho} \frac{\partial h\tau_{xx}}{\partial x} + \frac{1}{\rho} \frac{\partial h\tau_{xy}}{\partial y} \quad (1)$$

$$\frac{\partial hv}{\partial t} + \frac{\partial huv}{\partial x} + \frac{\partial}{\partial y} \left(hv^2 + \frac{gh^2}{2} \right) = \frac{\tau_{by}}{\rho} + \frac{1}{\rho} \frac{\partial h\tau_{xy}}{\partial x} + \frac{1}{\rho} \frac{\partial h\tau_{yy}}{\partial y} \quad (2)$$

318 where g is the acceleration of gravity, ρ is the water density, t is the time, τ_{xx} , τ_{yy} , and τ_{xy} are the depth-
 319 averaged stresses comprising both the Reynolds and molecular stresses (Ercicum et al., 2009), and τ_{bx} and
 320 τ_{by} are the bed shear stresses in the x and y direction, respectively, calculated from Eqs. (3) and (4) in line
 321 with Camnasio et al. (2014):

$$\frac{\tau_{bx}}{\rho} = f \frac{u\sqrt{u^2 + v^2}}{8} \quad (3)$$

$$\frac{\tau_{by}}{\rho} = f \frac{v\sqrt{u^2 + v^2}}{8} \quad (4)$$

322 where f is the Darcy-Weisbach bed friction coefficient.

323 The Darcy-Weisbach formulation is used in both models, but the friction coefficient f of the bottom
 324 and side-walls is estimated by the Colebrook-White formula (Eq. (5)) (Idel'cik, 1969) in Model 2 and by
 325 its explicit equivalent formula (Eq. (6)) (Yen, 2002) in Model 1.

$$\frac{1}{\sqrt{f}} = -2 \log \left(\frac{k_s}{14.8h} + \frac{2.51}{\text{Re}\sqrt{f}} \right) \quad (5)$$

326

$$f = \frac{1}{4} \left[-\log \left(\frac{k_s}{12h} + \frac{6.79}{\text{Re}^{0.9}} \right) \right]^{-2} \quad (6)$$

327 where k_s is the roughness height and Re is a Reynolds number $\text{Re} = 4\sqrt{u^2 + v^2}h/\nu$ with ν the kinematic
 328 viscosity of water.

329 Although both models were derived by depth-averaging the Reynolds-averaged Navier-Stokes
330 equations, together with Boussinesq's assumption for expressing the depth-averaged turbulent stresses, they
331 differ by the type of turbulence closure used. Model 1 is based on a zero-order turbulence closure, in which
332 the eddy viscosity, ν_t , is estimated by Elder's formula: $\nu_t = \lambda h u_*$, with u_* the friction velocity computed
333 from the free surface slope and λ a parameter set by the user with a default value of 1 (Mejia-Morales et
334 al., 2020). In Model 2, a second-order turbulence closure is implemented. It consists in a two-length-scale
335 depth-averaged k - ϵ turbulence model, as detailed by Ercicum et al. (2009) and Camnasio et al. (2014).

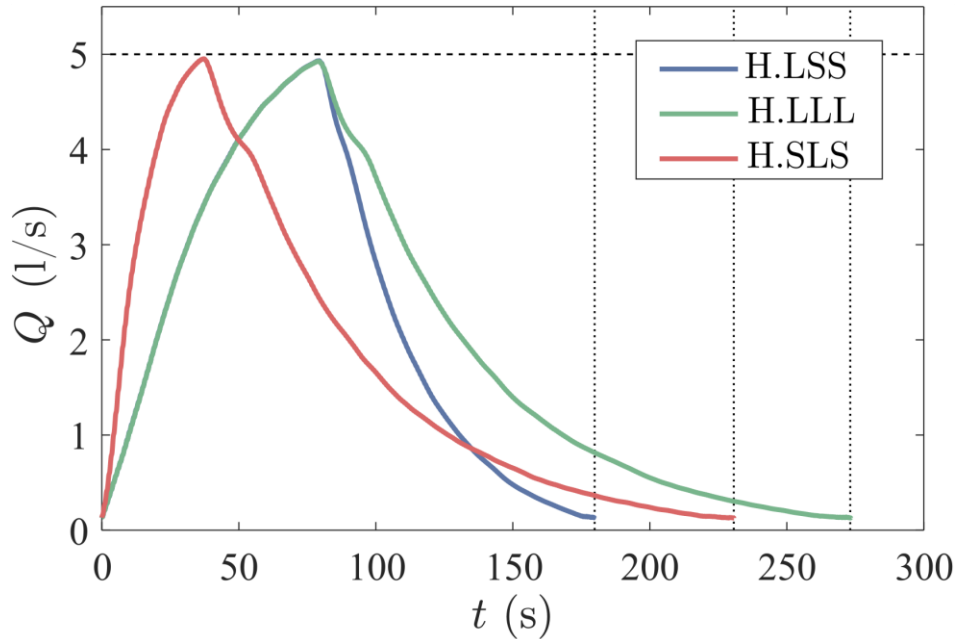
336 *2.3.2. Numerical discretization*

337 In both models, the computational domain was meshed with a Cartesian square grid aligned with the
338 street sidewalls. Depending on the model run, the grid spacing, Δx , was varied between 5 mm and 30 mm
339 with the resulting ratio of the grid size to the length of one opening in the porous block, L_{op} , ranging from
340 1/2 to 1/12. Both models are solved with a finite volume technique. In Model 1, a Godunov type scheme is
341 used (Mignot et al., 2008), while Model 2 is based on a flux-vector splitting technique (Ercicum et al.,
342 2010). In both models, the variables at the cell edges are evaluated from a linear reconstruction, achieving
343 second-order accuracy in space. For steady flow calculations, the models are run in unsteady mode until a
344 steady state is reached. The time step used in the simulations is of the order of 10^{-3} seconds, as it is
345 constrained by the Courant-Friedrichs-Lewy stability condition.

346 *2.4. Boundary and initial conditions*

347 The computational domain was delimited by three types of boundaries: sidewalls, inlets, and outlets.
348 At each sidewall, the component of the specific discharge normal to the sidewall was set to zero. At the
349 inlets, the specific discharge in the streamwise direction was prescribed, and the normal component of the
350 specific discharge was set to zero. The two inlets that are considered in the Left Street and Right Street
351 were positioned at a distance of 2.94 m upstream of the uppermost street intersections (Figure 1), i.e., at the
352 location of the honeycomb grid at the entrance of each street in the experiments.

353 For the steady flow cases in the first and second series of tests (Figure 2a and b), steady inflow
354 discharges were prescribed: $Q_{in_1} = 4.5$ l/s and $Q_{in_2} = 2.0$ l/s (Figure 1) in consistency with the measured
355 values. For the unsteady flow cases in the third test series (Figure 2c), the inflow discharge was fed only
356 through the Right Street as a sequence of 50 consecutive identical flood waves. Three different floodwaves
357 were tested (Figure 3) and each one was examined separately. Each floodwave had the same peak flow of
358 5 l/s (Figure 3) but was characterized by a different unsteadiness degree (Mejia-Morales et al., 2022a). The
359 floodwaves were distinguished based on the rising discharge time, the falling discharge time, and the total
360 volume of floodwater, ~~and~~ while their names were formed by using an “L” or an “S” for large and small
361 magnitude for each one of the floodwave characteristics, respectively. For example, H.LSS denotes a
362 hydrograph with large rising discharge time, small falling discharge time, and small total volume of
363 floodwater. As a reference case, steady flow experiments with inlet discharge of 5 l/s (i.e., equal to the peak
364 of the floodwaves) through the Right Street were also carried out in the geometrical setup of test series 3
365 (Figure 1b with the urban blocks of Figure 2c).



367

368 **Figure 3.** Unsteady hydrographs used as inlet discharge in the Right Street (Figure 1b) for the porous blocks
 369 of Figure 2c.

370 At the outlets, the outflow discharge was prescribed as a function of the computed flow depth. The
 371 outlet boundaries were positioned as follows (Figure 1):

- 372 • in the Right Street and the Left Street, at a distance of 0.6 m downstream of the easternmost street
 373 intersection.
- 374 • in the Upstream Street and the Downstream Street, at 1.94 m downstream of the northernmost street
 375 intersection.

376 For test series 1 and 2 (Figure 2a and b), the outflow discharge, Q_0 , in each outlet was determined from
 377 the following weir formula (e.g., Roger et al. (2009)):

$$Q_0 = LC_D \sqrt{2g(h-w)^3} \quad (7)$$

378 where L is the weir length, C_D is the discharge coefficient, and w is the weir height.

379 The implementation of Eq. (7) is slightly different in the two models:

- 380 • in Model 1, the value of L is set equal to the mesh size, and distinct values of Q_0 are computed at
381 each cell edge along the outlet boundary; as a function of the flow depth computed at [the](#) relevant
382 cell;
- 383 • in Model 2, the length L is taken equal to the actual weir length (i.e., the street width b) and a single
384 value of Q_0 is evaluated, assumed uniformly distributed over the weir length, as a function of the
385 average of the computed flow depths over the cells next to the outlet boundary.

386 For test series 3 (Figure 2c), the downstream boundary condition was set to critical flow for all the
387 edges of an outlet because the flow goes directly from the street to the outlet tank without a weir.

388 In ~~most~~ [the](#) steady flow runs of Model 2, the initial condition was [either a converged solution from a](#)
389 [previous run or](#) a calm body of water; with an initial flow depth equal to 0.05 m. ~~The~~ [For Model 1, the](#)
390 initial condition [for the steady flow calculations was a water level close to the experimental value and](#) for
391 the unsteady flow calculations was zero flow depth across the flow domain.

392 3. Results and discussion

393 3.1. Sensitivity analysis and calibration of the numerical models

394 Model 2 was used systematically in a series of preliminary computations to assess the effect of the
395 variation in the (i) grid spacing, Δx , (ii) roughness height, k_s , (iii) discharge coefficient, C_D , of the weirs at
396 the outlets, and (iv) initial conditions. Model 1 was also used in these preliminary computations, but not in
397 a systematic way. Moreover, Model 1 was used to verify whether considering a theoretical bottom
398 topography (flat bed) instead of the real one influences the results. These sensitivity analyses were
399 conducted for a single geometric configuration (C19-12 in Figure 2a), which includes the largest number
400 of openings and leads to the most complex flow fields. The comparison of the computed, y_i^c , and observed,
401 y_i^o , hydraulic variables was carried out based on the bias and the root mean square error (RMSE) (e.g.,
402 [Chen et al. \(2010\)](#)):

$$\text{bias} = \frac{\sum_{i=1}^N (y_i^c - y_i^o)}{N} \quad (8)$$

403

$$\text{RMSE} = \sqrt{\frac{\sum_{i=1}^N (y_i^c - y_i^o)^2}{N}} \quad (9)$$

404 where N is the number of points where both measured and modelled data were available.

405 3.1.1. Grid spacing

406 The grid cell size for Model 2 was selected after repeating the computations for C19-12 three times
 407 with all parameters being kept the same except the grid cell size. The three mesh grids that were tested had
 408 square grid cells with side length, Δ , equal to 30 mm, 10 mm, and 5 mm, respectively. The bias and RMSE
 409 of the flow depths and velocities for different areas of the model were significantly reduced when the grid
 410 cell size was reduced from 30 mm to 10 mm but did not vary much when the cell size was further reduced
 411 from 10 mm to 5 mm (Figure S1a in the Supplementary Material). **Figure S1a in the Supplementary**
 412 **Material also confirms the second order accuracy of the finite volume numerical scheme implemented in**
 413 **Model 2, consistently with the linear reconstruction used in this model.**

414 However, the features of the simulated flow velocity patterns (i.e., number and size of recirculating
 415 flow areas) within the porous block were more consistent with the features of the measured patterns when
 416 the cell size was 5 mm (Figure S2a in the Supplementary Material), even though some flow recirculations
 417 were not captured entirely. Therefore, the 5 mm cell size was kept for the rest of the analyses with Model 2.

418 Model 1 exhibited similar behavior with Model 2 when varying the cell size with the rest of the
 419 parameters being kept the same, however, with Model 1 the flow velocity patterns were ~~identical~~ similar
 420 for mesh sizes of 10 mm and 5 mm (Figure S3a in the Supplementary Material). Thus, to reduce
 421 computational times, the 10 mm mesh was kept for the rest of the analyses with Model 1.

422 With these mesh configurations, the computed flow depths exhibited a systematic bias compared to the
423 observations, which motivated the extension of the sensitivity analysis to the roughness height and the
424 discharge coefficients of the weir outlets.

425 3.1.2. Roughness height

426 The roughness height was taken at a small value corresponding to the PVC surface of the laboratory
427 model. The tested values of k_s were equal to 2×10^{-4} m, 8×10^{-5} m, and 3.6×10^{-5} m. This sensitivity
428 analysis was conducted with Model 2, with $\Delta x = 5$ mm and $C_D = 0.527$ for all outlets, with a previously
429 converged flow field as initial condition. The three tested values for the roughness height did not affect
430 significantly the flow depths and velocities results (Figure S1b in the Supplementary Material) nor the flow
431 patterns (Figure S2b in the Supplementary Material). The flow depth bias and RMSE values for the lowest
432 value of k_s were slightly lower compared to the other k_s values, but at the same time the flow velocity bias
433 and RMSE values slightly increased. The k_s value of 3.6×10^{-5} m was calibrated from water surface
434 measurements in a single street without openings. Considering the very small influence of the tested k_s
435 values on the simulated results with Model 2, a similar sensitivity analysis was not repeated with Model 1
436 and $k_s = 3.6 \times 10^{-5}$ m was used in both models.

437 3.1.3. Discharge coefficient of the weirs

438 The computations presented in Section 3.1.1 used discharge coefficients that were experimentally
439 derived from the laboratory tests. However, the location where the flow depth is measured upstream of the
440 weirs in the lab does not correspond exactly to the location where the Model 2 considers flow depth for
441 estimating the outflow discharge. Hence, the discharge coefficient, C_D , which lumps all flow processes in
442 the near field of the weirs (including vertical acceleration, which cannot be represented explicitly by shallow
443 water equations) was recalibrated so that the computed flow depths agree on average with the observations.
444 To this end, several values of C_D were tested. The lowest difference between modelled and measured flow
445 depths for Model 2 was obtained with $C_D = 0.453$, and thus this value was selected for the rest of the
446 numerical simulations using Model 2. For Model 1, the lowest difference between modelled and measured

447 flow depths was obtained with $C_D = 0.467$ and this value was chosen for the rest of the simulations with
448 Model 1, although a value of 0.55 for Outlets 1 and 2 and 0.53 for Outlets 3 and 4 led to a better distribution
449 of the outflows. This was also the case for all the urban blocks in Figure 2a. Nevertheless, the effect of C_D
450 on the street and block intrusion discharges and on the flow patterns (Figure S2c and Figure S3b in the
451 Supplementary Material) is rather small. The small difference between the chosen discharge coefficients
452 for the two models may be attributed to the different ways that the downstream boundary conditions were
453 implemented in the models and to the different turbulent closures.

454 *3.1.4. Initial conditions*

455 A converged solution for a steady flow simulation may depend on the initial conditions (Dewals et al.,
456 2012), particularly in the presence of complex patterns of recirculating flow. Therefore, by using Model 2
457 for the case with the C19-12 block (Figure 2a), we repeated the computations for two different initial
458 conditions: (i) the computed steady flow field obtained with the experimentally derived discharge
459 coefficient (i.e., a previously converged solution) and (ii) water at rest with flow depth equal to 5 cm. As
460 expected, the initial condition ~~influences~~ influenced the computed steady flow field. For the flow in the
461 porous block, the results obtained when the computations were initiated with water at rest agree better with
462 the observations (Figure S1c and Figure S2d in the Supplementary Material). This initial condition setting
463 ~~is was~~ kept for the rest of the analysis for Model 2 ~~and also~~ while the initial condition for Model 1 was a
464 water level close to the experimental value. For Model 1 the results were generally independent of the initial
465 conditions, but exceptions could be found for the more complex patterns inside the block.

466 The simulation parameters obtained from the sensitivity analysis are summarized in Table 2 and these
467 parameters were used for the numerical modelling of the rest of the experimental configurations.

468 **Table 2.** Calibrated parameters used for the numerical modelling of all cases.

	Model 1	Model 2
Cell size, Δx	10 mm	5 mm
Initial conditions	Water level close to experimental value	Water at rest
Roughness height, k_s	3.6×10^{-5} m	3.6×10^{-5} m
Outlet weirs discharge coefficient, C_D	0.467	0.453

469

470 *3.1.5. Topography*

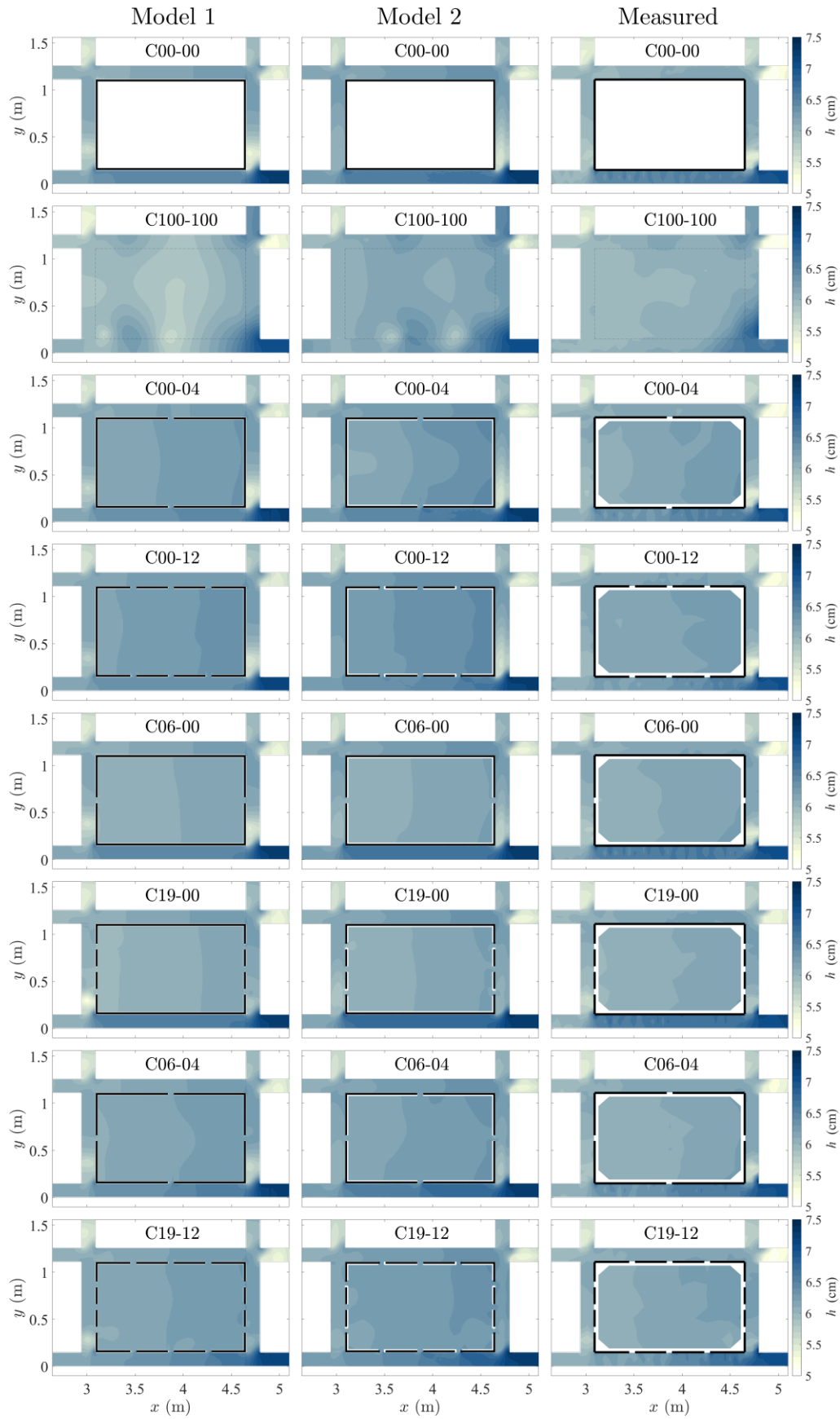
471 The topography of the experimental platform may change in time since it was constructed with boards
 472 supported by beams. For most numerical calculations, the theoretical topography of an inclined plane with
 473 a constant slope in the x direction of 0.12% was used. However, two detailed topographies that were
 474 surveyed in 2019 (before the first series of experiments, i.e., Figure 2a) and in 2021 (between the second
 475 and third series of experiments, i.e., Figure 2b and Figure 2c, respectively) showed some elevation
 476 differences compared to the theoretical topography, and between the two topographical surveys, of less
 477 than 2 mm. The effect of this change in topography was tested using Model 1 and $C_D = 0.4$. Results show
 478 a weak influence on the flow velocity pattern and all the other results (Table S1 in the Supplementary
 479 Material), thus, the theoretical topography was used for the rest of the cases.

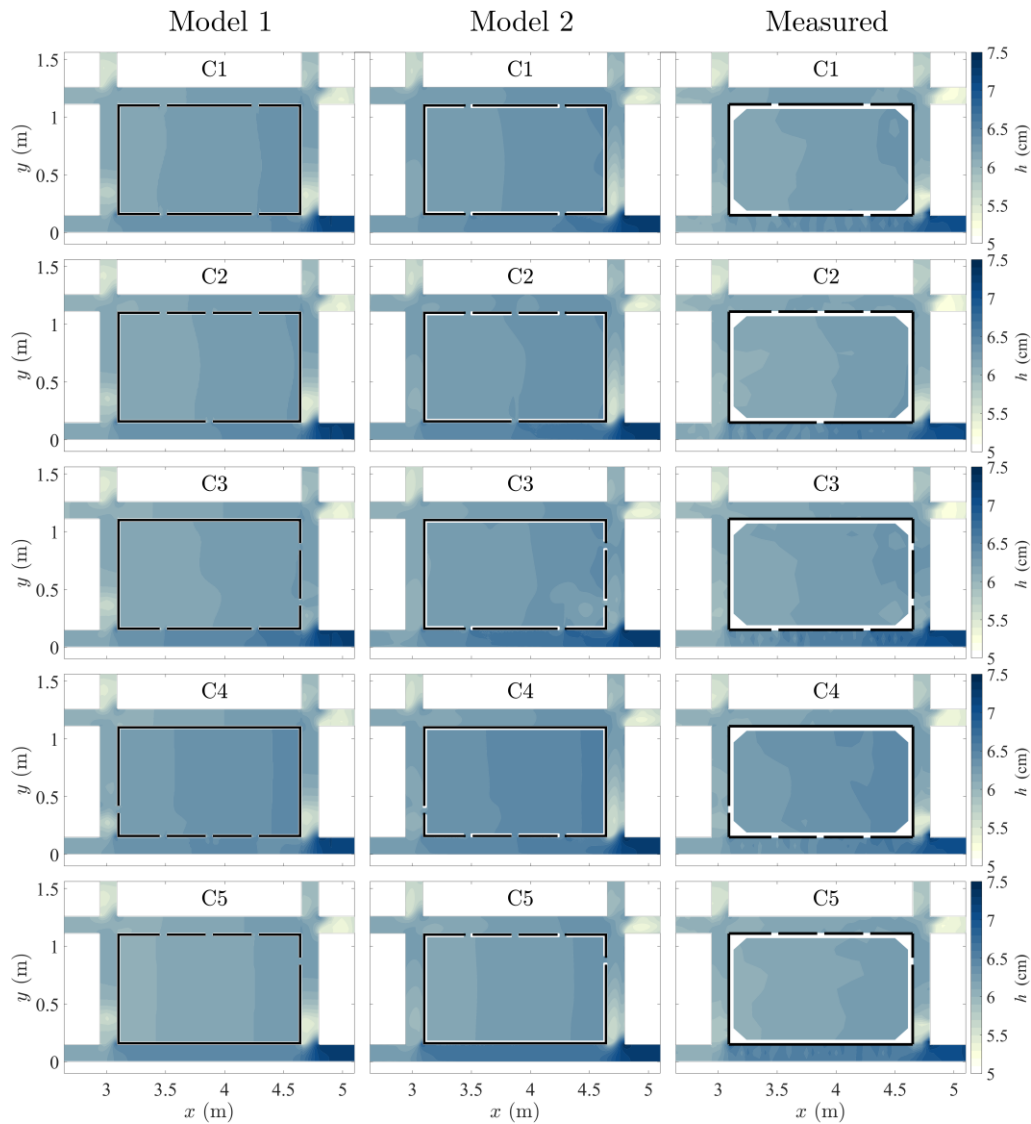
480 *3.2. Steady flow tests*

481 *3.2.1. Flow depths*

482 Figure 4 shows that both models, and hence the 2D SWE, are able to reproduce fairly accurately the
 483 measured flow depth patterns for cases with steady flow (Figure 2a and b). There is a flow depth difference
 484 between the Right and Left Streets because the weir height in Outlet 1 is larger than in Outlet 2. The larger
 485 flow depths in the Right Street compared to the Left Street induce a pressure gradient that enhances the
 486 transverse flow through the porous block openings.

487





489

490 **Figure 4.** Flow depths modelled with Model 1 (left column), Model 2 (middle column) and measured (right column) for steady flow conditions. The first eight configurations are from Mejia-Morales et al. (2021).
 491

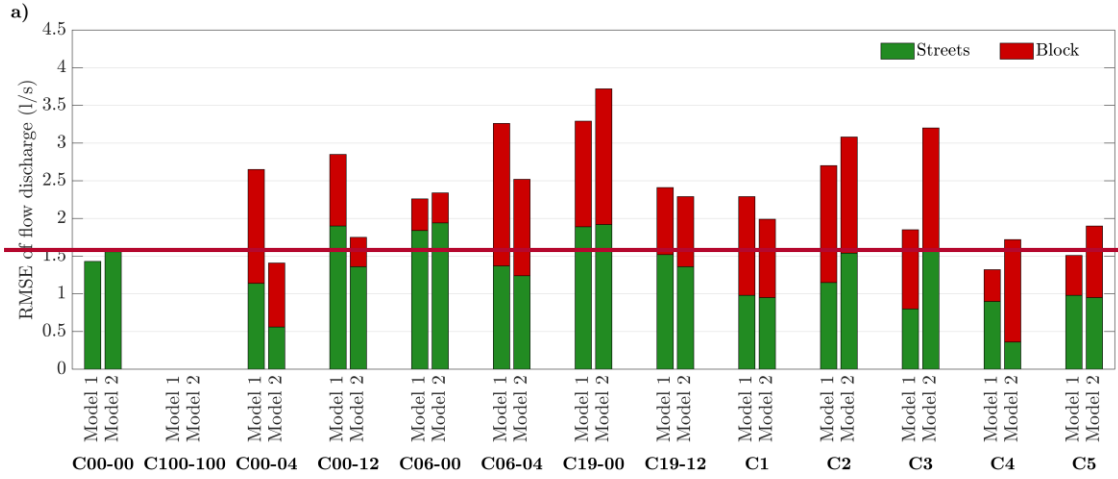
492

493 Both models are capable to reproduce the increasing flow depth at the Right Street, the decreasing flow
 494 depth at the Left Street, and the relatively constant water level within the block, which is a result of the very
 495 low velocities within the block. The differences between the results of the two models are minimal both
 496 within the porous block and in the streets, which implies that at a large scale the turbulence closure model
 497 does not affect the flow depth predictive capabilities of a 2D SWE model in urban floods with steady flow.

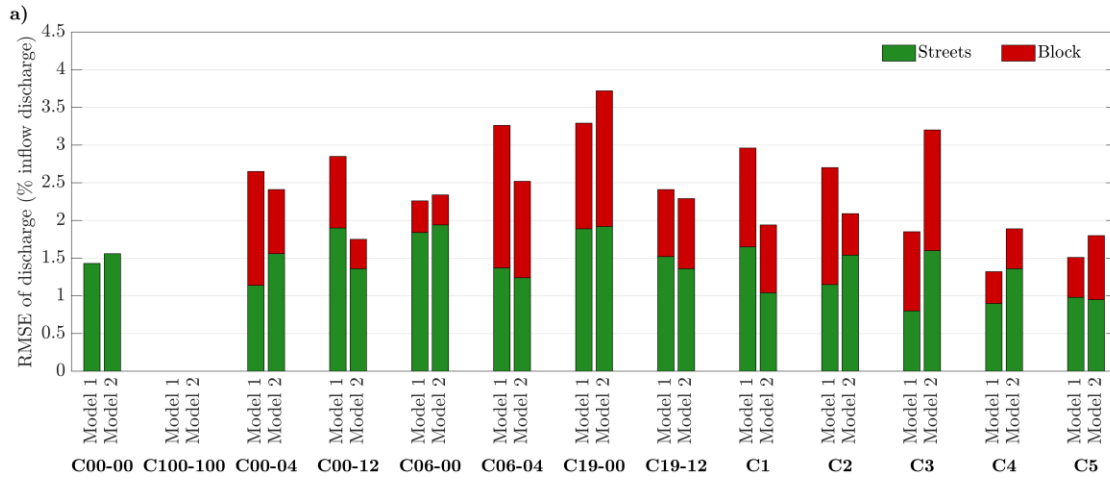
498 3.2.2. Discharge partition

499 The two models reproduce well the discharge partition both in the streets and within the porous block
500 without any of the two exhibiting clearly superior performance (Figure 5a). ~~However,~~ Model 1 predicts
501 more accurately the discharge partitioning at the four outlets with a RMSE that is less than half of that of
502 Model 2 (Figure 5c). Model 2 overestimates Q_{out_4} and both models underestimate Q_{out_1} , except for the case
503 C100-100 (configuration without a block), and ~~slightly underestimate~~approximate well Q_{out_2} (Figure 5b).
504 The two models exhibit a different behavior in Outlet 3, with Model 1 overpredicting and Model 2
505 underpredicting Q_{out_3} (Figure 5b). Overall, Model 1 and Model 2 miscalculate the discharge distribution at
506 the outlets by 2.5% and 7.3% on average, respectively. In the streets surrounding three of the most complex
507 porous blocks (C06-04, C19-12, C3), Model 2 overestimates the discharge in the Right Street, which is the
508 street that conveys most of the discharge, while Model 1 exhibits a more erratic pattern with this discharge
509 (Figure 6). The street that conveys the second largest discharge in these three cases is the Downstream
510 Street, in which both models give good results, besides Model 2 overpredicting the discharge in C19-12.
511 The overpredictions of Model 2 and underpredictions of Model 1 at the large discharges in the Right and
512 Downstream Streets are partially compensated by respective underpredictions and overpredictions of the
513 two models at the street with the smallest discharge, i.e., the Upstream Street (Figure 6). The discharge
514 distribution for all cases is presented in Figure S4 in the Supplementary Material. Overall, the maximum
515 discharge deviation occurs for C100-100 (Figure 5c). Similar disagreements between measurements and
516 2D SWE computations in large open areas were also noted by Li et al. (2021a).

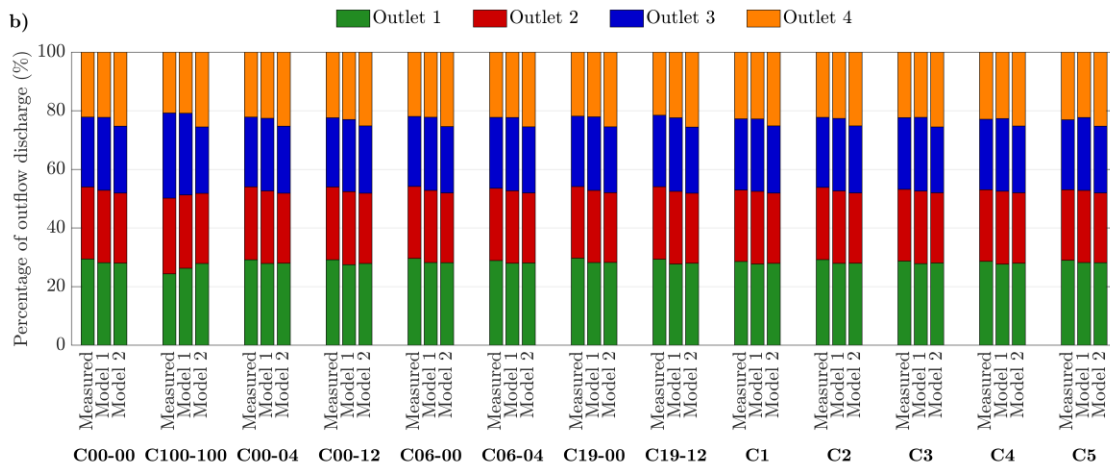
517 Generally, the flow distribution at the outlets corresponds to the experimental ones (error less than
518 ~~±2.5%~~ of the total inflow except the case C100-100) but this distribution is relatively constant due to the
519 general configuration of the street network. Flow discharges in the streets and through the openings of the
520 block are more influenced although the RMSE remains below 2% of the total discharge. However, ~~relatively~~
521 due to the ~~weak parts~~small portion of the flow that enters the block, the relative error can be high ~~(up to~~
522 ~~40%)~~ for the flow passing through the building (Figure S4 in the Supplementary Material).



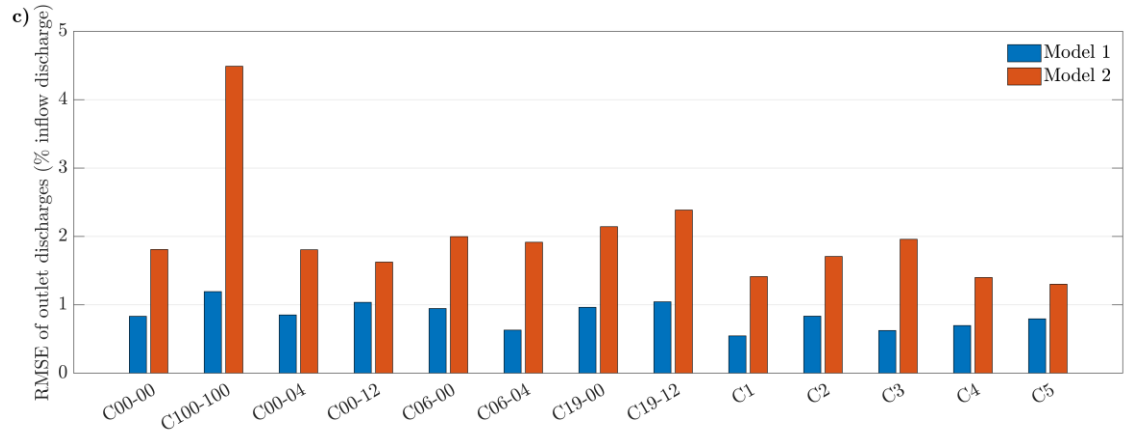
523



524



525

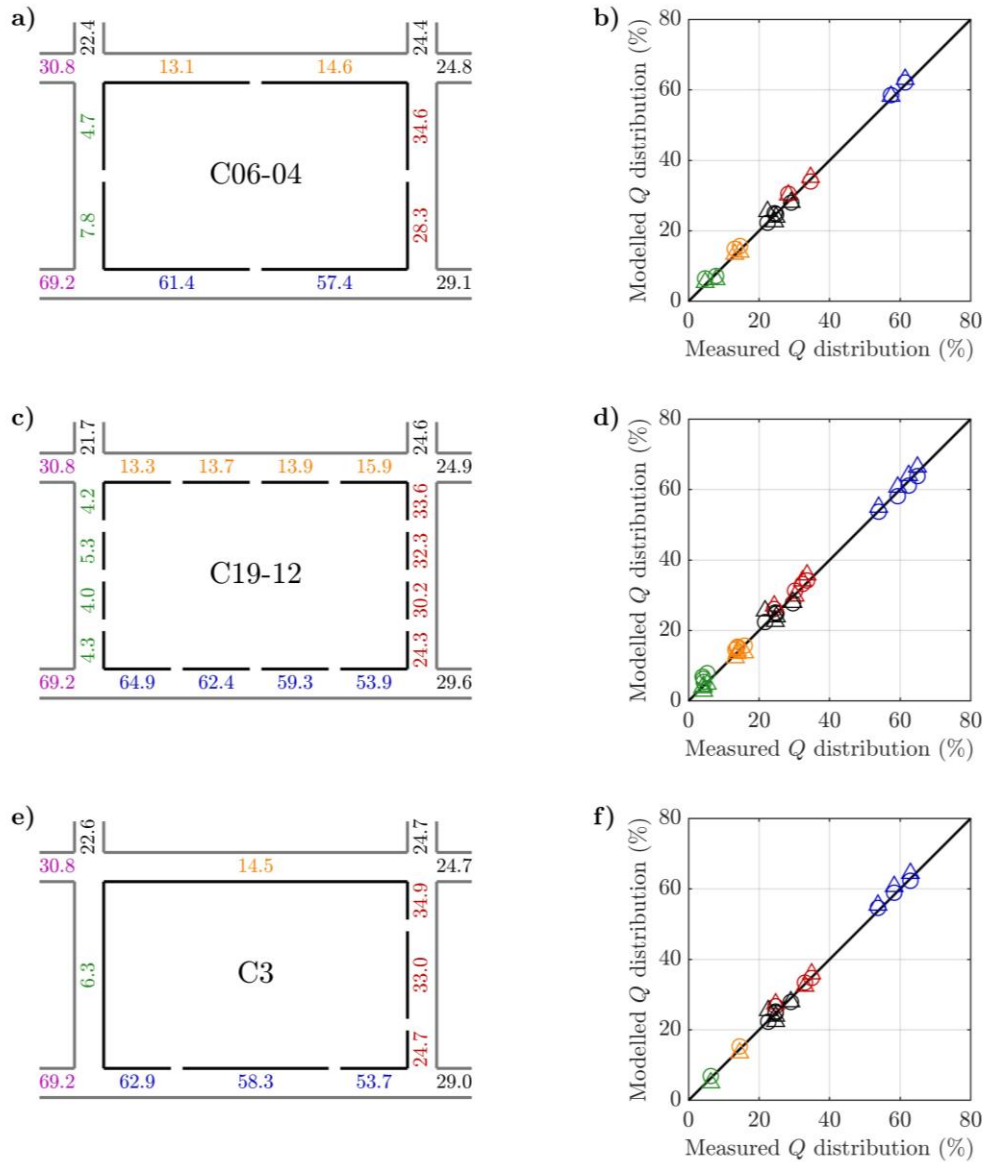


526

527 **Figure 5.** (a) RMSE of flow discharge for Model 1 and Model 2 in the urban block and in the surrounding
 528 streets, (b) Discharge distribution at the four outlets and (c) RMSE between modelled and measured outlet
 529 discharges ~~in percentage points (pp)~~ at the four outlets for the steady flow cases. No data are presented for
 530 C100-100 in (a) because this case does not have a block.

531

532



533

534 **Figure 6.** (a, c, e) Measured discharge distribution around the urban block and at the outlets for selected
 535 cases with steady flow conditions and (b, d, f) comparison between measured and modelled discharges with
 536 Model 1 (circles) and Model 2 (triangles). The colored symbols in each scatter plot of the right column
 537 correspond to the discharges with the same color in the subfigure next to each scatter plot in the left column.

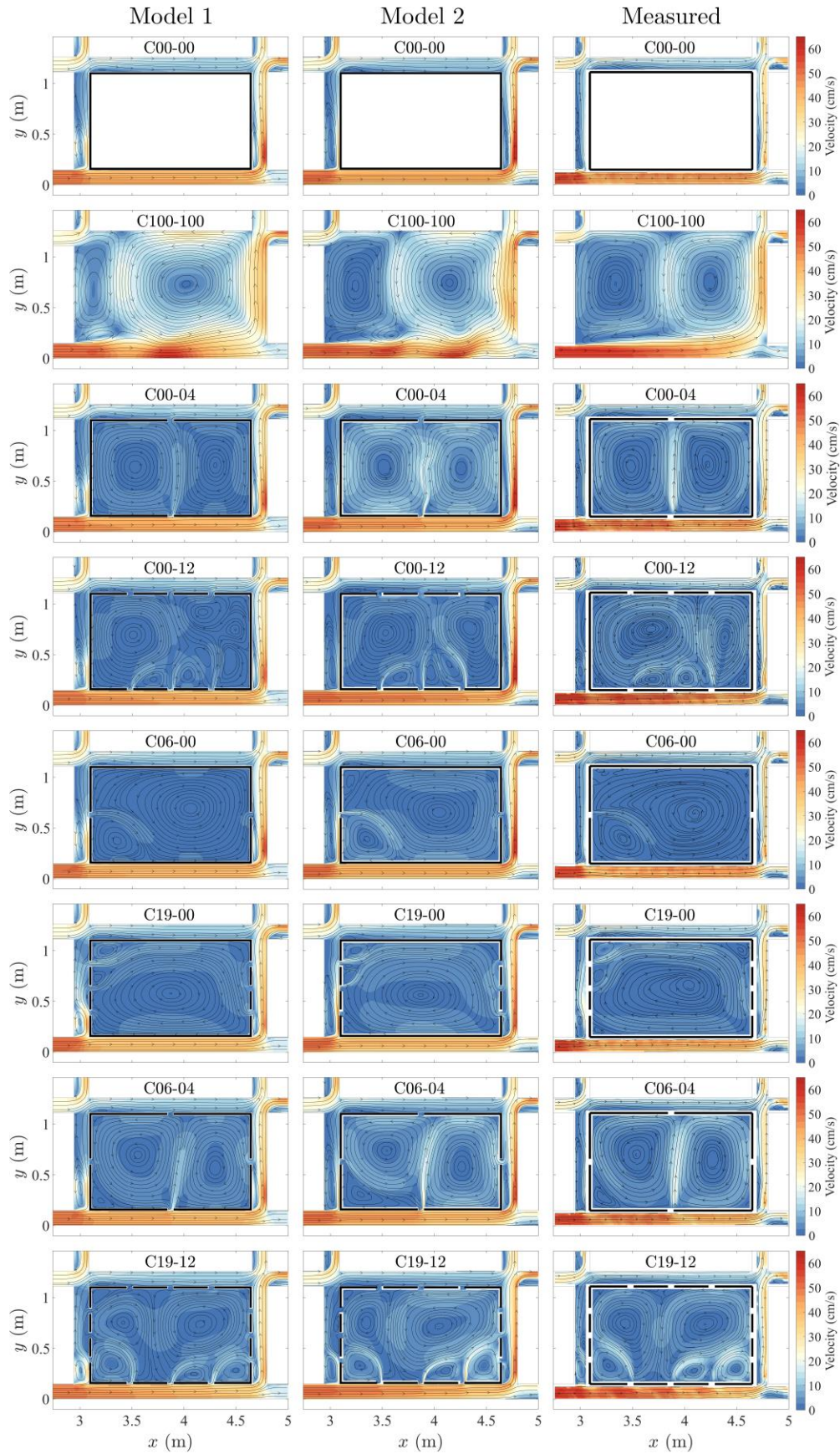
3.2.3. Velocity flow fields

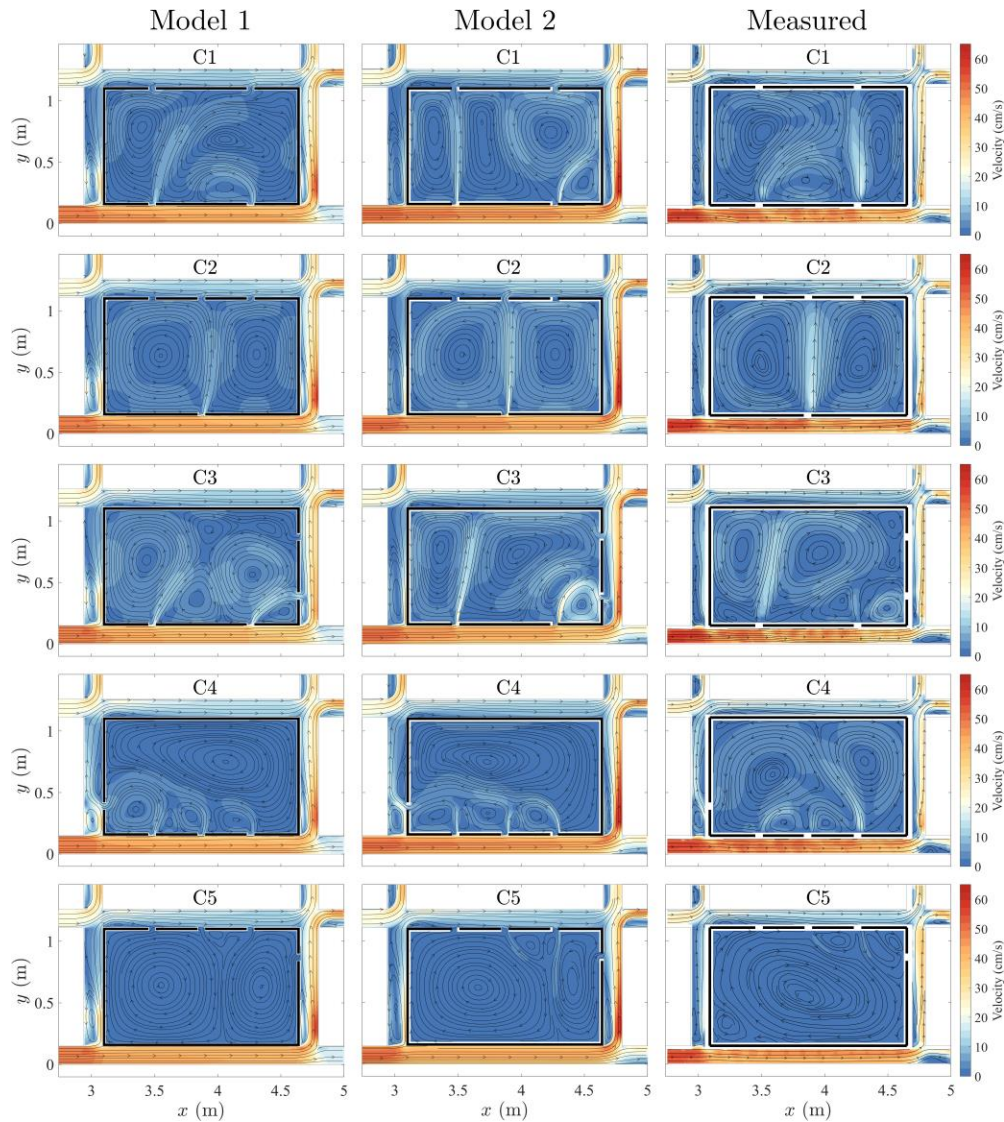
538
539 In this section, the depth-averaged flow velocities modelled with 2D SWE are compared to the surface
540 velocities measured with LSPIV. Mejia-Morales et al. (2021) compared the LSPIV surface velocity
541 measurements to ADV measurements across the flow depth and showed that the surface velocities are
542 mostly well-approximated by depth-averaged velocities. Starting with the two reference cases C00-00 (non-
543 porous block) and C100-100 (no block), the two models reproduce qualitatively all the flow features that
544 were observed in the experiments (Figure 7). In C00-00, the interaction of the flows from the different
545 branches at the junctions matches the measurements well, with a correct distribution of the discharge
546 between the outlets (Figure 5c). In C100-100, even though the modelled discharge distribution at the outlets
547 exhibits the largest deviation from the measurements (Figure 5c), the two models reproduce fairly well,
548 particularly Model 2, the two large recirculation zones. However, they are uneven compared to the
549 measurements, with the downstream and upstream recirculation zones being modelled larger and smaller,
550 respectively, than what was observed.

551 The modelled flow patterns within and around the porous blocks in the first test series (Figure 2a) agree
552 well with the measurements, with the number and direction of the recirculation zones being modelled
553 correctly in almost all cases (Figure 7). For the cases with no more than one opening per side, i.e., C00-04,
554 C06-00, and C06-04, only Model 2 in C06-04 exhibits a notable difference in the size of the recirculation
555 zone in the lower left corner. When there are three openings at two opposite sides of the porous block, the
556 flow pattern becomes much more complex. The two models are still able to simulate the direction of the
557 streamlines quite correctly but the sizes of some of the recirculation zones are a little different than the
558 measured ones. For C00-12, Model 1 adds two small recirculation zones at the right part of the block and
559 Model 2 adds-augments one in the center.

560 The second test series of steady flow cases (presented in Figure 2b) generally exhibits complex flow
561 recirculations (Figure 7) because of the several openings on one side of the block, in each case, and ~~an~~ the
562 asymmetric distribution of the other openings at ~~the~~ an other sides of the porous block. The case C1 is the

563 only exception in the sense that it has two symmetric openings at the sides at the Right Street and Left
564 Street. However, the flow pattern within the block for C1 is quite complex with three main uneven
565 recirculation zones that the two models cannot reproduce in their correct location; moreover, the two models
566 do not obtain the same pattern. In case C2, from the three openings at the Left Street, the middle one
567 influences the flow pattern the most and the flow pattern in the porous block resembles C00-04. The two
568 models reproduce this pattern accurately. Cases C3 to C5 are the more complex ones and the two models
569 are not always able to reproduce entirely the observed flow patterns. The left part of the pattern in C3 is
570 generally well reproduced by Model 1 but the right part with an interaction of three openings is not similar
571 to the measurements. On the other hand, Model 2 predicts quite accurately the flow pattern in C3. Case C4
572 is the most challenging one: the two models provide similar patterns but fail to accurately predict the shape
573 and size of the recirculation zones. As a result, the two observed large counter-rotating recirculation zones
574 are modelled as one and the two smaller ones next to the Right Street have the opposite directionality. The
575 structure of the smaller recirculation zones from the models seems more influenced by the opening at the
576 Upstream Street, compared to the measurements. On the contrary, in a mirrored configuration, the modelled
577 flow patterns in C5 (relatively similar for the two models) seem less influenced by the opening in the
578 Downstream Street compared to the measurements, and as a result the recirculation zone at the right side
579 of the block is modelled larger than what it actually is.





581

582 **Figure 7.** Time-averaged surface velocities modelled with Model 1 (left column), Model 2 (middle column)
 583 and measured (right column) for steady flow conditions. The first eight configurations are from Mejia-
 584 Morales et al. (2021). The modelled flow velocity patterns (left and middle columns) are based on depth-
 585 averaged velocities while the measured flow velocities are surface flow velocities.

586

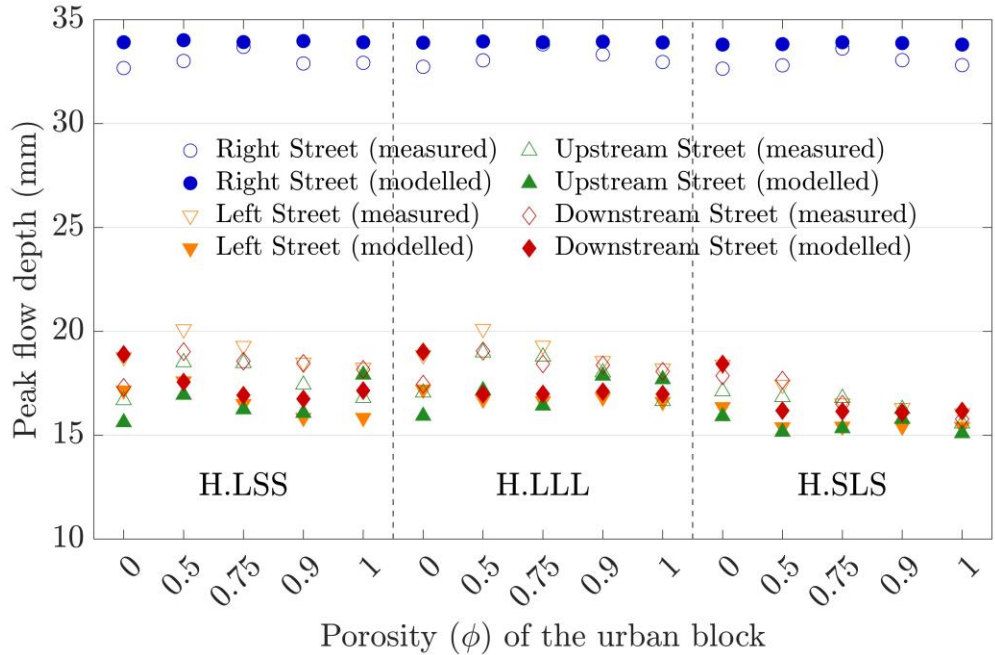
587 3.3. Unsteady flow tests

588 3.3.1. Flow depths

589 The unsteady flow simulations were carried out only with Model 1. The presence of hydraulic jumps
 590 at different locations in the experiments and in the calculations, causes a lower agreement of peak flow
 591 depths compared to the steady flow cases, with an average deviation of 6.7% between calculations and

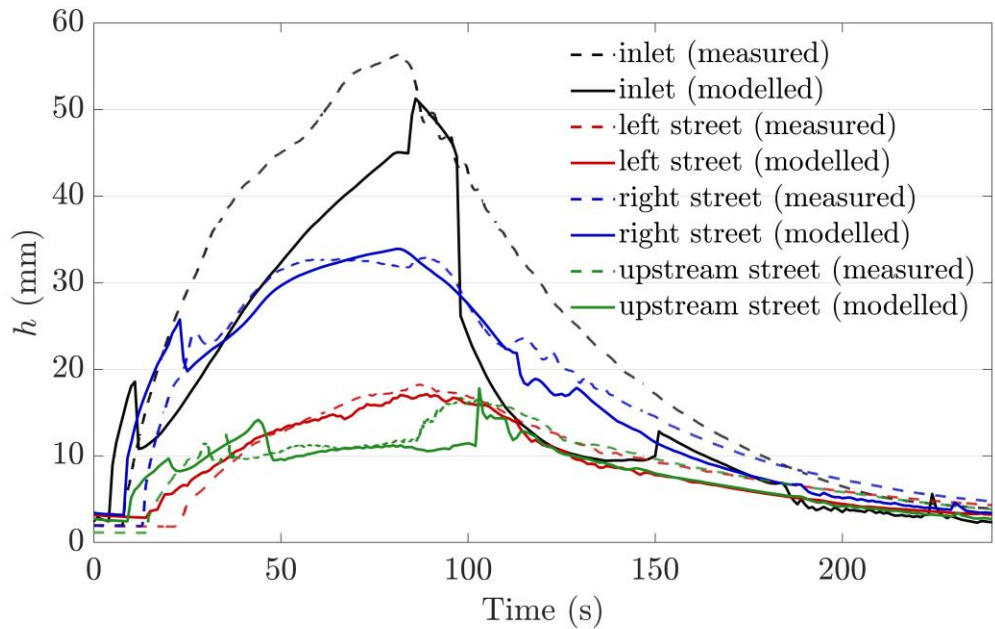
592 measurements in the streets around the block. Model 1 slightly overestimates the peak flow depth in the
593 Right Street, which is the highest peak flow depth in the test domain, with an error of less than ~~10~~4% (Figure
594 8). The model performs best in the Right Street for $\phi = 0.75$, for every tested hydrograph (H.LSS, H.LLL,
595 and H.SLS). No trend is detected between the rest of the block porosities and the performance of the model
596 in predicting peak flow depths in the Right Street. The absolute error in the other three streets around the
597 block is similar to that in the Right Street; however, the peak flow depth is lower and thus, percentagewise
598 Model 1 is less accurate in predicting flow depths there. In these three streets, Model 1 predicts flow depths
599 best in H.SLS (the hydrograph with the greatest unsteadiness), followed by H.LLL and H.LSS. The
600 predictive performance of the model in the H.SLS hydrograph deteriorates with decreasing block porosity,
601 whereas for H.LLL and H.LSS there is a more erratic pattern on the agreement between depth modelling
602 results and measurements. For all flow cases, the flow depth is underestimated in the Left Street (Figure 8)
603 and in the block (Figure S5 in the Supplementary Material).

604 Figure 9 shows how the flow depth evolves in time at different measuring locations (Figure 1b) of the
605 test domain for the hydrograph H.LSS and $\phi = 1$, i.e., the block without any interior obstruction. The model
606 captures the evolution of the flow depths in the Right, Left, and Upstream Street relatively accurately after
607 the first 60 seconds, particularly in the rising limb of the hydrograph; however, it cannot correctly reproduce
608 the flow depth at the location P_{in} .



609

610 **Figure 8.** Measurements and calculations with Model 1 of peak flow depths in the streets around the porous
 611 block (locations P_{RS} , P_{LS} , P_{US} , and P_{DS} in Figure 1b for the Right, Left, Upstream, and Downstream Street,
 612 respectively) for the three cases with unsteady hydrographs (H.LSS, H.LLL, and H.SLS). The tested urban
 613 blocks and their respective porosities are shown in Figure 2c. The vertical dashed lines separate the data
 614 for each flow case.



615

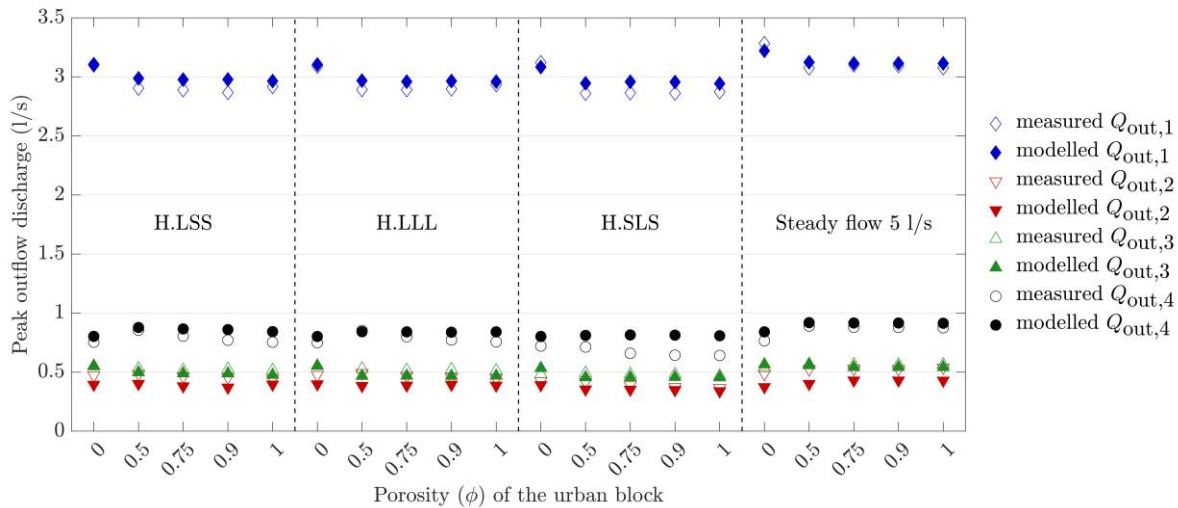
616 **Figure 9.** Measured and calculated (with Model 1) flow depths (locations P_{in} , P_{RS} , P_{LS} , and P_{US} in Figure
 617 1b for the inlet and the Right, Left, and Upstream Street, respectively) as a function of time for the H.LSS
 618 discharge hydrograph with porosity $\phi = 1$ (series 3).

619 *3.3.2. Discharge partition*

620 For steady flow in the configurations of test series 3 (Figure 2c), the discharge at Outlet 4 is
621 ~~overestimated~~ miscalculated by approximately 0.05 l/s on average, while the discharge at Outlet 2 is
622 underestimated by about 0.1 l/s (Figure 10). As for test series 1 and 2 (Figure 2a, b), the downstream
623 boundary conditions should be adapted to obtain a more correct distribution. However, it should be noted
624 that changing critical flow to free outflow at Outlets 1 and 2 (in which the flow is partly supercritical) did
625 not change the outflow distribution. The ~~peak~~ discharges at the outlets for the steady flow case of test
626 series 3 exhibit a slightly increasing trend with increasing porosity in Outlets 2 and 4 and rather constant
627 values, besides $\phi = 0$, in the other outlets (Figure 10). ~~No consistent trends are observed in Outlets 1 and~~
628 ~~3.~~

629 For the unsteady flows, the peak outflow discharge in Outlet 1 is consistently higher than the peak
630 discharges in the other outlets for every tested hydrograph and porosity value, as for the respective steady
631 flow test (Figure 10). The outflow in Outlet 1 becomes the highest when the block has no porosity ($\phi = 10$),
632 while it reaches a plateau for each flow case when the block has porosity. For the unsteady cases, Model 1
633 predicts accurately the peak discharge in Outlet 1 for the non-porous block, for every hydrograph, but it
634 overestimates this peak discharge by less than 54% for ~~most the~~ porous blocks. Model 1 performs even
635 better in predicting the peak discharge in Outlet 1 in the steady flow case, with a slight underestimation of
636 the non-porous block case and a few overestimations for the porous block cases. The second highest peak
637 outflow discharge occurs in Outlet 4, where Model 1 overestimates the peak discharge by around 0.085 l/s
638 for the non-porous block, for all flow cases (Figure 10). The predictive performance of Model 1 mostly
639 deteriorates with increasing porosity of the block for all three hydrographs, particularly for H.SLS, while
640 this is not observed in the steady flow cases, where only a slight overestimation is noted. The
641 overestimations in Outlets 1 and 4 are mostly partially compensated by some underestimations in the peak
642 outflow discharge in Outlet 2, where, percentagewise, the model predictions deviate from the measurements
643 the most for all flow cases, besides the hydrograph H.SLS. Finally, Model 1 predicts accurately the peak

644 outflow discharge in Outlet 3. Overall, for all unsteady cases the average discrepancy between calculations
 645 and measurements of the peak discharges at the outlets is 8.6%. A comparison between the measured and
 646 modelled peak flow depths at the locations $P_{out1} - P_{out4}$ near the outlets (Figure 1b) is provided in Figure S6
 647 in the Supplementary Material.



648

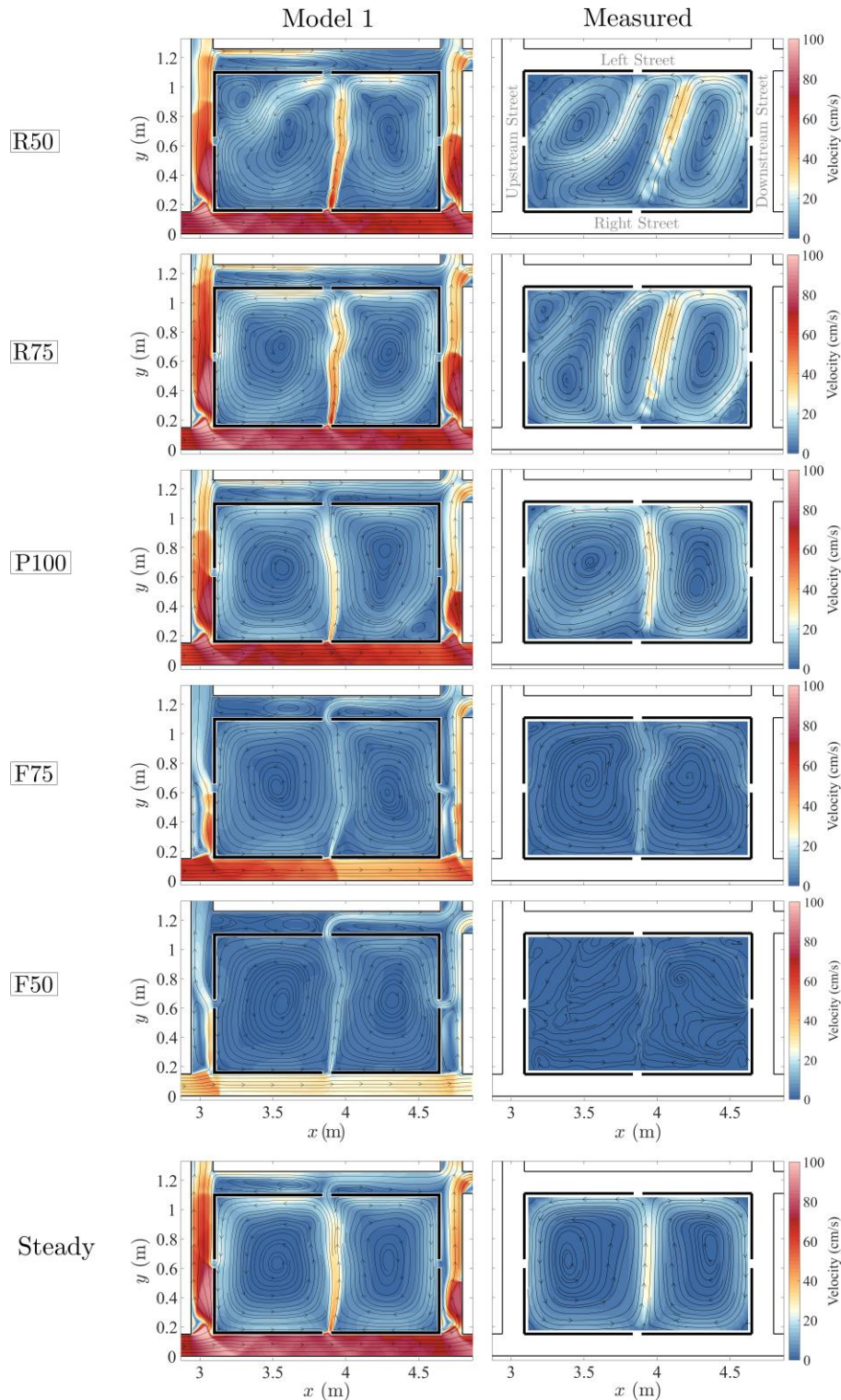
649 **Figure 10.** Measured and calculated (with Model 1) peak discharges at the four outlets of the experimental
 650 setup of Figure 1b for the three cases with unsteady hydrographs (H.LSS, H.LLL, and H.SLS) and a steady
 651 flow case with inflow discharge of 5 l/s, which is equal to the peak value of each unsteady hydrograph at
 652 the inlet. The tested urban blocks and their respective porosities are shown in Figure 2c. The vertical dashed
 653 lines separate the data for each flow case.

654

655 *3.3.3. Velocity flow fields*

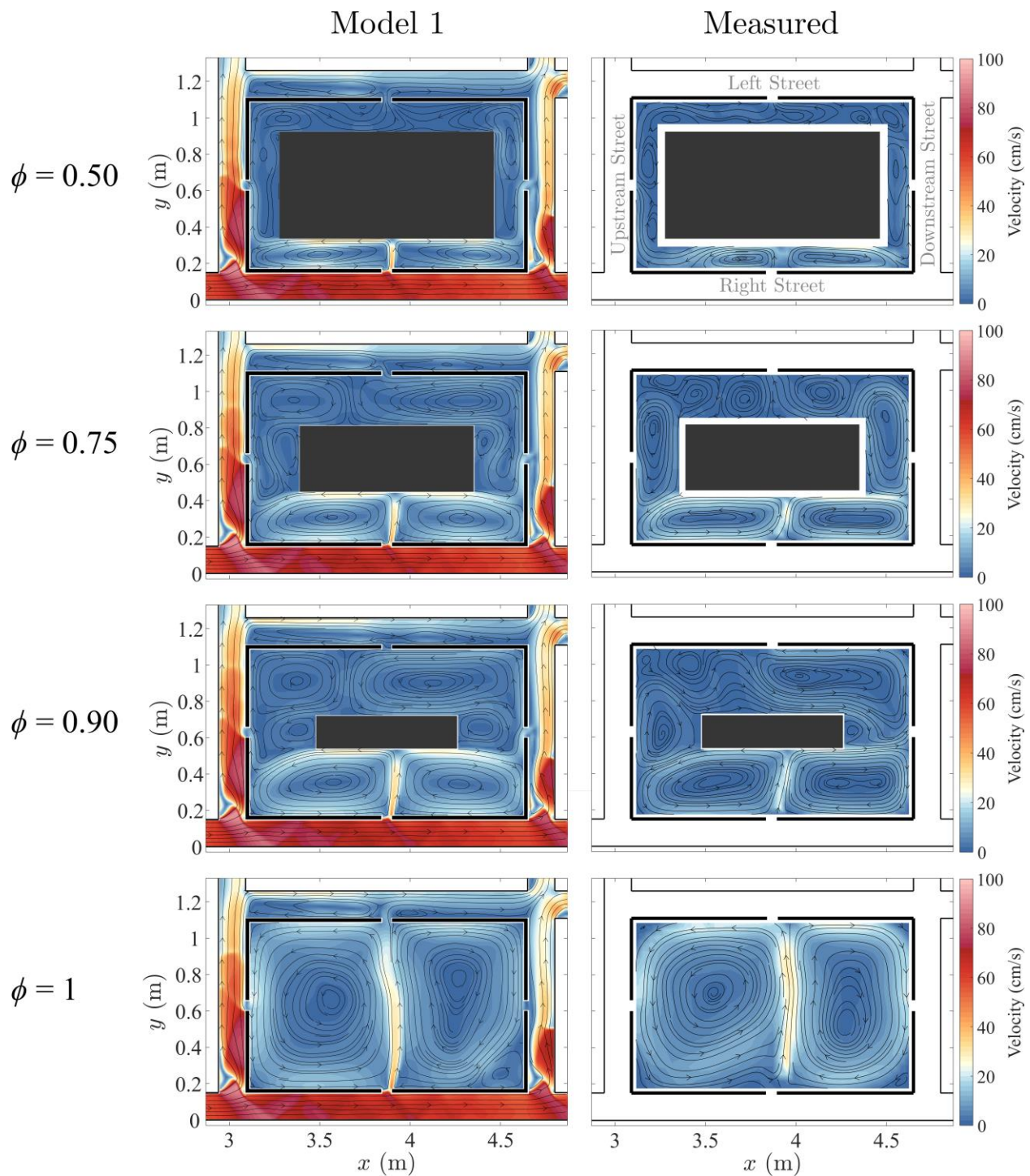
656 As in Section 3.2.3, the depth-averaged flow velocities modelled with 2D SWE are compared to the
 657 surface velocities measured with LSPIV. For $\phi = 1$ in steady flow, the flow pattern of the third series is
 658 quite similar to C06-04 with two main nearly symmetrical recirculation zones (Figure 11). For the unsteady
 659 case with the hydrograph H.LSS (with the greatest unsteadiness), after the flow peak the flow pattern
 660 remains quite similar for a long time. The initial part of this process is reproduced well by Model 1. Before
 661 the flow peak, the block is filling and the observed flow pattern comprises four main recirculation zones
 662 that are not reproduced by Model 1, which, instead, generates a flow pattern that tends more rapidly to a
 663 flow pattern with two main recirculation zones. Reducing ϕ leads to reduced water volume in the block

664 and an increase in the number of recirculation zones within the porous block, which are fairly well
665 reproduced by Model 1 (Figure 12).



666

667 **Figure 11.** Quasi-instantaneous surface velocities modelled with Model 1 (left column) and measured (right
 668 column) for the hydrograph H.LSS and $\phi = 1$. All experimental configurations are presented in were
 669 obtained from Mejia-Morales et al. (2022a). In the first column, R, P, and F stand for rising, peak, and
 670 falling stage of the hydrograph, while the numbers 50, 75, and 100 show the ratio of the flow depth to the
 671 maximum flow depth within the porous block at that instant.



673

674 **Figure 12.** Quasi-instantaneous depth-averaged velocities modelled with Model 1 (left column) and surface
 675 velocities measured (right column) at the peak of the hydrograph H.LSS with various values of ϕ . All
 676 experimental configurations are presented in were obtained from Mejia-Morales et al. (2022a).

677

678 4. Conclusions

679 Accurate and fast computational tools for the estimation of urban flood hazard are of vital importance.
680 Although in such cases the flow can be 3D in parts of the urban layout, it is important from a management
681 perspective to understand when these 3D processes are dominant and when the flow can be reliably
682 modelled with 2D shallow water equations. In this paper, we demonstrated the capacity of two 2D shallow
683 water flow solvers to simulate urban floods involving flow exchanges with the interior of an urban block
684 in nineteen idealized urban layouts. The computations were compared against published and new
685 experimental observations in steady and unsteady conditions. The tested computational models differed
686 mostly by the turbulence closure used for estimating the eddy viscosity.

687 Both models reproduced accurately the measured flow depth for all cases. The prediction of the
688 discharge distribution and the flow velocity patterns within and around the urban block was in general
689 satisfactory but deteriorated when the flow exchanges between the urban block and the surrounding streets
690 increased and became asymmetrical. The average difference between the modelled discharge distributions
691 and the measurements at the outlets was 2.5% and 7.3% for Model 1 and Model 2, respectively. With
692 respect to the flow velocities, none of the two models outperformed consistently the other, which implies
693 that both tested turbulence closure models are suitable to model the flow patterns within and around an
694 urban block, although with different accuracy at different flow patterns.

695 For unsteady conditions, the difficulties increased because of the occurrence of hydraulic jumps and
696 the sequence of a filling phase and an emptying phase of the block. The error thus rose in parameters such
697 as the peak flow depths in the streets and the peak discharges at the outlets, which were miscalculated by
698 6.7% and 8.6%, respectively. However, the influence of the porosity of the urban block was generally
699 simulated in the right way and except during rapid filling of the block, the computed velocity pattern inside
700 the block reproduced sufficiently well the main process.

701 Even if the discharge partition at the outlets is only a little sensitive to a change in the urban block
702 openings, local modifications of the flow field can be particularly important for urban planning under
703 climate change scenarios, since the building density and the distance between neighboring buildings are the
704 most influential parameters affecting pluvial flooding (Bruwier et al., 2020).

705 The geometric configurations considered here are highly simplified compared to real-world urbanized
706 floodplains, which have considerably more intricate flowpaths, street profiles, opening shapes and indoor
707 arrangement of buildings. In addition, in reality the flow exchanges between the streets and the urban blocks
708 are influenced by obstructions near the openings such as parked cars and street furniture (Mignot et al.,
709 2020) and the interaction of surface flows with surcharging sewers (Kitsikoudis et al., 2021). These aspects
710 highlight the limitations of the present study and need to be investigated in future studies with either large
711 scale experiments or field data to additionally address potential scale effects that affected our results. In
712 practice, evaluating accurately the flow intrusion into buildings and building blocks would require
713 particularly fine mesh resolution in the near field of the opening, or the use of parametrizations such as weir
714 equations. Such aspects affect the operationality of models for simulating large urban floodplains and need
715 to be investigated. The performance of 1D modelling in the streets, combined with side discharge equations
716 for the exchanges through building opening, could also be investigated in a follow-up study.

717 **Acknowledgements**

718 The authors from INRAE and INSA Lyon acknowledge the financial support offered by the French National Research
719 Agency (ANR) for the project DEUFI (under grant ANR-18-CE01-0020). The authors gratefully acknowledge MSc
720 students Yann Nicol and Elliott Crestey who contributed to the numerical computations.

721 **Data availability**

722 All experimental observations used in this research are available at: <https://doi.org/10.57745/UJOCJ8> (Mejia-Morales
723 et al., 2022b).

724 **Authors' contributions**

725 The study was designed by A.P., B.D., S.P., and E.M., who also defined the methodology; all laboratory experiments
726 were conducted by M.M.M., under the supervision of S.P. and E.M.; computations with Model 1 were conducted by

727 A.P. and those with Model 2 by students under the guidance of P.A., B.D., S.E., and M.P. The original draft of the
728 manuscript was prepared by V.K. with the support of B.D., A.P., and M.M.M. It was revised by V.K., B.D., E.M. and
729 S.P.

730 References

- 731 Addison-Atkinson, W., Chen, A. S., Memon, F. A., Chang, T.-J. (2022). Modelling urban sewer flooding
732 and quantitative microbial risk assessment: A critical review. *Journal of Flood Risk Management*
733 **15**(4), e12844. <https://doi.org/10.1111/jfr3.12844>
- 734 Almeida, G. A. M. de, Bates, P., Ozdemir, H. (2018). Modelling urban floods at submetre resolution:
735 challenges or opportunities for flood risk management? *Journal of Flood Risk Management* **11**,
736 S855–S865. <https://doi.org/10.1111/jfr3.12276>
- 737 Arrault, A., Finaud-Guyot, P., Archambeau, P., Bruwier, M., Erpicum, S., Pirotton, M., Dewals, B.
738 (2016). Hydrodynamics of long-duration urban floods: experiments and numerical modelling.
739 *Natural Hazards and Earth System Sciences* **16**(6), 1413–1429. [https://doi.org/10.5194/nhess-16-](https://doi.org/10.5194/nhess-16-1413-2016)
740 [1413-2016](https://doi.org/10.5194/nhess-16-1413-2016)
- 741 Arrighi, C., Oumeraci, H., Castelli, F. (2017). Hydrodynamics of pedestrianstextquotesingle instability in
742 floodwaters. *Hydrology and Earth System Sciences* **21**(1), 515–531. [https://doi.org/10.5194/hess-](https://doi.org/10.5194/hess-21-515-2017)
743 [21-515-2017](https://doi.org/10.5194/hess-21-515-2017)
- 744 Bates, P. D. (2022). Flood Inundation Prediction. *Annual Review of Fluid Mechanics* **54**(1), 287–315.
745 <https://doi.org/10.1146/annurev-fluid-030121-113138>
- 746 Bazin, P.-H., Mignot, E., Paquier, A. (2017). Computing flooding of crossroads with obstacles using a 2D
747 numerical model. *Journal of Hydraulic Research* **55**(1), 72–84.
748 <https://doi.org/10.1080/00221686.2016.1217947>
- 749 Bazin, P.-H., Nakagawa, H., Kawaike, K., Paquier, A., Mignot, E. (2014). Modeling Flow Exchanges
750 between a Street and an Underground Drainage Pipe during Urban Floods. *Journal of Hydraulic*
751 *Engineering* **140**(10), 04014051. [https://doi.org/10.1061/\(asce\)hy.1943-7900.0000917](https://doi.org/10.1061/(asce)hy.1943-7900.0000917)
- 752 Bernardini, G., Quagliarini, E., D’Orazio, M., Brocchini, M. (2020). Towards the simulation of flood
753 evacuation in urban scenarios: Experiments to estimate human motion speed in floodwaters.
754 *Safety Science* **123**, 104563. <https://doi.org/10.1016/j.ssci.2019.104563>
- 755 Birkmann, J., Welle, T., Solecki, W., Lwasa, S., Garschagen, M. (2016). Boost resilience of small and
756 mid-sized cities. *Nature* **537**(7622), 605–608. <https://doi.org/10.1038/537605a>
- 757 Brown, R., Chanson, H. (2013). Turbulence and Suspended Sediment Measurements in an Urban
758 Environment during the Brisbane River Flood of January 2011. *Journal of Hydraulic Engineering*
759 **139**(2), 244–253. [https://doi.org/10.1061/\(asce\)hy.1943-7900.0000666](https://doi.org/10.1061/(asce)hy.1943-7900.0000666)
- 760 Bruwier, M., Erpicum, S., Archambeau, P., Pirotton, M., Dewals, B. (2017). Discussion of: Computing
761 flooding of crossroads with obstacles using a 2D numerical model. *Journal of Hydraulic*
762 *Research* **55**(5), 737–741. <https://doi.org/10.1080/00221686.2017.1326406>
- 763 Bruwier, M., Maravat, C., Mustafa, A., Teller, J., Pirotton, M., Erpicum, S., Archambeau, P., Dewals, B.
764 (2020). Influence of urban forms on surface flow in urban pluvial flooding. *Journal of Hydrology*
765 **582**, 124493. <https://doi.org/10.1016/j.jhydrol.2019.124493>
- 766 Camnasio, E., Erpicum, S., Archambeau, P., Pirotton, M., Dewals, B. (2014). Prediction of mean and
767 turbulent kinetic energy in rectangular shallow reservoirs. *Engineering Applications of*
768 *Computational Fluid Mechanics* **8**(4), 586–597.
769 <https://doi.org/10.1080/19942060.2014.11083309>
- 770 Chang, T.-J., Wang, C.-H., Chen, A. S., Djordjevic, S. (2018). The effect of inclusion of inlets in dual
771 drainage modelling. *Journal of Hydrology* **559**, 541–555.
772 <https://doi.org/10.1016/j.jhydrol.2018.01.066>

773 Chen, D., Acharya, K., Stone, M. (2010). Sensitivity Analysis of Nonequilibrium Adaptation Parameters
774 for Modeling Mining-Pit Migration. *Journal of Hydraulic Engineering* **136**(10), 806–811.
775 [https://doi.org/10.1061/\(asce\)hy.1943-7900.0000242](https://doi.org/10.1061/(asce)hy.1943-7900.0000242)

776 Chen, S., Huang, Q., Muttarak, R., Fang, J., Liu, T., He, C., Liu, Z., Zhu, L. (2022). Updating global
777 urbanization projections under the Shared Socioeconomic Pathways. *Scientific Data* **9**(137).
778 <https://doi.org/10.1038/s41597-022-01209-5>

779 Chen, W., Wang, X., Deng, S., Liu, C., Xie, H., Zhu, Y. (2019). Integrated urban flood vulnerability
780 assessment using local spatial dependence-based probabilistic approach. *Journal of Hydrology*
781 **575**, 454–469. <https://doi.org/10.1016/j.jhydrol.2019.05.043>

782 Chen, Y., Zhou, H., Zhang, H., Du, G., Zhou, J. (2015). Urban flood risk warning under rapid
783 urbanization. *Environmental Research* **139**, 3–10. <https://doi.org/10.1016/j.envres.2015.02.028>

784 Costabile, P., Costanzo, C., Lorenzo, G. D., Macchione, F. (2020). Is local flood hazard assessment in
785 urban areas significantly influenced by the physical complexity of the hydrodynamic inundation
786 model? *Journal of Hydrology* **580**, 124231. <https://doi.org/10.1016/j.jhydrol.2019.124231>

787 Dewals, B., Bruwier, M., Piroton, M., Erpicum, S., Archambeau, P. (2021). Porosity Models for Large-
788 Scale Urban Flood Modelling: A Review. *Water* **13**(7), 960. <https://doi.org/10.3390/w13070960>

789 Dewals, B., Erpicum, S., Archambeau, P., Piroton, M. (2012). Discussion of: Experimental study of
790 velocity fields in rectangular shallow reservoirs. *Journal of Hydraulic Research* **50**(4), 435–436.
791 <https://doi.org/10.1080/00221686.2012.702856>

792 Doocy, S., Daniels, A., Murray, S., Kirsch, T. D. (2013). The Human Impact of Floods: a Historical
793 Review of Events 1980-2009 and Systematic Literature Review. *PLoS Currents*.
794 <https://doi.org/10.1371/currents.dis.f4deb457904936b07c09daa98ee8171a>

795 Dottori, F., Figueiredo, R., Martina, M. L. V., Molinari, D., Scorzini, A. R. (2016). INSYDE: a synthetic,
796 probabilistic flood damage model based on explicit cost analysis. *Natural Hazards and Earth
797 System Sciences* **16**(12), 2577–2591. <https://doi.org/10.5194/nhess-16-2577-2016>

798 El Kadi Abderrezzak, K., Lewicki, L., Paquier, A., Rivière, N., Travin, G. (2011). Division of critical
799 flow at three-branch open-channel intersection. *Journal of Hydraulic Research* **49**(2), 231–238.
800 <https://doi.org/10.1080/00221686.2011.558174>

801 El Kadi Abderrezzak, K., Paquier, A. (2009). Discussion of “Numerical and Experimental Study of
802 Dividing Open-Channel Flows” by A. S. Ramamurthy, Junying Qu, and Diep Vo. *Journal of
803 Hydraulic Engineering* **135**(12), 1111–1112. [https://doi.org/10.1061/\(asce\)hy.1943-
804 7900.0000009](https://doi.org/10.1061/(asce)hy.1943-7900.0000009)

805 Erpicum, S., Dewals, B. J., Archambeau, P., Piroton, M. (2010). Dam break flow computation based on
806 an efficient flux vector splitting. *Journal of Computational and Applied Mathematics* **234**(7),
807 2143–2151. <https://doi.org/10.1016/j.cam.2009.08.110>

808 Erpicum, S., Meile, T., Dewals, B. J., Piroton, M., Schleiss, A. J. (2009). 2D numerical flow modeling in
809 a macro-rough channel. *International Journal for Numerical Methods in Fluids* **61**(11), 1227–
810 1246. <https://doi.org/10.1002/flid.2002>

811 Fujita, I., Muste, M., Kruger, A. (1998). Large-scale particle image velocimetry for flow analysis in
812 hydraulic engineering applications. *Journal of Hydraulic Research* **36**(3), 397–414.
813 <https://doi.org/10.1080/00221689809498626>

814 Gems, B., Mazzorana, B., Hofer, T., Sturm, M., Gabl, R., Aufleger, M. (2016). 3-D hydrodynamic
815 modelling of flood impacts on a building and indoor flooding processes. *Natural Hazards and
816 Earth System Sciences* **16**(6), 1351–1368. <https://doi.org/10.5194/nhess-16-1351-2016>

817 Gross, M. (2016). The urbanisation of our species. *Current Biology* **26**(23), R1205–R1208.
818 <https://doi.org/10.1016/j.cub.2016.11.039>

819 Guo, K., Guan, M., Yu, D. (2021). Urban surface water flood modelling – a comprehensive review of
820 current models and future challenges. *Hydrology and Earth System Sciences* **25**(5), 2843–2860.
821 <https://doi.org/10.5194/hess-25-2843-2021>

822 Haltas, I., Tayfur, G., Elci, S. (2016). Two-dimensional numerical modeling of flood wave propagation in
823 an urban area due to Ürkmez dam-break, Izmir, Turkey. *Natural Hazards* **81**(3), 2103–2119.
824 <https://doi.org/10.1007/s11069-016-2175-6>

825 Heller, V. (2011). Scale effects in physical hydraulic engineering models. *Journal of Hydraulic Research*
826 **49**(3), 293–306. <https://doi.org/10.1080/00221686.2011.578914>

827 Hettiarachchi, S., Wasko, C., Sharma, A. (2018). Increase in flood risk resulting from climate change in a
828 developed urban watershed – the role of storm temporal patterns. *Hydrology and Earth System*
829 *Sciences* **22**(3), 2041–2056. <https://doi.org/10.5194/hess-22-2041-2018>

830 Huang, J., Weber, L. J., Lai, Y. G. (2002). Three-Dimensional Numerical Study of Flows in Open-
831 Channel Junctions. *Journal of Hydraulic Engineering* **128**(3), 268–280.
832 [https://doi.org/10.1061/\(asce\)0733-9429\(2002\)128:3\(268\)](https://doi.org/10.1061/(asce)0733-9429(2002)128:3(268))

833 Huggel, C., Stone, D., Auffhammer, M., Hansen, G. (2013). Loss and damage attribution. *Nature Climate*
834 *Change* **3**(8), 694–696. <https://doi.org/10.1038/nclimate1961>

835 Idel’cik, I. E. (1969). Mémento des pertes de charge. Eyrolles (translated to French by Meury M).

836 Jongman, B. (2018). Effective adaptation to rising flood risk. *Nature Communications* **9**, 1986.
837 <https://doi.org/10.1038/s41467-018-04396-1>

838 Khan, A. A., Cadavid, R., Wang, S. S.-Y. (2000). Simulation of channel confluence and bifurcation using
839 the CCHE2D model. *Proceedings of the Institution of Civil Engineers - Water and Maritime*
840 *Engineering* **142**(2), 97–102. <https://doi.org/10.1680/wame.2000.142.2.97>

841 Kitsikoudis, V., Becker, B. P. J., Huismans, Y., Archambeau, P., Erpicum, S., Piroton, M., Dewals, B.
842 (2020). Discrepancies in Flood Modelling Approaches in Transboundary River Systems: Legacy
843 of the Past or Well-grounded Choices? *Water Resources Management* **34**(11), 3465–3478.
844 <https://doi.org/10.1007/s11269-020-02621-5>

845 Kitsikoudis, V., Erpicum, S., Rubinato, M., Shucksmith, J. D., Archambeau, P., Piroton, M., Dewals, B.
846 (2021). Exchange between drainage systems and surface flows during urban flooding: Quasi-
847 steady and dynamic modelling in unsteady flow conditions. *Journal of Hydrology* **602**, 126628.
848 <https://doi.org/10.1016/j.jhydrol.2021.126628>

849 Kreibich, H., Bergh, J. C. J. M. van den, Bouwer, L. M., Bubeck, P., Ciavola, P., Green, C., Hallegatte,
850 S., Logar, I., Meyer, V., Schwarze, R., Thielen, A. H. (2014). Costing natural hazards. *Nature*
851 *Climate Change* **4**(5), 303–306. <https://doi.org/10.1038/nclimate2182>

852 Kreibich, H., Piroth, K., Seifert, I., Maiwald, H., Kunert, U., Schwarz, J., Merz, B., Thielen, A. H.
853 (2009). Is flow velocity a significant parameter in flood damage modelling? *Natural Hazards and*
854 *Earth System Sciences* **9**(5), 1679–1692. <https://doi.org/10.5194/nhess-9-1679-2009>

855 Leandro, J., Schumann, A., Pfister, A. (2016). A step towards considering the spatial heterogeneity of
856 urban key features in urban hydrology flood modelling. *Journal of Hydrology* **535**, 356–365.
857 <https://doi.org/10.1016/j.jhydrol.2016.01.060>

858 Li, X., Erpicum, S., Mignot, E., Archambeau, P., Piroton, M., Dewals, B. (2021a). Influence of urban
859 forms on long-duration urban flooding: Laboratory experiments and computational analysis.
860 *Journal of Hydrology* **603**, 127034. <https://doi.org/10.1016/j.jhydrol.2021.127034>

861 Li, X., Erpicum, S., Mignot, E., Archambeau, P., Rivière, N., Piroton, M., Dewals, B. (2020). Numerical
862 Insights Into the Effects of Model Geometric Distortion in Laboratory Experiments of Urban
863 Flooding. *Water Resources Research* **56**(7), e2019WR026774.
864 <https://doi.org/10.1029/2019wr026774>

865 Li, X., Kitsikoudis, V., Mignot, E., Archambeau, P., Piroton, M., Dewals, B., Erpicum, S. (2021b).
866 Experimental and Numerical Study of the Effect of Model Geometric Distortion on Laboratory
867 Modeling of Urban Flooding. *Water Resources Research* **57**(10), e2021WR029666.
868 <https://doi.org/10.1029/2021wr029666>

869 Lin, J., He, X., Lu, S., Liu, D., He, P. (2021). Investigating the influence of three-dimensional building
870 configuration on urban pluvial flooding using random forest algorithm. *Environmental Research*
871 **196**, 110438. <https://doi.org/10.1016/j.envres.2020.110438>

872 Liu, L., Sun, J., Lin, B., Lu, L. (2018). Building performance in dam-break flow – an experimental study.
873 *Urban Water Journal* **15**(3), 251–258. <https://doi.org/10.1080/1573062x.2018.1433862>

874 Luo, H., Fytanidis, D. K., Schmidt, A. R., Garcia, M. H. (2018). Comparative 1D and 3D numerical
875 investigation of open-channel junction flows and energy losses. *Advances in Water Resources*
876 **117**, 120–139. <https://doi.org/10.1016/j.advwatres.2018.05.012>

877 Luo, P., Luo, M., Li, F., Qi, X., Huo, A., Wang, Z., He, B., Takara, K., Nover, D., Wang, Y. (2022).
878 Urban flood numerical simulation: Research, methods and future perspectives. *Environmental*
879 *Modelling and Software* **156**, 105478. <https://doi.org/10.1016/j.envsoft.2022.105478>

880 Lv, H., Wu, Z., Meng, Y., Guan, X., Wang, H., Zhang, X., Ma, B. (2022). Optimal Domain Scale for
881 Stochastic Urban Flood Damage Assessment Considering Triple Spatial Uncertainties. *Water*
882 *Resources Research* **58**(7), e2021WR031552. <https://doi.org/10.1029/2021wr031552>

883 Martinez-Gomariz, E., Forero-Ortiz, E., Russo, B., Locatelli, L., Guerrero-Hidalga, M., Yubero, D.,
884 Castan, S. (2021). A novel expert opinion-based approach to compute estimations of flood
885 damage to property in dense urban environments. Barcelona case study. *Journal of Hydrology*
886 **598**, 126244. <https://doi.org/10.1016/j.jhydrol.2021.126244>

887 Martinez-Gomariz, E., Gómez, M., Russo, B., Djordjevic, S. (2018). Stability criteria for flooded
888 vehicles: a state-of-the-art review. *Journal of Flood Risk Management* **11**, S817–S826.
889 <https://doi.org/10.1111/jfr3.12262>

890 Mejia-Morales, M. A., Mignot, E., Paquier, A., Proust, S. (2022a). Laboratory investigation into the effect
891 of the storage capacity of a city block on unsteady urban flood flows. *Water Resources Research*
892 **(under review)**.

893 Mejia-Morales, M. A., Mignot, E., Paquier, A., Proust, S. (2022b). Data set of a laboratory experiment on
894 the impact of the conveyance porosity of an urban block on the flood risk assessment. Recherche
895 Data Gouv, UNF:6:Md2Yh9DNuCDyRl3U3kNGCw== [fileUNF].
896 <https://doi.org/10.57745/UJOCJ8>

897 Mejia-Morales, M. A., Mignot, E., Paquier, A., Sigaud, D., Proust, S. (2021). Impact of the porosity of an
898 urban block on the flood risk assessment: A laboratory experiment. *Journal of Hydrology* **602**,
899 126715. <https://doi.org/10.1016/j.jhydrol.2021.126715>

900 Mejia-Morales, M. A., Proust, S., Mignot, E., Paquier, A. (2020). Experimental and Numerical Modelling
901 of the Influence of Street-Block Flow Exchanges During Urban Floods, in: *Advances*
902 *Hydroinformatics*. Springer Singapore, 495–505. https://doi.org/10.1007/978-981-15-5436-0_39

903 Mignot, E., Camusson, L., Riviere, N. (2020). Measuring the flow intrusion towards building areas during
904 urban floods: Impact of the obstacles located in the streets and on the facade. *Journal of*
905 *Hydrology* **583**, 124607. <https://doi.org/10.1016/j.jhydrol.2020.124607>

906 Mignot, E., Dewals, B. (2022). Hydraulic modelling of inland urban flooding: Recent advances. *Journal*
907 *of Hydrology* **609**, 127763. <https://doi.org/10.1016/j.jhydrol.2022.127763>

908 Mignot, E., Li, X., Dewals, B. (2019). Experimental modelling of urban flooding: A review. *Journal of*
909 *Hydrology* **568**, 334–342. <https://doi.org/10.1016/j.jhydrol.2018.11.001>

910 Mignot, E., Paquier, A., Haider, S. (2006). Modeling floods in a dense urban area using 2D shallow water
911 equations. *Journal of Hydrology* **327**(1-2), 186–199.
912 <https://doi.org/10.1016/j.jhydrol.2005.11.026>

913 Mignot, E., Paquier, A., Rivière, N. (2008). Experimental and numerical modeling of symmetrical four-
914 branch supercritical cross junction flow. *Journal of Hydraulic Research* **46**(6), 723–738.
915 <https://doi.org/10.1080/00221686.2008.9521918>

916 Mignot, E., Zeng, C., Dominguez, G., Li, C.-W., Rivière, N., Bazin, P.-H. (2013). Impact of topographic
917 obstacles on the discharge distribution in open-channel bifurcations. *Journal of Hydrology* **494**,
918 10–19. <https://doi.org/10.1016/j.jhydrol.2013.04.023>

919 Neal, J. C., Bates, P. D., Fewtrell, T. J., Hunter, N. M., Wilson, M. D., Horritt, M. S. (2009). Distributed
920 whole city water level measurements from the Carlisle 2005 urban flood event and comparison
921 with hydraulic model simulations. *Journal of Hydrology* **368**(1-4), 42–55.
922 <https://doi.org/10.1016/j.jhydrol.2009.01.026>

923 Neary, V. S., Sotiropoulos, F., Odgaard, A. J. (1999). Three-Dimensional Numerical Model of Lateral-
924 Intake Inflows. *Journal of Hydraulic Engineering* **125**(2), 126–140.
925 [https://doi.org/10.1061/\(asce\)0733-9429\(1999\)125:2\(126\)](https://doi.org/10.1061/(asce)0733-9429(1999)125:2(126))

926 Ozdemir, H., Sampson, C. C., Almeida, G. A. M. de, Bates, P. D. (2013). Evaluating scale and roughness
927 effects in urban flood modelling using terrestrial LIDAR data. *Hydrology and Earth System*
928 *Sciences* **17**(10), 4015–4030. <https://doi.org/10.5194/hess-17-4015-2013>

929 Perks, M. T., Russell, A. J., Large, A. R. G. (2016). Technical Note: Advances in flash flood monitoring
930 using unmanned aerial vehicles (UAVs). *Hydrology and Earth System Sciences* **20**(10), 4005–
931 4015. <https://doi.org/10.5194/hess-20-4005-2016>

932 Pfahl, S., O’Gorman, P. A., Fischer, E. M. (2017). Understanding the regional pattern of projected future
933 changes in extreme precipitation. *Nature Climate Change* **7**(6), 423–427.
934 <https://doi.org/10.1038/nclimate3287>

935 Postacchini, M., Bernardini, G., D’Orazio, M., Quagliarini, E. (2021). Human stability during floods:
936 Experimental tests on a physical model simulating human body. *Safety Science* **137**, 105153.
937 <https://doi.org/10.1016/j.ssci.2020.105153>

938 Qi, W., Ma, C., Xu, H., Zhao, K., Chen, Z. (2022). A comprehensive analysis method of spatial
939 prioritization for urban flood management based on source tracking. *Ecological Indicators* **135**,
940 108565. <https://doi.org/10.1016/j.ecolind.2022.108565>

941 Ramamurthy, A. S., Qu, J., Vo, D. (2007). Numerical and Experimental Study of Dividing Open-Channel
942 Flows. *Journal of Hydraulic Engineering* **133**(10), 1135–1144.
943 [https://doi.org/10.1061/\(asce\)0733-9429\(2007\)133:10\(1135\)](https://doi.org/10.1061/(asce)0733-9429(2007)133:10(1135))

944 Re, M., Kazimierski, L. D., Garcia, P. E., Ortiz, N. E., Lagos, M. (2022). Assessment of crowdsourced
945 social media data and numerical modelling as complementary tools for urban flood mitigation.
946 *Hydrological Sciences Journal* **67**(9), 1295–1308.
947 <https://doi.org/10.1080/02626667.2022.2075266>

948 Rodi, W. (2017). Turbulence Modeling and Simulation in Hydraulics: A Historical Review. *Journal of*
949 *Hydraulic Engineering* **143**(5), 03117001. [https://doi.org/10.1061/\(asce\)hy.1943-7900.0001288](https://doi.org/10.1061/(asce)hy.1943-7900.0001288)

950 Roger, S., Dewals, B. J., Erpicum, S., Schwanenberg, D., Schüttrumpf, H., Köngeter, J., Piroton, M.
951 (2009). Experimental and numerical investigations of dike-break induced flows. *Journal of*
952 *Hydraulic Research* **47**(3), 349–359. <https://doi.org/10.1080/00221686.2009.9522006>

953 Rosenzweig, B. R., Cantis, P. H., Kim, Y., Cohn, A., Grove, K., Brock, J., Yesuf, J., Mistry, P., Welty,
954 C., McPhearson, T., Sauer, J., Chang, H. (2021). The Value of Urban Flood Modeling. *Earth’s*
955 *Future* **9**(1), e2020EF001739. <https://doi.org/10.1029/2020ef001739>

956 Rubinato, M., Helms, L., Vanderlinden, M., Hart, J., Martins, R. (2022). Flow exchange, energy losses
957 and pollutant transport in a surcharging manhole linked to street profiles. *Journal of Hydrology*
958 **604**, 127201. <https://doi.org/10.1016/j.jhydrol.2021.127201>

959 Sanderson, B. M., Wobus, C., Mills, D., Zarakas, C., Crimmins, A., Sarofim, M. C., Weaver, C. (2019).
960 Informing Future Risks of Record-Level Rainfall in the United States. *Geophysical Research*
961 *Letters* **46**(7), 3963–3972. <https://doi.org/10.1029/2019gl082362>

962 Schindfessel, L., Creëlle, S., Mulder, T. D. (2015). Flow Patterns in an Open Channel Confluence with
963 Increasingly Dominant Tributary Inflow. *Water* **7**(9), 4724–4751.
964 <https://doi.org/10.3390/w7094724>

965 Shettar, A. S., Murthy, K. K. (1996). A numerical study of division of flow in open channels. *Journal of*
966 *Hydraulic Research* **34**(5), 651–675. <https://doi.org/10.1080/00221689609498464>

967 Smith, G. P., Modra, B. D., Felder, S. (2019). Full-scale testing of stability curves for vehicles in flood
968 waters. *Journal of Flood Risk Management* **12**(S2). <https://doi.org/10.1111/jfr3.12527>

969 Sturm, M., Gems, B., Keller, F., Mazzorana, B., Fuchs, S., Papatoma-Köhle, M., Aufleger, M. (2018).
970 Experimental analyses of impact forces on buildings exposed to fluvial hazards. *Journal of*
971 *Hydrology* **565**, 1–13. <https://doi.org/10.1016/j.jhydrol.2018.07.070>

972 Van Emelen, S., Soares-Frazão, S., Riahi-Nezhad, C. K., Chaudhry, M. H., Imran, J., Zech, Y. (2012).
973 Simulations of the New Orleans 17th Street Canal breach flood. *Journal of Hydraulic Research*
974 **50(1)**, 70–81. <https://doi.org/10.1080/00221686.2011.642578>
975 Wu, W. (2008). *Computational River Dynamics*. Taylor and Francis.
976 Wüthrich, D., Pfister, M., Schleiss, A. J. (2020). Forces on buildings with openings and orientation in a
977 steady post-tsunami free-surface flow. *Coastal Engineering* **161**, 103753.
978 <https://doi.org/10.1016/j.coastaleng.2020.103753>
979 Xia, J., Falconer, R. A., Wang, Y., Xiao, X. (2014). New criterion for the stability of a human body in
980 floodwaters. *Journal of Hydraulic Research* **52(1)**, 93–104.
981 <https://doi.org/10.1080/00221686.2013.875073>
982 Xia, J., Teo, F. Y., Lin, B., Falconer, R. A. (2011). Formula of incipient velocity for flooded vehicles.
983 *Natural Hazards* **58(1)**, 1–14. <https://doi.org/10.1007/s11069-010-9639-x>
984 Yalcin, E. (2020). Assessing the impact of topography and land cover data resolutions on two-
985 dimensional HEC-RAS hydrodynamic model simulations for urban flood hazard analysis.
986 *Natural Hazards* **101(3)**, 995–1017. <https://doi.org/10.1007/s11069-020-03906-z>
987 Yen, B. C. (2002). Open Channel Flow Resistance. *Journal of Hydraulic Engineering* **128(1)**, 20–39.
988 [https://doi.org/10.1061/\(asce\)0733-9429\(2002\)128:1\(20\)](https://doi.org/10.1061/(asce)0733-9429(2002)128:1(20))
989 Zhou, Q., Leng, G., Huang, M. (2018). Impacts of future climate change on urban flood volumes in
990 Hohhot in northern China: benefits of climate change mitigation and adaptations. *Hydrology and*
991 *Earth System Sciences* **22(1)**, 305–316. <https://doi.org/10.5194/hess-22-305-2018>
992 Zhou, Q., Yu, W., Chen, A. S., Jiang, C., Fu, G. (2016). Experimental Assessment of Building Blockage
993 Effects in a Simplified Urban District. *Procedia Engineering* **154**, 844–852.
994 <https://doi.org/10.1016/j.proeng.2016.07.448>
995
996

1 Can the 2D shallow water equations model flow intrusion into buildings during urban floods?

2 Benjamin Dewals¹, Vasileios Kitsikoudis², Miguel Angel Mejía-Morales³, Pierre Archambeau¹,

3 Emmanuel Mignot⁴, Sébastien Proust³, Sébastien Erpicum¹, Michel Piroton¹, André Paquier³

4 ¹Hydraulics in Environmental and Civil Engineering, Urban and Environmental Engineering, University
5 of Liege, 4000 Liege, Belgium

6 ²Water Engineering and Management, Faculty of Engineering Technology, University of Twente, 7500
7 AE Enschede, The Netherlands

8 ³UR RiverLy – INRAE, 5 rue de la Doua CS 20244, 69625 Villeurbanne, France

9 ⁴University of Lyon, INSA Lyon, CNRS, LMFA, Ecole Centrale Lyon, Université Claude Bernard
10 Lyon 1, UMR5509, F-69621 Villeurbanne, France

11

12 Abstract

13 The multiple flow paths existing in urban environments lead to complex flow fields during urban flooding.
14 Modelling these flow processes with three-dimensional numerical models may be scientifically sound;
15 however, such numerical models are computationally demanding. To ascertain whether urban floods can
16 be modelled with faster tools, this study investigated for the first time the capacity of the 2D shallow water
17 equations (SWE) in modelling the flow patterns within and around urban blocks with openings, i.e.,
18 involving flow exchanges between the flows in the streets and within the urban blocks (e.g., through alleys
19 leading to courtyards or through broken windows or doors). Laboratory experiments of idealized urban
20 floods were simulated with two academic 2D SWE models, with their most notable difference being the
21 parameterization of the eddy viscosity. Specifically, the first model had a zero-order turbulence closure
22 while the second model had a second-order depth-averaged $k-\varepsilon$ turbulence closure. Thirteen urban layouts
23 were considered with steady flow and five with unsteady flow. Both models simulated the flow depths
24 accurately for the steady cases. The discharge distribution in the streets and the flow velocities were
25 predicted with lower accuracy, particularly in layouts with large open spaces. The average deviation of the
26 modelled discharge distribution at the outlets was 2.5% and 7.3% for the first and second model,

27 respectively. For the unsteady cases, only the first model was tested. It predicted well the velocity pattern
28 during the falling limb of a flood wave, while it did not reproduce all recirculation zones in the rising limb.
29 The peak flow depths in the streets and the peak discharges at the outlets were predicted with an average
30 deviation of 6.7% and 8.6%, respectively. Even though some aspects of the flow in an urban setup are 3D,
31 the findings of this study support the modelling of such processes with 2D SWE models.

32 **Keywords**

33 Experimental hydraulics; Numerical modelling; Open channel flow; Shallow water equations;
34 Turbulence; Urban flood

35 **1. Introduction**

36 Urban flood risk is a growing concern (Addison-Atkinson et al., 2022; Chen et al., 2015; Doocy et al.,
37 2013) given the high urbanization rate (Birkmann et al., 2016; Chen et al., 2022; Gross, 2016) and the
38 intense anticipated rainfall events due to climate change (Hettiarachchi et al., 2018; Pfahl et al., 2017;
39 Sanderson et al., 2019). The flood risk mapping of an urban area remains a challenging task due to the
40 variability in the direct and indirect flood impacts (Kreibich et al., 2014) and in the flood vulnerability
41 (Chen et al., 2019; Huggel et al., 2013; Lv et al., 2022) associated with various socioeconomic contexts in
42 different parts of a city, as well as due to intricate urban layouts that induce complex flow patterns
43 influencing the flood hazard (Leandro et al., 2016; Li et al., 2021a; Lin et al., 2021).

44 Urban flood numerical modelling is a vital component of flood risk assessment (Rosenzweig et al.,
45 2021) and management (Guo et al., 2021; Jongman, 2018), and supports design strategies for sustainable
46 and resilient urban infrastructures (Qi et al., 2022; Zhou et al., 2018). Contrary to one-dimensional (1D)
47 (Kitsikoudis et al., 2020) and 1D-2D (Bates, 2022) simplifications that can be made in river modelling
48 aiming mostly at estimating inundation extents, numerical modelling of multidirectional flows in flooded
49 urban areas should be at least 2D (Li et al., 2021a; Mignot et al., 2006), with a focus on the spatial

50 distribution of not only flow depths but also flow velocities (Kreibich et al., 2009) and specific discharges
51 (Costabile et al., 2020) to express the flood hazard degree in the street network. This is particularly true for
52 large impervious surfaces upstream of and in urban areas that can lead to an excessive amount of runoff,
53 which cannot be conveyed by the drainage systems. Such high flow discharges may threaten the stability
54 of pedestrians (Arrighi et al., 2017; Bernardini et al., 2020; Postacchini et al., 2021; Xia et al., 2014) and
55 can cause the entrainment of vehicles (Martinez-Gomariz et al., 2018; Smith et al., 2019; Xia et al., 2011).
56 Hence, the accurate spatial quantification of hydraulic variables within an urban area is of utmost
57 importance.

58 *1.1. Role of laboratory experiments for model validation*

59 A large number of numerical modelling studies simulated urban flows in real-world cases (Guo et al.,
60 2021; Luo et al., 2022), with some of them using LiDAR data with high-resolution digital elevation models
61 of the urban topography (Almeida et al., 2018; Ozdemir et al., 2013; Yalcin, 2020). However, validation
62 field data including both flow depths and velocities are usually lacking or insufficient (Costabile et al.,
63 2020), which may lead to equifinality issues. Remote sensing techniques can provide inundation extents
64 and water levels, although with certain limitations as tall buildings within the urban environment may
65 obscure some measurements (Neal et al., 2009), but flow velocity measurements in urban floods are more
66 challenging. Such measurements are dangerous and can be costly, and as a result, are limited (Brown and
67 Chanson, 2013). Flow depths and surface velocities can alternatively be determined by monitoring parts of
68 a flooded urban area with unmanned aerial vehicles (Perks et al., 2016) and by analyzing existing footage
69 and crowdsourced data from flooded street networks (Mignot and Dewals, 2022; Re et al., 2022). However,
70 there are uncertainties related to the boundary conditions in complex urban terrains with large spatial
71 variability and to the interplay between surface flow and flow in underground drainage systems (Bazin et
72 al., 2014; Chang et al., 2018; Kitsikoudis et al., 2021; Rubinato et al., 2022). Finally, the typically short
73 duration of pluvial flooding and its local character do not allow for detailed measurements over long
74 durations. Experimental measurements in laboratory facilities provide an alternative option for models'

75 validation. In carefully designed experiments, the flow and boundary conditions can be accurately
76 controlled (Mignot et al., 2019) and besides offering a better understanding of the governing physical
77 processes, such studies can contribute to the validation of numerical models, which may subsequently be
78 used for scenario analyses of field cases.

79 *1.2. Performance of 2D shallow water models*

80 The 2D shallow water equations (SWE) can be used to simulate the flow in flooded streets, with
81 typically large width-to-depth ratios. However, at street intersections the interacting flows coming from
82 various branches generate complex patterns (Mignot et al., 2008) and 3D flow structures (El Kadi
83 Abderrezzak et al., 2011; Ramamurthy et al., 2007). While 3D models can capture most features of
84 diverging flows in bifurcations (Mignot et al., 2013; Neary et al., 1999; Ramamurthy et al., 2007) and
85 converging flows in junctions (Huang et al., 2002; Luo et al., 2018; Schindfessel et al., 2015), it is important
86 to examine whether these flow processes can be satisfactorily reproduced by 2D operational models that
87 are much faster than 3D models and can be used for real-time modelling. The 2D SWE approach has been
88 proven capable to replicate experimental measurements of flow depths and discharge partitioning in
89 bifurcations (Bazin et al., 2017; El Kadi Abderrezzak and Paquier, 2009; Khan et al., 2000; Li et al., 2021b;
90 Shettar and Murthy, 1996), in junctions (Li et al., 2021b), in crossroads (Mignot et al., 2008), as well as in
91 larger and more complicated street networks such as that of Arrault et al. (2016) with 49 intersections and
92 that of Li et al. (2021b) with four intersections. Li et al. (2021a) incorporated various urban layouts in their
93 experimental setup and also modelled successfully the flow depths and discharge partition with a 2D SWE
94 model.

95 Despite the successful applications of 2D SWE in modelling water surface profiles and discharge
96 distributions, some open questions remain (Li et al., 2020) regarding the accuracy of 2D SWE in predicting
97 flow velocities in intersections, the extents of recirculating flow areas occurring due to flow separation in
98 some of the branches, and the role of the turbulence closure model (Rodi, 2017). Shettar and Murthy (1996)

99 modelled depth-averaged flow velocities in a bifurcation with a $k-\varepsilon$ turbulence closure and their modelled
100 velocities in the main channel and the length of the recirculation zone agreed well with the experimental
101 measurements. However, their modelled velocities in the branch of the bifurcation were less accurate. Khan
102 et al. (2000) also modelled the flow in a bifurcation but with a mixing length model and reported that the
103 modelled depth-averaged velocities compared well with the measurements, while the dimensions of the
104 recirculation zone were predicted by the model satisfactorily. Bazin et al. (2017) used a constant eddy
105 viscosity model to simulate flows in a bifurcation with a branch with a 90 degree angle, with and without
106 obstacles at the intersection, and the modelled depth-averaged flow velocities in the recirculation zone on
107 the upstream side of the bifurcation branch deviated from the measurements. Bruwier et al. (2017) argued
108 that a $k-\varepsilon$ turbulence closure model should be more suitable than a constant eddy viscosity model for
109 modelling flow interactions in intersections, given that since a $k-\varepsilon$ model does not necessarily require
110 calibration, its computational demand can be similar to a constant eddy viscosity model that requires
111 calibration. Arrault et al. (2016) showed in a more complex setup that the turbulence closure model was not
112 particularly influential in the estimation of discharge distribution in the various streets; however, a $k-\varepsilon$
113 turbulence closure model modified significantly the estimates of the recirculation lengths compared to a
114 simulation without a turbulence model. No velocity measurements were available, however, to compare the
115 modelled velocities. More recently, Li et al. (2021a) modelled depth-averaged velocities in an urban district
116 with various urban forms with a $k-\varepsilon$ turbulence closure model and achieved good agreement with surface
117 velocities in areas of flow contraction, however, the results were less accurate in large open areas.
118 Supercritical (Bazin et al., 2017; Mignot et al., 2008) and transcritical (El Kadi Abderrezzak et al., 2011)
119 flows in crossroads may pose additional challenges in 2D SWE models, since the occurrence and structure
120 of hydraulic jumps can significantly affect the discharge partitioning and water surface profiles.

121 *1.3. Flow intrusion into buildings: an extra challenge*

122 Numerical and experimental studies of urban flooding typically consider flow around non-porous
123 residential blocks (Haltas et al., 2016; Van Emelen et al., 2012). However, in reality urban blocks may have

124 corridors leading to backyards, while during intense flooding windows and doors (labeled as "openings"
125 from now on) of buildings may break, leading to lateral flow exchanges between a street and the inside area
126 of the buildings (Mignot et al., 2020) causing significant damages in their interiors (Dottori et al., 2016;
127 Martinez-Gomariz et al., 2021). Mejia-Morales et al. (2021) conducted a systematic experimental analysis
128 of the effect of the location and size of openings in an urban block located within an idealized urban district.
129 They showed that the flow exchanges between the streets and the block interior can alter the flow depth
130 and the flow velocity in the surrounding streets by 12% and 70%, respectively, when compared to a
131 reference case with a non-porous block. Besides the recent study of Mejia-Morales et al. (2021), there is
132 only a limited number of studies that investigated how the porosity of urban blocks affects the hydraulic
133 characteristics of a flood. Mignot et al. (2020) measured the flow discharge entering a building through an
134 open door, window, or gate in case of an urban flood, and they noticed that in some cases the intruding
135 discharge can be approximated by formulas for side weirs. However, the authors also observed that this
136 intruding discharge can be significantly affected by surrounding urban obstacles. Wüthrich et al. (2020)
137 showed with a flume experiment how the hydrostatic force and the form drag exerted by a steady flow on
138 a building are modified by the porosity and the orientation of the building, while Sturm et al. (2018)
139 measured the flood impact forces on physical models of buildings with openings on a torrential fan. In other
140 experiments, Liu et al. (2018) showed how the orientation of a house with respect to the incoming flow
141 affects the forcing on the house door for a dam-break case and Zhou et al. (2016) found differences in the
142 wakes of simplified porous and non-porous buildings. In a numerical study of a torrential flood, Gems et
143 al. (2016) modelled how the different openings of a building affect the flow pattern within its interior, the
144 associated hydrodynamic forcing, and the near-building flow pattern. The findings of these studies show
145 that the openings in buildings affect the spatial distribution of flood hazard and thus the number and types
146 of openings should be considered in flood modelling.

147 *1.4. Objective of the study*

148 The flow exchanges between a street and the interior of a building, in combination with bifurcations
149 and junctions at crossroads, lead to complex and potentially 3D flow patterns around urban blocks during
150 urban floods. Since urban areas are typically densely populated, there is a need for fast computational tools
151 that could be utilized for real-time modelling of not only the flow depths but also the flow velocities for the
152 accurate estimation of the flood hazard. 3D numerical models can potentially capture the flow processes of
153 urban floods; however, they are computationally demanding and slow for real-time modelling. In practice,
154 the 2D SWE are used for operational flood hazard and risk modelling. While previous studies have already
155 analysed the ability of the 2D SWE to simulate flow fields in various settings, such as bifurcations,
156 junctions, 4-branch crossroads, and street networks, they all assumed that the street boundaries (i.e.,
157 building facades) were impervious. No existing study has focused on the performance of the 2D SWE to
158 predict the flow intrusion into flooded buildings or building blocks, nor on the flow patterns in the streets
159 and within the urban blocks in urban configurations with openings in the building facades.

160 The objective of this study is to examine, for the first time, whether the flow patterns within and around
161 porous urban blocks (i.e., with openings) can be quickly and accurately predicted with numerical modelling
162 based on 2D SWE and to determine what is the most effective modelling strategy for the accurate estimation
163 of flow velocities and flow depths. To this end, the experiments of Mejia-Morales et al. (2021) and Mejia-
164 Morales et al. (2022a) for flow around and within a porous urban block are replicated using two different
165 academic numerical modelling tools to investigate the importance of eddy viscosity parameterization on
166 the accuracy of the models. Complementary steady flow experiments with additional geometric
167 configurations are also presented for the first time, based on the same experimental approach as Mejia-
168 Morales et al. (2021). The paper is organized as follows: in Section 2, the experimental procedure is briefly
169 described, and the numerical models are presented. The new experimental results and the results of the
170 numerical modelling are presented and discussed in Section 3. Finally, conclusions are drawn in Section 4.

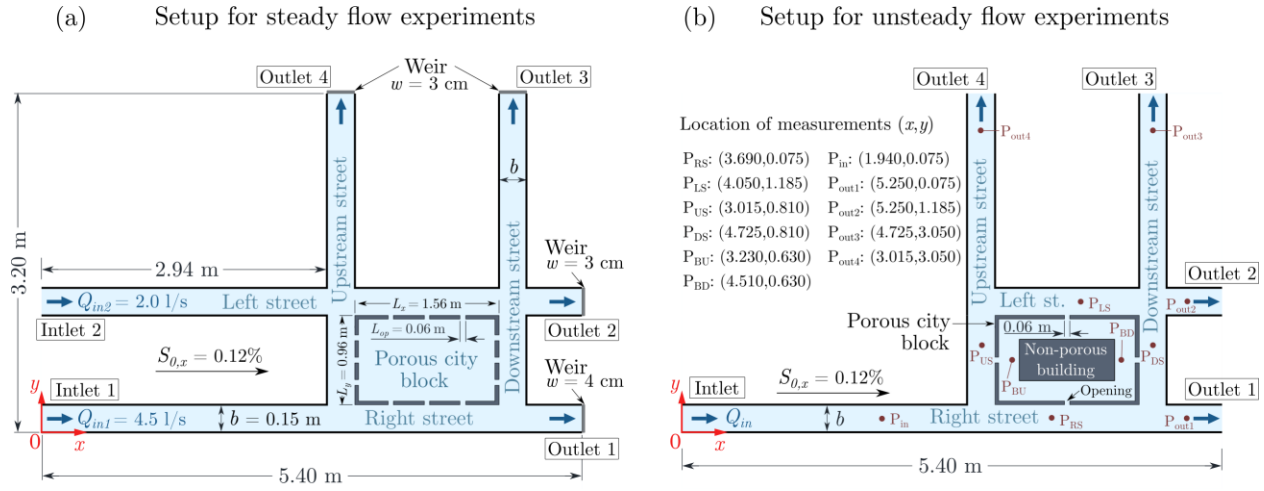
171 2. Experiments and numerical modelling

172 This section presents the experimental setup (Section 2.1), the various porous urban block
173 configurations that were tested (Section 2.2), the numerical models that were used to simulate the
174 experimental data (Section 2.3), and the prescribed boundary and initial conditions (Section 2.4). Both
175 steady and unsteady flow conditions were simulated with the numerical models. For steady flow conditions,
176 the experimental data are a combination of the data presented by Mejia-Morales et al. (2021) and new data
177 collected from the same urban physical model in the same facility. For unsteady flow conditions, the
178 experimental data of Mejia-Morales et al. (2022a) are used. Only a brief overview of the experimental setup
179 and methods is provided here since they are described in detail in the aforementioned papers.

180 2.1. Experimental setup

181 Mejia-Morales et al. (2021) and Mejia-Morales et al. (2022a) experimentally investigated urban floods
182 at the city block scale using a physical model of a rectangular urban block surrounded by four streets, under
183 steady (Figure 1a) and unsteady (Figure 1b) flow conditions. For the steady flow experiments, the length
184 of the two streets in the x -direction (named “Right Street” and “Left Street”) was 5.4 m and the length of
185 the two streets in the y -direction (named “Downstream Street” and “Upstream Street”) was 3.2 m. All four
186 streets had the same rectangular cross section with a width $b = 0.15$ m. The experimental setup for the
187 unsteady flow experiments was the same, except for the initial part of the Left Street, which was closed
188 upstream of the Upstream Street (Figure 1b). The physical model had a slope $S_{0,x} = 0.12\%$ in the x
189 direction and $S_{0,y} = 0\%$ in the y direction, whereas the bed of the model was constructed with PVC and
190 the sidewalls of the streets and the urban block were constructed with plastic. Various configurations of the
191 urban block were tested (Section 2.2 and Figure 2); however, its total lengths in the x and y directions
192 remained fixed at $L_x = 1.56$ m and $L_y = 0.96$ m, respectively. The thickness and the height of the walls of
193 the porous block were 2 cm and 15 cm, respectively.

194 The model inlets were located at the upstream ends of the streets in the x direction. As such, the steady
195 flow experiments had two inlets with fixed inlet discharges Q_{in_1} and Q_{in_2} for the Right Street and Left Street,
196 respectively, while for the unsteady experiments discharge was fed only through the Right Street since the
197 upstream reach of the Left Street was closed. The inlet discharges were measured using separate valve-
198 flowmeter systems with an accuracy of 3%. Smooth inlet conditions were secured by placing a plastic
199 honeycomb grid at the point entrance of the Right Street and of the Left Street. Each one of the four streets
200 of the physical model had an outlet with a vertical tail weir that regulated the flow depth. For the steady
201 flow cases, the weir height of Outlet 1 in the Right Street was 4 cm and of Outlet 2 in the Left Street was
202 3 cm, with respective outlet discharges Q_{out_1} and Q_{out_2} . In the two streets in the y direction, the Outlet 3 in
203 the Downstream Street and the Outlet 4 in the Upstream Street had the same 3 cm weir height, with outlet
204 discharges Q_{out_3} and Q_{out_4} , respectively. For the unsteady flow cases, the weir height was set to zero in all
205 outlets to avoid the reflection of the floodwaves on the weir. The outflow discharges at the four outlets were
206 monitored using electromagnetic flowmeters. Specifically, the water overflowing the weir in each outlet
207 was collected in a separate tank and subsequently the flow exiting each tank was measured with an
208 OPTIFLUX 2000 flowmeter, manufactured by KROHNE.



210

211 **Figure 1.** (a) Experimental setup for the steady flow experiments (adapted from Mejia-Morales et al.
 212 (2021)) and (b) experimental setup for the unsteady flow experiments (adapted from Mejia-Morales et al.
 213 (2022a)). In (b) the locations of measurements denote the points where flow depths were recorded for the
 214 whole duration of the hydrograph.

215 The flow depths in the physical model were measured using ultrasonic distance-measuring sensors
 216 (BAUMER UNDK 20I6914/S35A) with a 0.65 mm uncertainty. For the steady flow cases, a sensor was
 217 attached on a mechanical gantry system that allowed horizontal movement, with measurements being taken
 218 every 5 cm along the longitudinal direction of each street and at three locations across the street width with
 219 6.5 cm spacing. Flow depth measurements within the porous urban block were conducted every 12 cm in
 220 both x and y directions. Each depth measurement was conducted with a sampling frequency of 50 Hz for a
 221 duration of 50 s (Mejia-Morales et al., 2021). For the unsteady flow cases, flow depths were measured at
 222 the eleven locations depicted in Figure 1b for the whole duration of each hydrograph. The reported flow
 223 depths are the results of ensemble averaging of 50 identical floodwaves that were fed sequentially into the
 224 model, with a steady base flow separating two sequential floodwaves. The number of required repeated
 225 floodwaves was selected by increasing the number until the ensemble average standard deviation of the
 226 flow depth became smaller than 1 mm. The floodwaves characteristics are detailed in Section 2.4.

227 For the steady flow cases, surface flow velocities were measured using large-scale particle image
228 velocimetry (LSPIV) (Fujita et al., 1998). Floating wood shavings (1 - 4 mm) were used as tracers. A
229 Panasonic HC-V770 camera was positioned 2.8 m above the physical model, monitoring the plan view at
230 a rate of 25 frames per second with a resolution of 1920 px by 1080 px. The time-averaged surface
231 velocities estimated by the LSPIV technique stabilized after different periods of time for the various areas
232 of the model, but none of them exceeded 60 s (Mejia-Morales et al., 2021). More details about the seeding
233 of the flow, the flow monitoring, the data post-processing, and a validation of the LSPIV measurements
234 against measurements with an acoustic Doppler velocimeter (ADV) are provided in Mejia-Morales et al.
235 (2021).

236 For the unsteady flow cases, it was not feasible to monitor the flow velocities in the whole flow area.
237 Only the surface velocities within the porous block and at two points in the Right Street and Left Street
238 (shown in Figure 1b) were monitored. Moreover, an ensemble average was not used for the LSPIV due to
239 prohibitive post-processing load (Mejia-Morales et al., 2022a). A Sony ZV-1 camera with a sampling rate
240 of 25 frames per second was used and the collected frames were averaged over periods of 2 seconds to filter
241 the data.

242 2.2. *Urban block configurations*

243 In every experiment, the urban block was in the same position near the downstream end in the x
244 direction and had the same dimensions L_x and L_y (Figure 1). However, the conveyance porosity (i.e., the
245 porosity of each sidewall of the urban block), ψ , as defined by the number and locations of openings,
246 differed in each experiment. Each opening had a width $L_{op} = 6$ cm and each sidewall of the block had no
247 more than three openings. In all tests, the water surface elevation remained lower than the height of the
248 openings. In the present paper, three series of configurations for the porous block are examined (Figure 2):

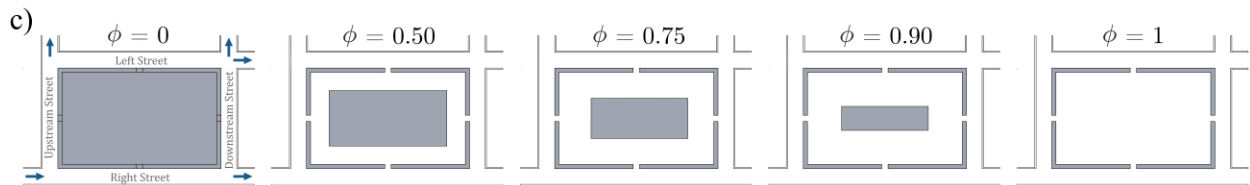
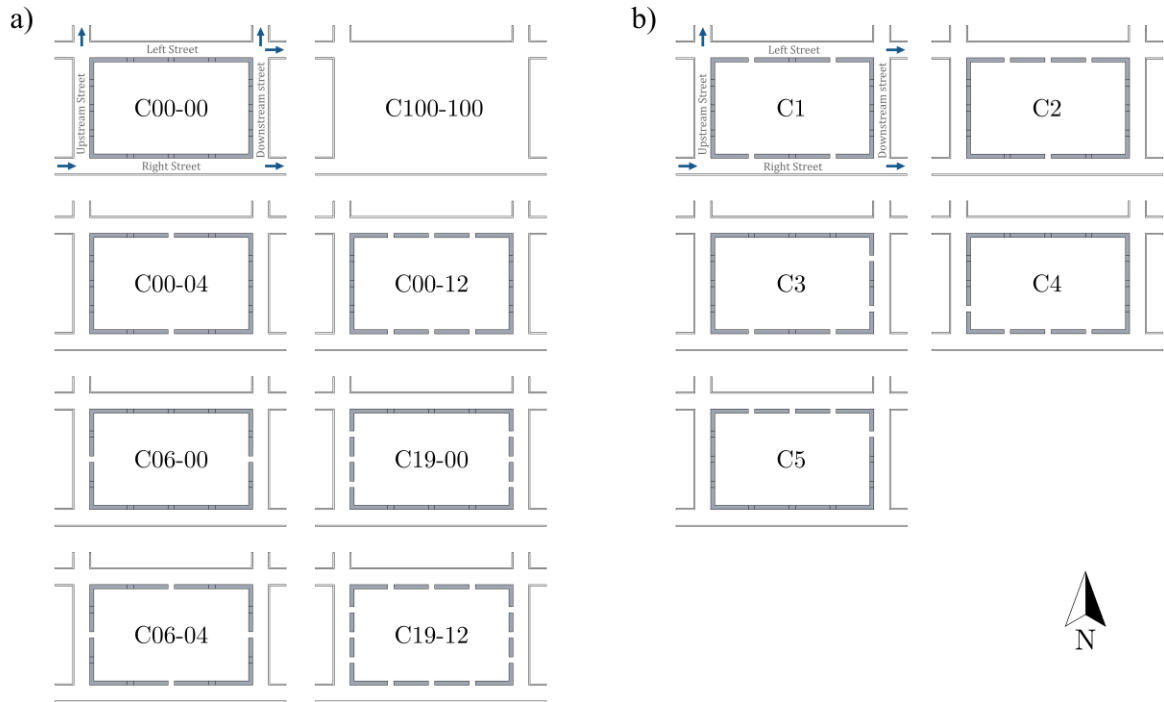
- 249 • The first series comprises the eight configurations presented by Mejia-Morales et al. (2021) without
250 obstruction within the block (Figure 2a). The conveyance porosity of each configuration is

251 presented as C_{xx-yy} , where xx and yy denote the ratio of the total length of the openings in a side
252 of the porous block to the length of that side, in percent, in the x and y directions, respectively. The
253 locations of the openings in the configuration with the largest conveyance porosity (C19-12) are
254 shown in Figure 1a. The conveyance porosity in the rest of the configurations is determined by
255 closing some of the openings of C19-12, while maintaining symmetry in the porous block openings.

- 256 • The second series comprises five new configurations, constructed and tested with the same
257 experimental approach as Mejia-Morales et al. (2021), also without obstructions within the block
258 (Figure 2b). The common trait of these configurations is that each configuration has four openings
259 in its perimeter (the remaining ones after blocking eight openings in C19-12 shown in Figure 1a).
260 Since there is no symmetry in every configuration, these configurations are simply named C1 – C5
261 in order of appearance.
- 262 • The configurations in the third series, presented in Mejia-Morales et al. (2022a), have one opening
263 in the middle of each wall of the block and a non-porous rectangular obstacle in the center of the
264 block. The footprint area of this obstacle was varied as shown in Figure 2c, leading to an areal
265 porosity, ϕ , for each case that is determined as the ratio of the empty area within the block to its
266 total internal area.

267 Note that the concept of porosity is introduced here for the sole purpose of providing a macroscopic
268 description of the considered geometric layouts (Figure 2), while the flow models used in this study are not
269 porosity shallow-water models (e.g., Dewals et al. (2021)). They aim to fully resolve the flow field on the
270 considered computational mesh.

271 The first and second series were used with steady flow conditions, while the third series was used with
272 both steady and unsteady flow conditions. Details about the upstream boundary conditions of each case are
273 presented in Section 2.4.



276 **Figure 2.** (a) Geometric configurations of the porous block of Mejia-Morales et al. (2021) with steady flow
 277 (series 1), (b) new geometric configurations of the porous block with steady flow (series 2), and
 278 (c) geometric configurations of the porous block with steady and unsteady flow (series 3). The arrows in
 279 the first geometric configuration of each subfigure show the flow direction in each street around the porous
 280 block and they are the same for the rest of the geometric configurations in each subfigure. In (a), the
 281 conveyance porosity, ψ , of each sidewall of each configuration is given by C_{xx-yy} , where xx and yy denote
 282 the ψ value in percent in the x and y directions, respectively. In (b), due to lack of symmetry in every case,
 283 the naming of the configurations is simply in order of appearance. In (c), the symbol ϕ denotes the areal
 284 porosity of the porous block as defined by the ratio of the empty space within the block to its total internal
 285 area. The grey rectangles in the center of the blocks in subfigure (c) denote solid non-porous obstacles. The
 286 blocks in (a) and (b) were tested in the experimental setup of Figure 1a and the blocks in (c) were tested in
 287 the experimental setup of Figure 1b.

288 The physical models were designed by assuming a geometrically distorted scale, with horizontal and
 289 vertical scale ratios equal to 50 and 10, respectively. This means that a studied flow in the physical model

290 may be interpreted as a representation of a real-world flow in streets with 7.5 m in width around an urban
 291 block with dimensions 78 m \times 48 m and openings 3 m wide. The upscaled studied flow depths are around
 292 60 cm. This approach ensures relatively large depths in the physical model to enable a satisfactory
 293 measurement accuracy (Heller, 2011; Li et al., 2021b).

294 **2.3. Numerical modelling**

295 The laboratory experiments were simulated using two academic numerical codes that solve the 2D
 296 SWE equations. The two models have differences in their mathematical formulation and their numerical
 297 discretization. The first model is implemented in the software Rubar20 (Mignot et al., 2008) developed by
 298 the Riverly research unit of Inrae in Lyon and the second one is implemented in Wolf 2D (Epicum et al.,
 299 2009) developed by the HECE group at the University of Liege. Table 1 provides an overview of the
 300 characteristics of each model, referred to as Model 1 for Rubar20 and Model 2 for Wolf 2D. The steady
 301 flow cases were simulated with both numerical models, while only Model 1 was used for the simulation of
 302 the unsteady flow cases.

303 **Table 1.** Details of the tested numerical models.

	Model 1	Model 2
Software	Rubar 20	Wolf 2D
Reference	Mignot et al. (2008)	Epicum et al. (2009)
Turbulence closure	Elder’s formula (zero-order model)	Depth-averaged $k-\varepsilon$ model
Friction formula	Explicit Colebrook-White (Yen, 2002) (Eq. (6))	Colebrook-White (Eq. (5))
Numerical scheme	Godunov type	Flux-vector splitting

304

305 **2.3.1. Governing equations**

306 The two codes solve the conservative form of the 2D SWE, which means that the main unknowns are
 307 the flow depth, h , and the specific discharges, hu and hv , with u and v denoting the depth-averaged flow

308 velocities along the x and y direction, respectively. The 2D SWE in conservative form are written as follows
 309 (Wu, 2008):

$$\frac{\partial hu}{\partial t} + \frac{\partial}{\partial x} \left(hu^2 + \frac{gh^2}{2} \right) + \frac{\partial hv}{\partial y} = \frac{\tau_{bx}}{\rho} + \frac{1}{\rho} \frac{\partial h\tau_{xx}}{\partial x} + \frac{1}{\rho} \frac{\partial h\tau_{xy}}{\partial y} \quad (1)$$

$$\frac{\partial hv}{\partial t} + \frac{\partial huv}{\partial x} + \frac{\partial}{\partial y} \left(hv^2 + \frac{gh^2}{2} \right) = \frac{\tau_{by}}{\rho} + \frac{1}{\rho} \frac{\partial h\tau_{xy}}{\partial x} + \frac{1}{\rho} \frac{\partial h\tau_{yy}}{\partial y} \quad (2)$$

310 where g is the acceleration of gravity, ρ is the water density, t is the time, τ_{xx} , τ_{yy} , and τ_{xy} are the depth-
 311 averaged stresses comprising both the Reynolds and molecular stresses (Ercicum et al., 2009), and τ_{bx} and
 312 τ_{by} are the bed shear stresses in the x and y direction, respectively, calculated from Eqs. (3) and (4) in line
 313 with Camnasio et al. (2014):

$$\frac{\tau_{bx}}{\rho} = f \frac{u\sqrt{u^2 + v^2}}{8} \quad (3)$$

$$\frac{\tau_{by}}{\rho} = f \frac{v\sqrt{u^2 + v^2}}{8} \quad (4)$$

314 where f is the Darcy-Weisbach bed friction coefficient.

315 The Darcy-Weisbach formulation is used in both models, but the friction coefficient f of the bottom
 316 and side-walls is estimated by the Colebrook-White formula (Eq. (5)) (Idel'cik, 1969) in Model 2 and by
 317 its explicit equivalent formula (Eq. (6)) (Yen, 2002) in Model 1.

$$\frac{1}{\sqrt{f}} = -2 \log \left(\frac{k_s}{14.8h} + \frac{2.51}{\text{Re}\sqrt{f}} \right) \quad (5)$$

318

$$f = \frac{1}{4} \left[-\log \left(\frac{k_s}{12h} + \frac{6.79}{\text{Re}^{0.9}} \right) \right]^{-2} \quad (6)$$

319 where k_s is the roughness height and Re is a Reynolds number $\text{Re} = 4\sqrt{u^2 + v^2}h/\nu$ with ν the kinematic
 320 viscosity of water.

321 Although both models were derived by depth-averaging the Reynolds-averaged Navier-Stokes
322 equations, together with Boussinesq's assumption for expressing the depth-averaged turbulent stresses, they
323 differ by the type of turbulence closure used. Model 1 is based on a zero-order turbulence closure, in which
324 the eddy viscosity, ν_t , is estimated by Elder's formula: $\nu_t = \lambda h u_*$, with u_* the friction velocity computed
325 from the free surface slope and λ a parameter set by the user with a default value of 1 (Mejia-Morales et
326 al., 2020). In Model 2, a second-order turbulence closure is implemented. It consists in a two-length-scale
327 depth-averaged k - ϵ turbulence model, as detailed by Ercicum et al. (2009) and Camnasio et al. (2014).

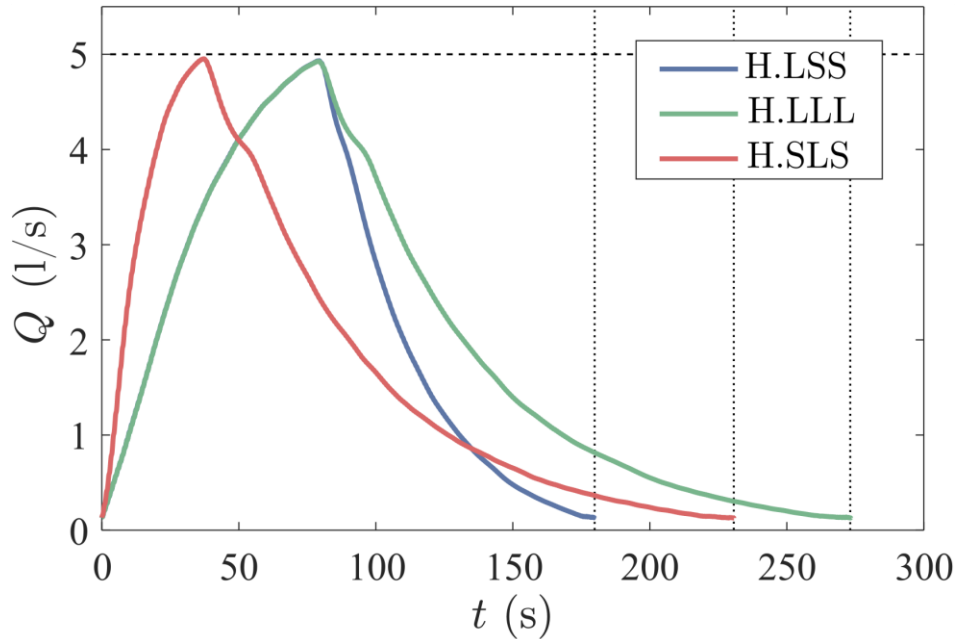
328 *2.3.2. Numerical discretization*

329 In both models, the computational domain was meshed with a Cartesian square grid aligned with the
330 street sidewalls. Depending on the model run, the grid spacing, Δx , was varied between 5 mm and 30 mm
331 with the resulting ratio of the grid size to the length of one opening in the porous block, L_{op} , ranging from
332 1/2 to 1/12. Both models are solved with a finite volume technique. In Model 1, a Godunov type scheme is
333 used (Mignot et al., 2008), while Model 2 is based on a flux-vector splitting technique (Ercicum et al.,
334 2010). In both models, the variables at the cell edges are evaluated from a linear reconstruction, achieving
335 second-order accuracy in space. For steady flow calculations, the models are run in unsteady mode until a
336 steady state is reached. The time step used in the simulations is of the order of 10^{-3} seconds, as it is
337 constrained by the Courant-Friedrichs-Lewy stability condition.

338 *2.4. Boundary and initial conditions*

339 The computational domain was delimited by three types of boundaries: sidewalls, inlets, and outlets.
340 At each sidewall, the component of the specific discharge normal to the sidewall was set to zero. At the
341 inlets, the specific discharge in the streamwise direction was prescribed, and the normal component of the
342 specific discharge was set to zero. The two inlets that are considered in the Left Street and Right Street
343 were positioned at a distance of 2.94 m upstream of the uppermost street intersections (Figure 1), i.e., at the
344 location of the honeycomb grid at the entrance of each street in the experiments.

345 For the steady flow cases in the first and second series of tests (Figure 2a and b), steady inflow
346 discharges were prescribed: $Q_{in_1} = 4.5$ l/s and $Q_{in_2} = 2.0$ l/s (Figure 1) in consistency with the measured
347 values. For the unsteady flow cases in the third test series (Figure 2c), the inflow discharge was fed only
348 through the Right Street as a sequence of 50 consecutive identical flood waves. Three different floodwaves
349 were tested (Figure 3) and each one was examined separately. Each floodwave had the same peak flow of
350 5 l/s (Figure 3) but was characterized by a different unsteadiness degree (Mejia-Morales et al., 2022a). The
351 floodwaves were distinguished based on the rising discharge time, the falling discharge time, and the total
352 volume of floodwater, while their names were formed by using an “L” or an “S” for large and small
353 magnitude for each one of the floodwave characteristics, respectively. For example, H.LSS denotes a
354 hydrograph with large rising discharge time, small falling discharge time, and small total volume of
355 floodwater. As a reference case, steady flow experiments with inlet discharge of 5 l/s (i.e., equal to the peak
356 of the floodwaves) through the Right Street were also carried out in the geometrical setup of test series 3
357 (Figure 1b with the urban blocks of Figure 2c).



359

360 **Figure 3.** Unsteady hydrographs used as inlet discharge in the Right Street (Figure 1b) for the porous blocks
 361 of Figure 2c.

362 At the outlets, the outflow discharge was prescribed as a function of the computed flow depth. The
 363 outlet boundaries were positioned as follows (Figure 1):

- 364 • in the Right Street and the Left Street, at a distance of 0.6 m downstream of the easternmost street
 365 intersection.
- 366 • in the Upstream Street and the Downstream Street, at 1.94 m downstream of the northernmost street
 367 intersection.

368 For test series 1 and 2 (Figure 2a and b), the outflow discharge, Q_0 , in each outlet was determined from
 369 the following weir formula (e.g., Roger et al. (2009)):

$$Q_0 = LC_D \sqrt{2g(h-w)^3} \quad (7)$$

370 where L is the weir length, C_D is the discharge coefficient, and w is the weir height.

371 The implementation of Eq. (7) is slightly different in the two models:

- 372 • in Model 1, the value of L is set equal to the mesh size, and distinct values of Q_0 are computed at
373 each cell edge along the outlet boundary as a function of the flow depth computed at the relevant
374 cell;
- 375 • in Model 2, the length L is taken equal to the actual weir length (i.e., the street width b) and a single
376 value of Q_0 is evaluated, assumed uniformly distributed over the weir length, as a function of the
377 average of the computed flow depths over the cells next to the outlet boundary.

378 For test series 3 (Figure 2c), the downstream boundary condition was set to critical flow for all the
379 edges of an outlet because the flow goes directly from the street to the outlet tank without a weir.

380 In the steady flow runs of Model 2, the initial condition was either a converged solution from a previous
381 run or a calm body of water with an initial flow depth equal to 0.05 m. For Model 1, the initial condition
382 for the steady flow calculations was a water level close to the experimental value and for the unsteady flow
383 calculations was zero flow depth across the flow domain.

384 3. Results and discussion

385 3.1. Sensitivity analysis and calibration of the numerical models

386 Model 2 was used systematically in a series of preliminary computations to assess the effect of the
387 variation in the (i) grid spacing, Δx , (ii) roughness height, k_s , (iii) discharge coefficient, C_D , of the weirs at
388 the outlets, and (iv) initial conditions. Model 1 was also used in these preliminary computations, but not in
389 a systematic way. Moreover, Model 1 was used to verify whether considering a theoretical bottom
390 topography (flat bed) instead of the real one influences the results. These sensitivity analyses were
391 conducted for a single geometric configuration (C19-12 in Figure 2a), which includes the largest number
392 of openings and leads to the most complex flow fields. The comparison of the computed, y_i^c , and observed,
393 y_i^o , hydraulic variables was carried out based on the bias and the root mean square error (RMSE) (e.g.,
394 Chen et al. (2010)):

$$\text{bias} = \frac{\sum_{i=1}^N (y_i^c - y_i^o)}{N} \quad (8)$$

395

$$\text{RMSE} = \sqrt{\frac{\sum_{i=1}^N (y_i^c - y_i^o)^2}{N}} \quad (9)$$

396 where N is the number of points where both measured and modelled data were available.

397 *3.1.1. Grid spacing*

398 The grid cell size for Model 2 was selected after repeating the computations for C19-12 three times
399 with all parameters being kept the same except the grid cell size. The three mesh grids that were tested had
400 square grid cells with side length, Δ , equal to 30 mm, 10 mm, and 5 mm, respectively. The bias and RMSE
401 of the flow depths and velocities for different areas of the model were significantly reduced when the grid
402 cell size was reduced from 30 mm to 10 mm but did not vary much when the cell size was further reduced
403 from 10 mm to 5 mm (Figure S1a in the Supplementary Material). Figure S1a in the Supplementary
404 Material also confirms the second order accuracy of the finite volume numerical scheme implemented in
405 Model 2, consistently with the linear reconstruction used in this model.

406 However, the features of the simulated flow velocity patterns (i.e., number and size of recirculating
407 flow areas) within the porous block were more consistent with the features of the measured patterns when
408 the cell size was 5 mm (Figure S2a in the Supplementary Material), even though some flow recirculations
409 were not captured entirely. Therefore, the 5 mm cell size was kept for the rest of the analyses with Model 2.

410 Model 1 exhibited similar behavior with Model 2 when varying the cell size with the rest of the
411 parameters being kept the same, however, with Model 1 the flow velocity patterns were similar for mesh
412 sizes of 10 mm and 5 mm (Figure S3a in the Supplementary Material). Thus, to reduce computational times,
413 the 10 mm mesh was kept for the rest of the analyses with Model 1.

414 With these mesh configurations, the computed flow depths exhibited a systematic bias compared to the
415 observations, which motivated the extension of the sensitivity analysis to the roughness height and the
416 discharge coefficients of the weir outlets.

417 *3.1.2. Roughness height*

418 The roughness height was taken at a small value corresponding to the PVC surface of the laboratory
419 model. The tested values of k_s were equal to 2×10^{-4} m, 8×10^{-5} m, and 3.6×10^{-5} m. This sensitivity
420 analysis was conducted with Model 2, with $\Delta x = 5$ mm and $C_D = 0.527$ for all outlets, with a previously
421 converged flow field as initial condition. The three tested values for the roughness height did not affect
422 significantly the flow depths and velocities results (Figure S1b in the Supplementary Material) nor the flow
423 patterns (Figure S2b in the Supplementary Material). The flow depth bias and RMSE values for the lowest
424 value of k_s were slightly lower compared to the other k_s values, but at the same time the flow velocity bias
425 and RMSE values slightly increased. The k_s value of 3.6×10^{-5} m was calibrated from water surface
426 measurements in a single street without openings. Considering the very small influence of the tested k_s
427 values on the simulated results with Model 2, a similar sensitivity analysis was not repeated with Model 1
428 and $k_s = 3.6 \times 10^{-5}$ m was used in both models.

429 *3.1.3. Discharge coefficient of the weirs*

430 The computations presented in Section 3.1.1 used discharge coefficients that were experimentally
431 derived from the laboratory tests. However, the location where the flow depth is measured upstream of the
432 weirs in the lab does not correspond exactly to the location where the Model 2 considers flow depth for
433 estimating the outflow discharge. Hence, the discharge coefficient, C_D , which lumps all flow processes in
434 the near field of the weirs (including vertical acceleration, which cannot be represented explicitly by shallow
435 water equations) was recalibrated so that the computed flow depths agree on average with the observations.
436 To this end, several values of C_D were tested. The lowest difference between modelled and measured flow
437 depths for Model 2 was obtained with $C_D = 0.453$, and thus this value was selected for the rest of the
438 numerical simulations using Model 2. For Model 1, the lowest difference between modelled and measured

439 flow depths was obtained with $C_D = 0.467$ and this value was chosen for the rest of the simulations with
440 Model 1, although a value of 0.55 for Outlets 1 and 2 and 0.53 for Outlets 3 and 4 led to a better distribution
441 of the outflows. This was also the case for all the urban blocks in Figure 2a. Nevertheless, the effect of C_D
442 on the street and block intrusion discharges and on the flow patterns (Figure S2c and Figure S3b in the
443 Supplementary Material) is rather small. The small difference between the chosen discharge coefficients
444 for the two models may be attributed to the different ways that the downstream boundary conditions were
445 implemented in the models and to the different turbulent closures.

446 *3.1.4. Initial conditions*

447 A converged solution for a steady flow simulation may depend on the initial conditions (Dewals et al.,
448 2012), particularly in the presence of complex patterns of recirculating flow. Therefore, by using Model 2
449 for the case with the C19-12 block (Figure 2a), we repeated the computations for two different initial
450 conditions: (i) the computed steady flow field obtained with the experimentally derived discharge
451 coefficient (i.e., a previously converged solution) and (ii) water at rest with flow depth equal to 5 cm. As
452 expected, the initial condition influenced the computed steady flow field. For the flow in the porous block,
453 the results obtained when the computations were initiated with water at rest agree better with the
454 observations (Figure S1c and Figure S2d in the Supplementary Material). This initial condition setting was
455 kept for the rest of the analysis for Model 2 while the initial condition for Model 1 was a water level close
456 to the experimental value. For Model 1 the results were generally independent of the initial conditions, but
457 exceptions could be found for the more complex patterns inside the block.

458 The simulation parameters obtained from the sensitivity analysis are summarized in Table 2 and these
459 parameters were used for the numerical modelling of the rest of the experimental configurations.

460 **Table 2.** Calibrated parameters used for the numerical modelling of all cases.

	Model 1	Model 2
Cell size, Δx	10 mm	5 mm
Initial conditions	Water level close to experimental value	Water at rest
Roughness height, k_s	3.6×10^{-5} m	3.6×10^{-5} m
Outlet weirs discharge coefficient, C_D	0.467	0.453

461

462 *3.1.5. Topography*

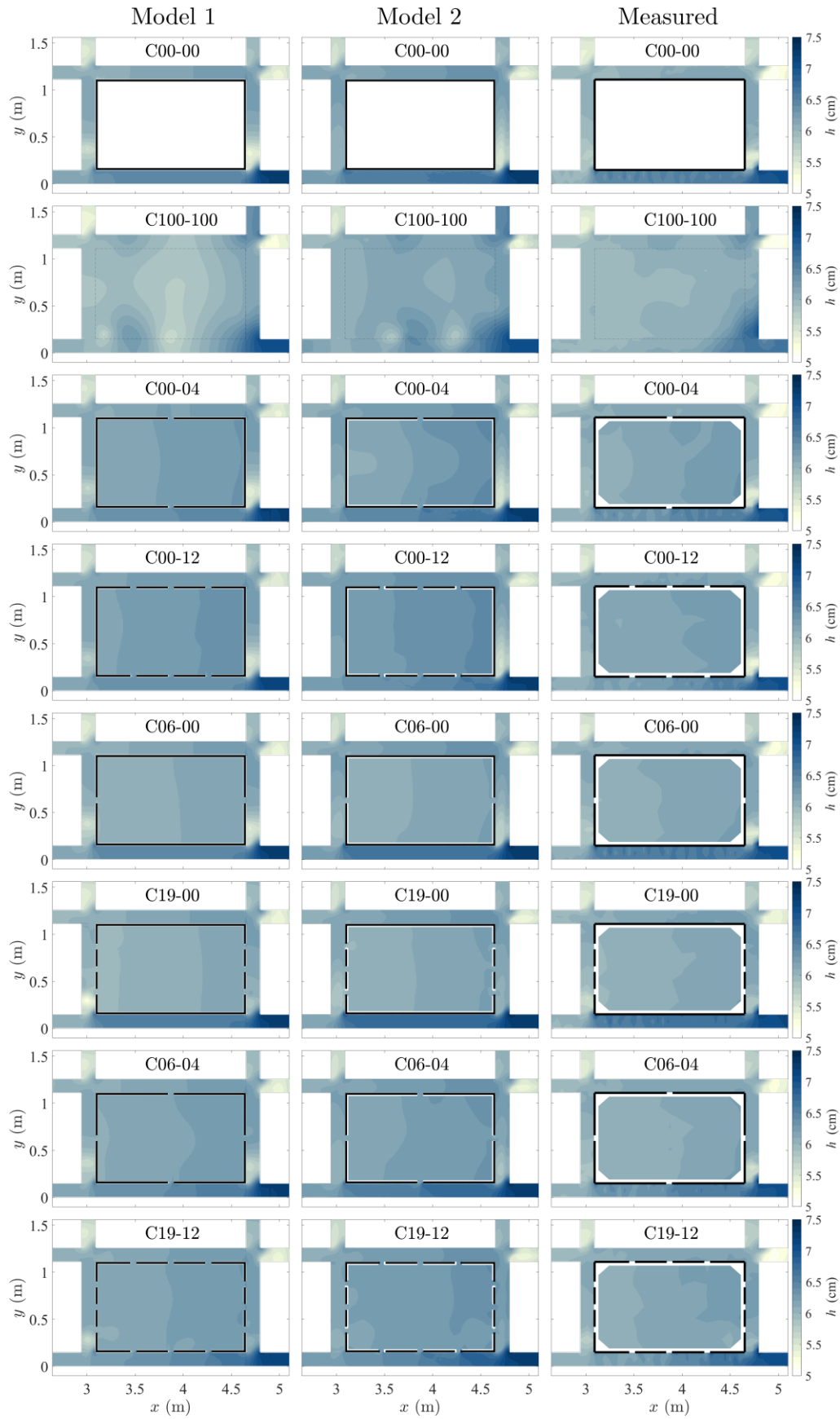
463 The topography of the experimental platform may change in time since it was constructed with boards
 464 supported by beams. For most numerical calculations, the theoretical topography of an inclined plane with
 465 a constant slope in the x direction of 0.12% was used. However, two detailed topographies that were
 466 surveyed in 2019 (before the first series of experiments, i.e., Figure 2a) and in 2021 (between the second
 467 and third series of experiments, i.e., Figure 2b and Figure 2c, respectively) showed some elevation
 468 differences compared to the theoretical topography, and between the two topographical surveys, of less
 469 than 2 mm. The effect of this change in topography was tested using Model 1 and $C_D = 0.4$. Results show
 470 a weak influence on the flow velocity pattern and all the other results (Table S1 in the Supplementary
 471 Material), thus, the theoretical topography was used for the rest of the cases.

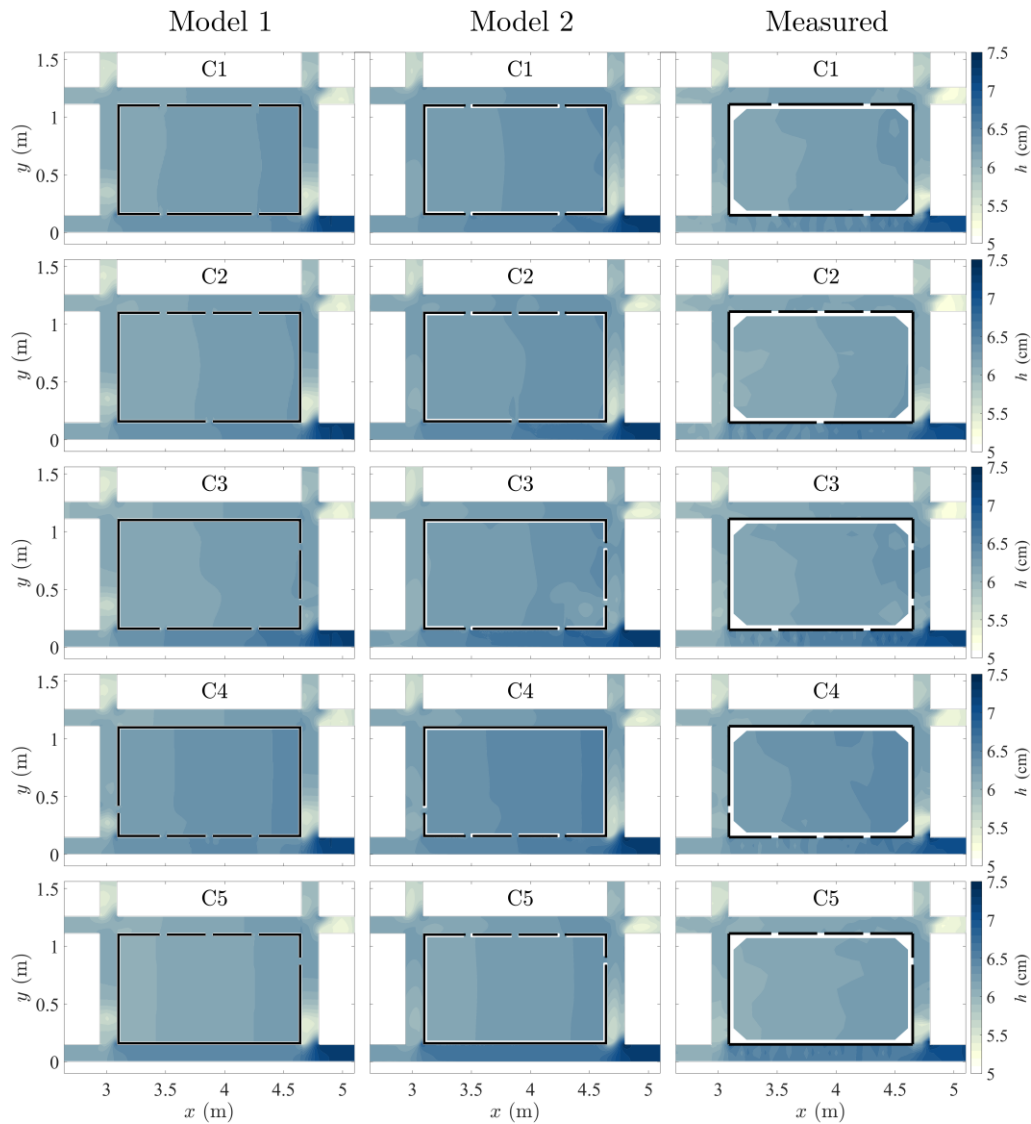
472 *3.2. Steady flow tests*

473 *3.2.1. Flow depths*

474 Figure 4 shows that both models, and hence the 2D SWE, are able to reproduce fairly accurately the
 475 measured flow depth patterns for cases with steady flow (Figure 2a and b). There is a flow depth difference
 476 between the Right and Left Streets because the weir height in Outlet 1 is larger than in Outlet 2. The larger
 477 flow depths in the Right Street compared to the Left Street induce a pressure gradient that enhances the
 478 transverse flow through the porous block openings.

479





481

482 **Figure 4.** Flow depths modelled with Model 1 (left column), Model 2 (middle column) and measured (right column) for steady flow conditions. The first eight configurations are from Mejia-Morales et al. (2021).
 483

484

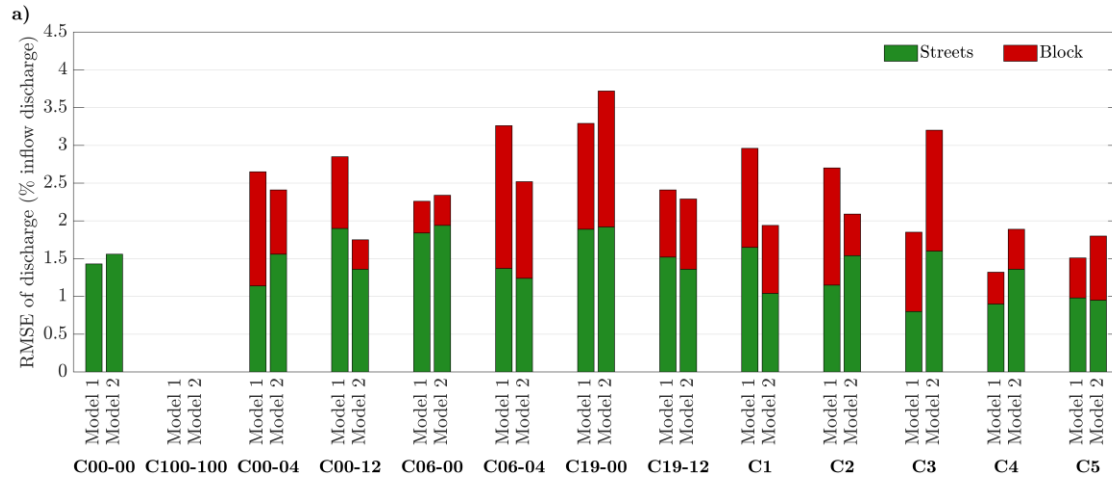
485 Both models are capable to reproduce the increasing flow depth at the Right Street, the decreasing flow
 486 depth at the Left Street, and the relatively constant water level within the block, which is a result of the very
 487 low velocities within the block. The differences between the results of the two models are minimal both
 488 within the porous block and in the streets, which implies that at a large scale the turbulence closure model
 489 does not affect the flow depth predictive capabilities of a 2D SWE model in urban floods with steady flow.

3.2.2. Discharge partition

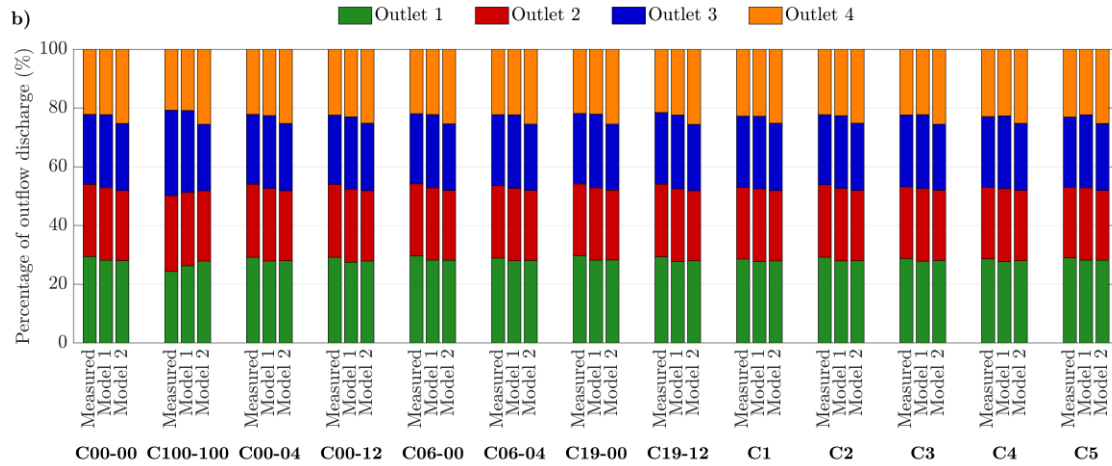
490
491 The two models reproduce well the discharge partition both in the streets and within the porous block
492 without any of the two exhibiting clearly superior performance (Figure 5a). Model 1 predicts more
493 accurately the discharge partitioning at the four outlets with a RMSE that is less than half of that of Model 2
494 (Figure 5c). Model 2 overestimates Q_{out_4} and both models underestimate Q_{out_1} , except for the case C100-
495 100 (configuration without a block), and approximate well Q_{out_2} (Figure 5b). The two models exhibit a
496 different behavior in Outlet 3, with Model 1 overpredicting and Model 2 underpredicting Q_{out_3} (Figure 5b).
497 Overall, Model 1 and Model 2 miscalculate the discharge distribution at the outlets by 2.5% and 7.3% on
498 average, respectively. In the streets surrounding three of the most complex porous blocks (C06-04, C19-
499 12, C3), Model 2 overestimates the discharge in the Right Street, which is the street that conveys most of
500 the discharge, while Model 1 exhibits a more erratic pattern with this discharge (Figure 6). The street that
501 conveys the second largest discharge in these three cases is the Downstream Street, in which both models
502 give good results, besides Model 2 overpredicting the discharge in C19-12. The overpredictions of Model 2
503 and underpredictions of Model 1 at the large discharges in the Right and Downstream Streets are partially
504 compensated by respective underpredictions and overpredictions of the two models at the street with the
505 smallest discharge, i.e., the Upstream Street (Figure 6). The discharge distribution for all cases is presented
506 in Figure S4 in the Supplementary Material. Overall, the maximum discharge deviation occurs for C100-
507 100 (Figure 5c). Similar disagreements between measurements and 2D SWE computations in large open
508 areas were also noted by Li et al. (2021a).

509 Generally, the flow distribution at the outlets corresponds to the experimental ones (error less than 2.5%
510 of the total inflow except the case C100-100) but this distribution is relatively constant due to the general
511 configuration of the street network. Flow discharges in the streets and through the openings of the block
512 are more influenced although the RMSE remains below 2% of the total discharge. However, due to the
513 small portion of the flow that enters the block, the relative error can be high for the flow passing through
514 the building (Figure S4 in the Supplementary Material).

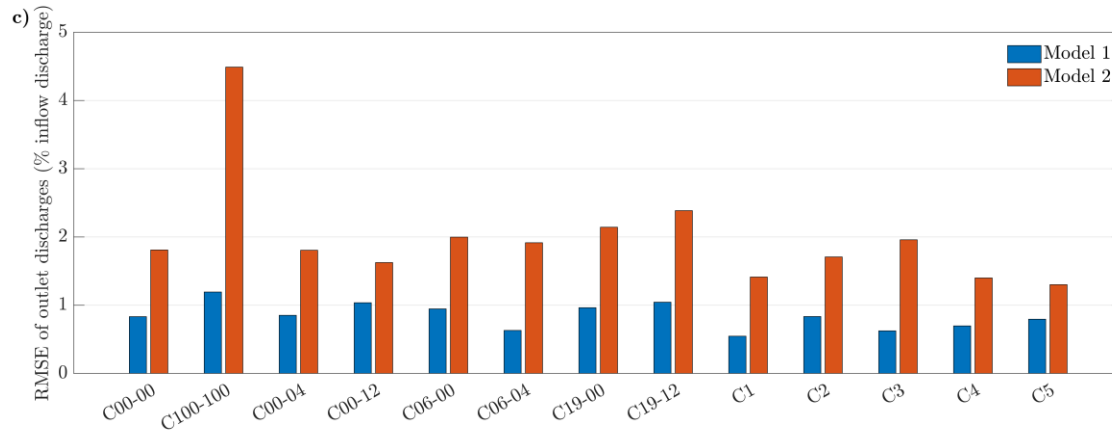
515



516



517

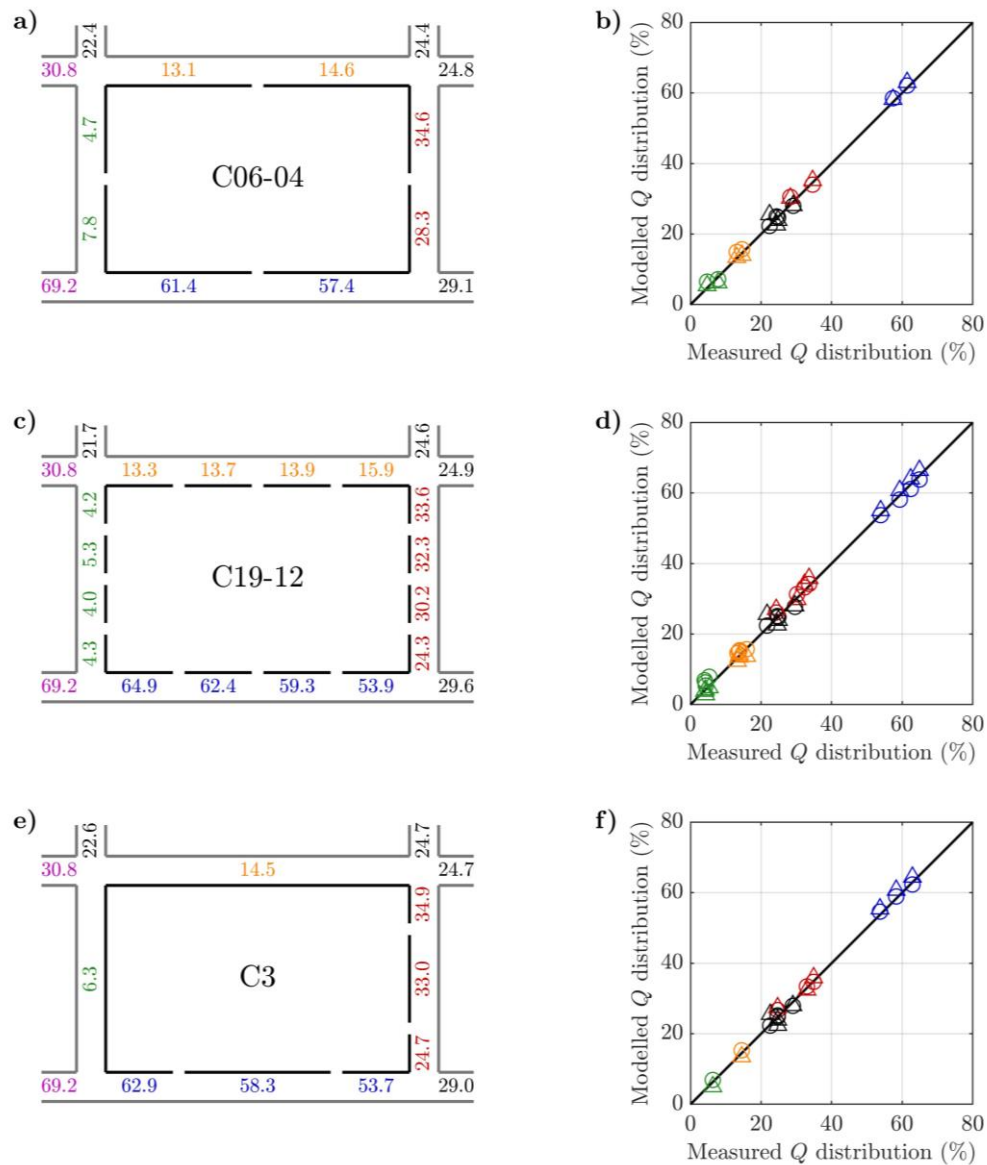


518

519 **Figure 5.** (a) RMSE of flow discharge for Model 1 and Model 2 in the urban block and in the surrounding
 520 streets, (b) Discharge distribution at the four outlets and (c) RMSE between modelled and measured outlet
 521 discharges at the four outlets for the steady flow cases. No data are presented for C100-100 in (a) because
 522 this case does not have a block.

523

524



525

526 **Figure 6.** (a, c, e) Measured discharge distribution around the urban block and at the outlets for selected
 527 cases with steady flow conditions and (b, d, f) comparison between measured and modelled discharges with
 528 Model 1 (circles) and Model 2 (triangles). The colored symbols in each scatter plot of the right column
 529 correspond to the discharges with the same color in the subfigure next to each scatter plot in the left column.

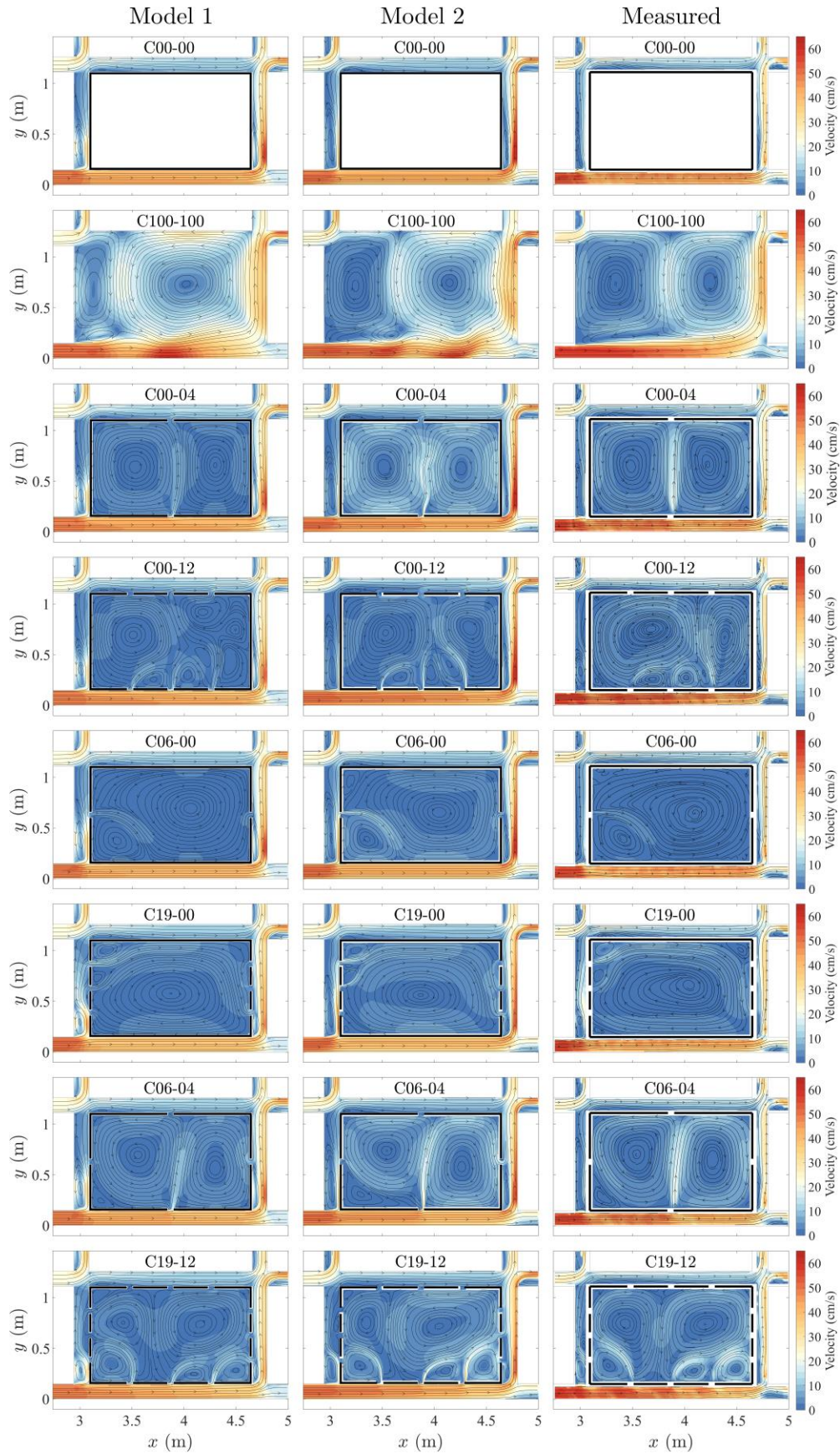
3.2.3. Velocity flow fields

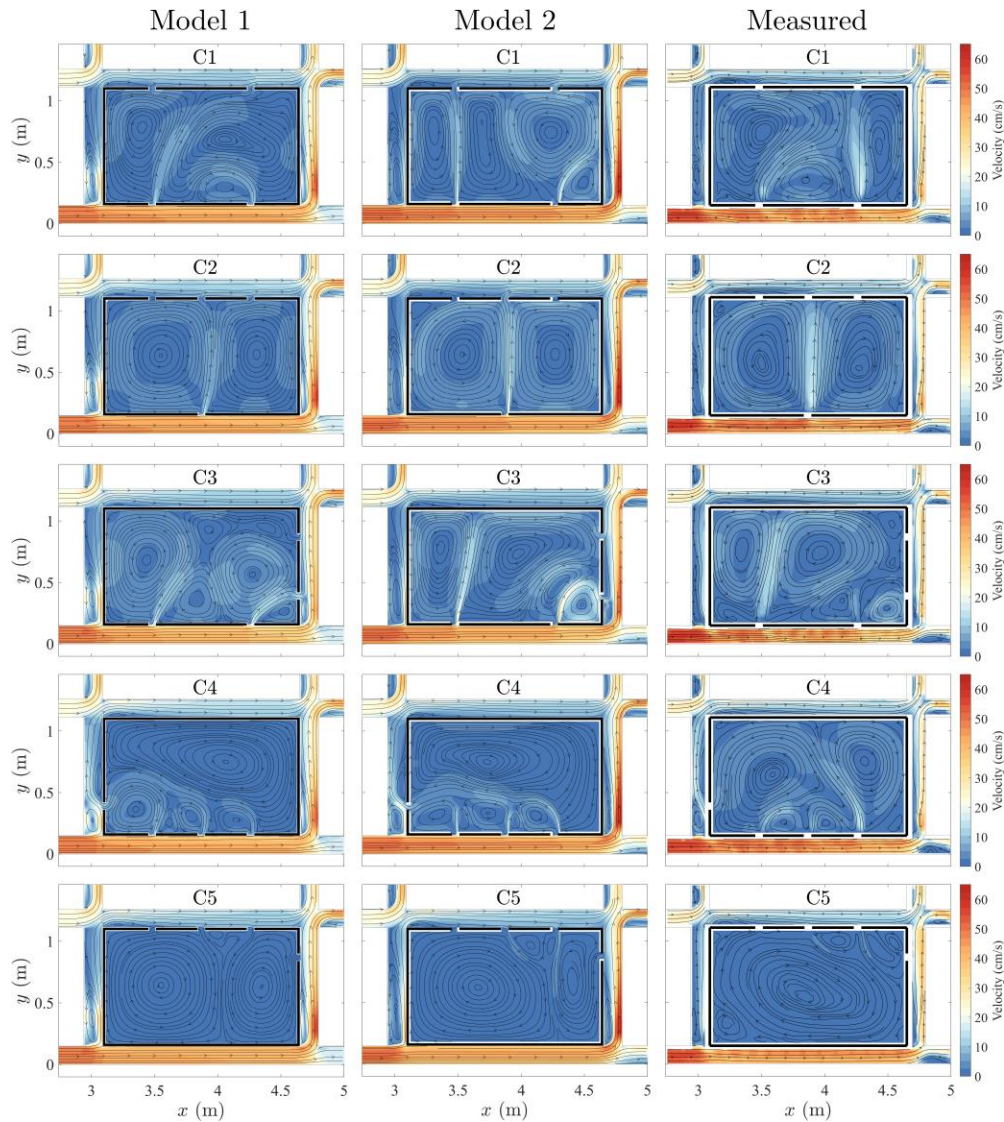
530
531 In this section, the depth-averaged flow velocities modelled with 2D SWE are compared to the surface
532 velocities measured with LSPIV. Mejia-Morales et al. (2021) compared the LSPIV surface velocity
533 measurements to ADV measurements across the flow depth and showed that the surface velocities are
534 mostly well-approximated by depth-averaged velocities. Starting with the two reference cases C00-00 (non-
535 porous block) and C100-100 (no block), the two models reproduce qualitatively all the flow features that
536 were observed in the experiments (Figure 7). In C00-00, the interaction of the flows from the different
537 branches at the junctions matches the measurements well, with a correct distribution of the discharge
538 between the outlets (Figure 5c). In C100-100, even though the modelled discharge distribution at the outlets
539 exhibits the largest deviation from the measurements (Figure 5c), the two models reproduce fairly well,
540 particularly Model 2, the two large recirculation zones. However, they are uneven compared to the
541 measurements, with the downstream and upstream recirculation zones being modelled larger and smaller,
542 respectively, than what was observed.

543 The modelled flow patterns within and around the porous blocks in the first test series (Figure 2a) agree
544 well with the measurements, with the number and direction of the recirculation zones being modelled
545 correctly in almost all cases (Figure 7). For the cases with no more than one opening per side, i.e., C00-04,
546 C06-00, and C06-04, only Model 2 in C06-04 exhibits a notable difference in the size of the recirculation
547 zone in the lower left corner. When there are three openings at two opposite sides of the porous block, the
548 flow pattern becomes much more complex. The two models are still able to simulate the direction of the
549 streamlines quite correctly but the sizes of some of the recirculation zones are a little different than the
550 measured ones. For C00-12, Model 1 adds two small recirculation zones at the right part of the block and
551 Model 2 augments one in the center.

552 The second test series of steady flow cases (presented in Figure 2b) generally exhibits complex flow
553 recirculations (Figure 7) because of the several openings on one side of the block, in each case, and the
554 asymmetric distribution of the other openings at another side of the porous block. The case C1 is the only

555 exception in the sense that it has two symmetric openings at the sides at the Right Street and Left Street.
556 However, the flow pattern within the block for C1 is quite complex with three main uneven recirculation
557 zones that the two models cannot reproduce in their correct location; moreover, the two models do not
558 obtain the same pattern. In case C2, from the three openings at the Left Street, the middle one influences
559 the flow pattern the most and the flow pattern in the porous block resembles C00-04. The two models
560 reproduce this pattern accurately. Cases C3 to C5 are the more complex ones and the two models are not
561 always able to reproduce entirely the observed flow patterns. The left part of the pattern in C3 is generally
562 well reproduced by Model 1 but the right part with an interaction of three openings is not similar to the
563 measurements. On the other hand, Model 2 predicts quite accurately the flow pattern in C3. Case C4 is the
564 most challenging one: the two models provide similar patterns but fail to accurately predict the shape and
565 size of the recirculation zones. As a result, the two observed large counter-rotating recirculation zones are
566 modelled as one and the two smaller ones next to the Right Street have the opposite directionality. The
567 structure of the smaller recirculation zones from the models seems more influenced by the opening at the
568 Upstream Street, compared to the measurements. On the contrary, in a mirrored configuration, the modelled
569 flow patterns in C5 (relatively similar for the two models) seem less influenced by the opening in the
570 Downstream Street compared to the measurements, and as a result the recirculation zone at the right side
571 of the block is modelled larger than what it actually is.





573

574 **Figure 7.** Time-averaged surface velocities modelled with Model 1 (left column), Model 2 (middle column)
 575 and measured (right column) for steady flow conditions. The first eight configurations are from Mejia-
 576 Morales et al. (2021). The modelled flow velocity patterns (left and middle columns) are based on depth-
 577 averaged velocities while the measured flow velocities are surface flow velocities.

578

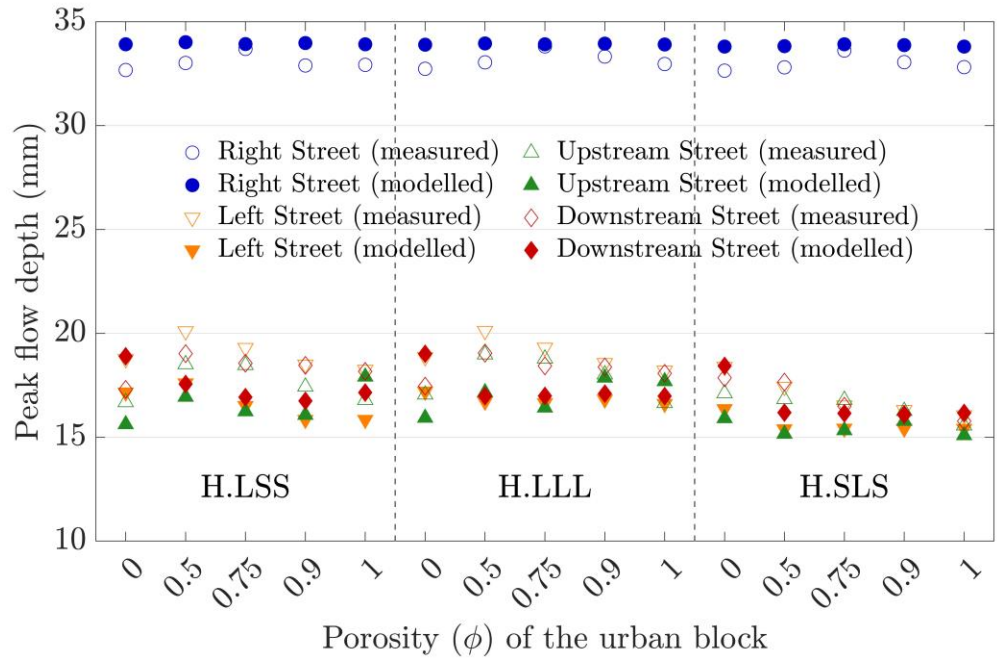
579 3.3. Unsteady flow tests

580 3.3.1. Flow depths

581 The unsteady flow simulations were carried out only with Model 1. The presence of hydraulic jumps
 582 at different locations in the experiments and in the calculations, causes a lower agreement of peak flow
 583 depths compared to the steady flow cases, with an average deviation of 6.7% between calculations and

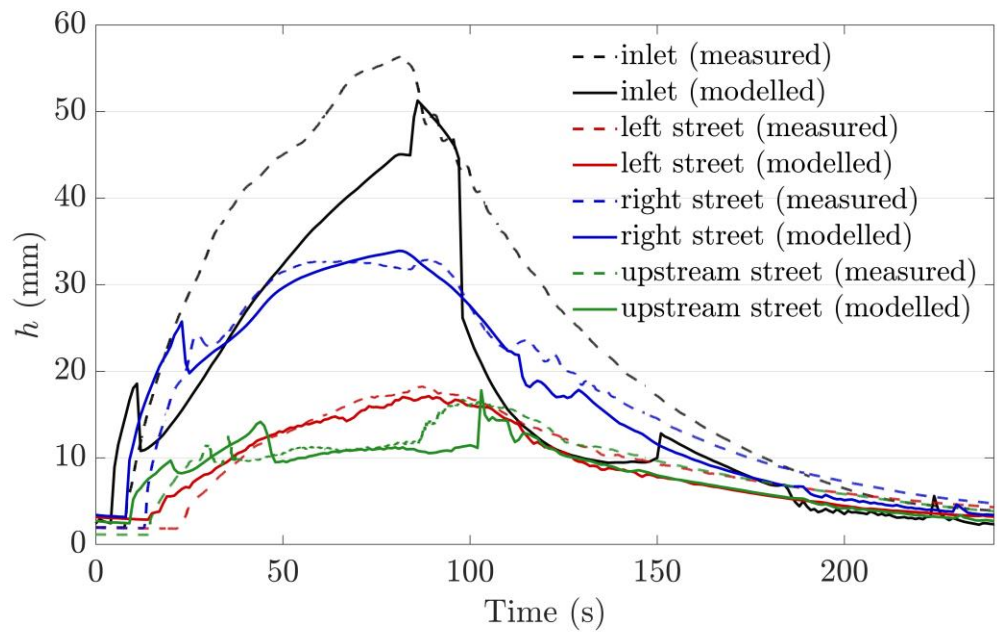
584 measurements in the streets around the block. Model 1 slightly overestimates the peak flow depth in the
585 Right Street, which is the highest peak flow depth in the test domain, with an error of less than 4% (Figure
586 8). The model performs best in the Right Street for $\phi = 0.75$, for every tested hydrograph (H.LSS, H.LLL,
587 and H.SLS). No trend is detected between the rest of the block porosities and the performance of the model
588 in predicting peak flow depths in the Right Street. The absolute error in the other three streets around the
589 block is similar to that in the Right Street; however, the peak flow depth is lower and thus, percentagewise
590 Model 1 is less accurate in predicting flow depths there. In these three streets, Model 1 predicts flow depths
591 best in H.SLS (the hydrograph with the greatest unsteadiness), followed by H.LLL and H.LSS. The
592 predictive performance of the model in the H.SLS hydrograph deteriorates with decreasing block porosity,
593 whereas for H.LLL and H.LSS there is a more erratic pattern on the agreement between depth modelling
594 results and measurements. For all flow cases, the flow depth is underestimated in the Left Street (Figure 8)
595 and in the block (Figure S5 in the Supplementary Material).

596 Figure 9 shows how the flow depth evolves in time at different measuring locations (Figure 1b) of the
597 test domain for the hydrograph H.LSS and $\phi = 1$, i.e., the block without any interior obstruction. The model
598 captures the evolution of the flow depths in the Right, Left, and Upstream Street relatively accurately after
599 the first 60 seconds, particularly in the rising limb of the hydrograph; however, it cannot correctly reproduce
600 the flow depth at the location P_{in} .



601

602 **Figure 8.** Measurements and calculations with Model 1 of peak flow depths in the streets around the porous
 603 block (locations P_{RS} , P_{LS} , P_{US} , and P_{DS} in Figure 1b for the Right, Left, Upstream, and Downstream Street,
 604 respectively) for the three cases with unsteady hydrographs (H.LSS, H.LLL, and H.SLS). The tested urban
 605 blocks and their respective porosities are shown in Figure 2c. The vertical dashed lines separate the data
 606 for each flow case.



607

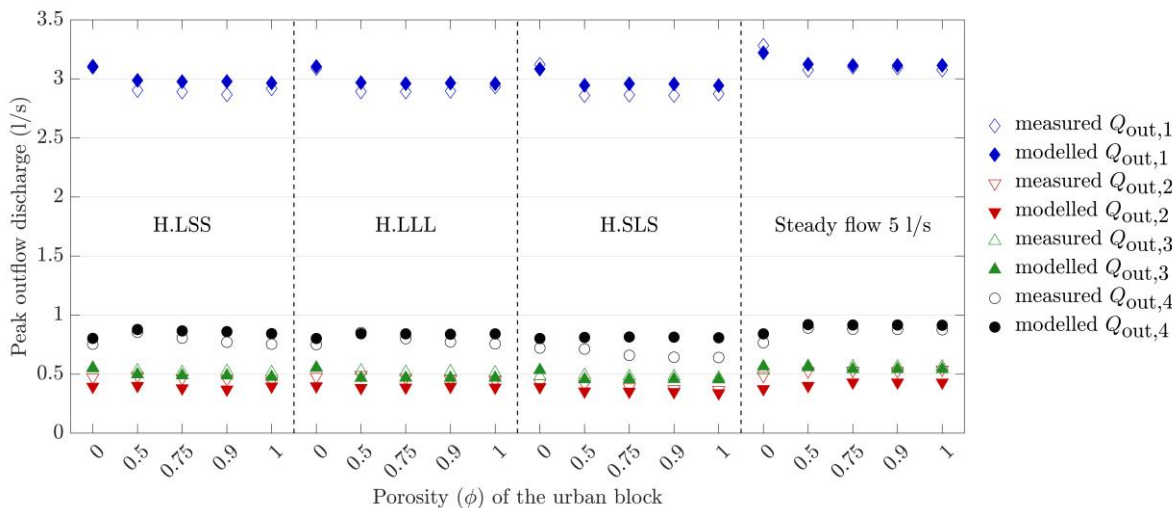
608 **Figure 9.** Measured and calculated (with Model 1) flow depths (locations P_{in} , P_{RS} , P_{LS} , and P_{US} in Figure
 609 1b for the inlet and the Right, Left, and Upstream Street, respectively) as a function of time for the H.LSS
 610 discharge hydrograph with porosity $\phi = 1$ (series 3).

611 *3.3.2. Discharge partition*

612 For steady flow in the configurations of test series 3 (Figure 2c), the discharge at Outlet 4 is
613 miscalculated by approximately 0.05 l/s on average, while the discharge at Outlet 2 is underestimated by
614 about 0.1 l/s (Figure 10). As for test series 1 and 2 (Figure 2a, b), the downstream boundary conditions
615 should be adapted to obtain a more correct distribution. However, it should be noted that changing critical
616 flow to free outflow at Outlets 1 and 2 (in which the flow is partly supercritical) did not change the outflow
617 distribution. The discharges at the outlets for the steady flow case of test series 3 exhibit a slightly increasing
618 trend with increasing porosity in Outlet 2 and rather constant values, besides $\phi = 0$, in the other outlets
619 (Figure 10).

620 For the unsteady flows, the peak outflow discharge in Outlet 1 is consistently higher than the peak
621 discharges in the other outlets for every tested hydrograph and porosity value, as for the respective steady
622 flow test (Figure 10). The outflow in Outlet 1 becomes the highest when the block has no porosity ($\phi = 0$),
623 while it reaches a plateau for each flow case when the block has porosity. For the unsteady cases, Model 1
624 predicts accurately the peak discharge in Outlet 1 for the non-porous block, for every hydrograph, but it
625 overestimates this peak discharge by less than 4% for the porous blocks. Model 1 performs even better in
626 predicting the peak discharge in Outlet 1 in the steady flow case, with a slight underestimation of the non-
627 porous block case and a few overestimations for the porous block cases. The second highest peak outflow
628 discharge occurs in Outlet 4, where Model 1 overestimates the peak discharge by around 0.085 l/s for the
629 non-porous block, for all flow cases (Figure 10). The predictive performance of Model 1 mostly deteriorates
630 with increasing porosity of the block for all three hydrographs, particularly for H.SLS, while this is not
631 observed in the steady flow cases, where only a slight overestimation is noted. The overestimations in
632 Outlets 1 and 4 are partially compensated by some underestimations in the peak outflow discharge in
633 Outlet 2, where, percentagewise, the model predictions deviate from the measurements the most for all flow
634 cases, besides the hydrograph H.SLS. Finally, Model 1 predicts accurately the peak outflow discharge in
635 Outlet 3. Overall, for all unsteady cases the average discrepancy between calculations and measurements

636 of the peak discharges at the outlets is 8.6%. A comparison between the measured and modelled peak flow
 637 depths at the locations $P_{out1} - P_{out4}$ near the outlets (Figure 1b) is provided in Figure S6 in the
 638 Supplementary Material.

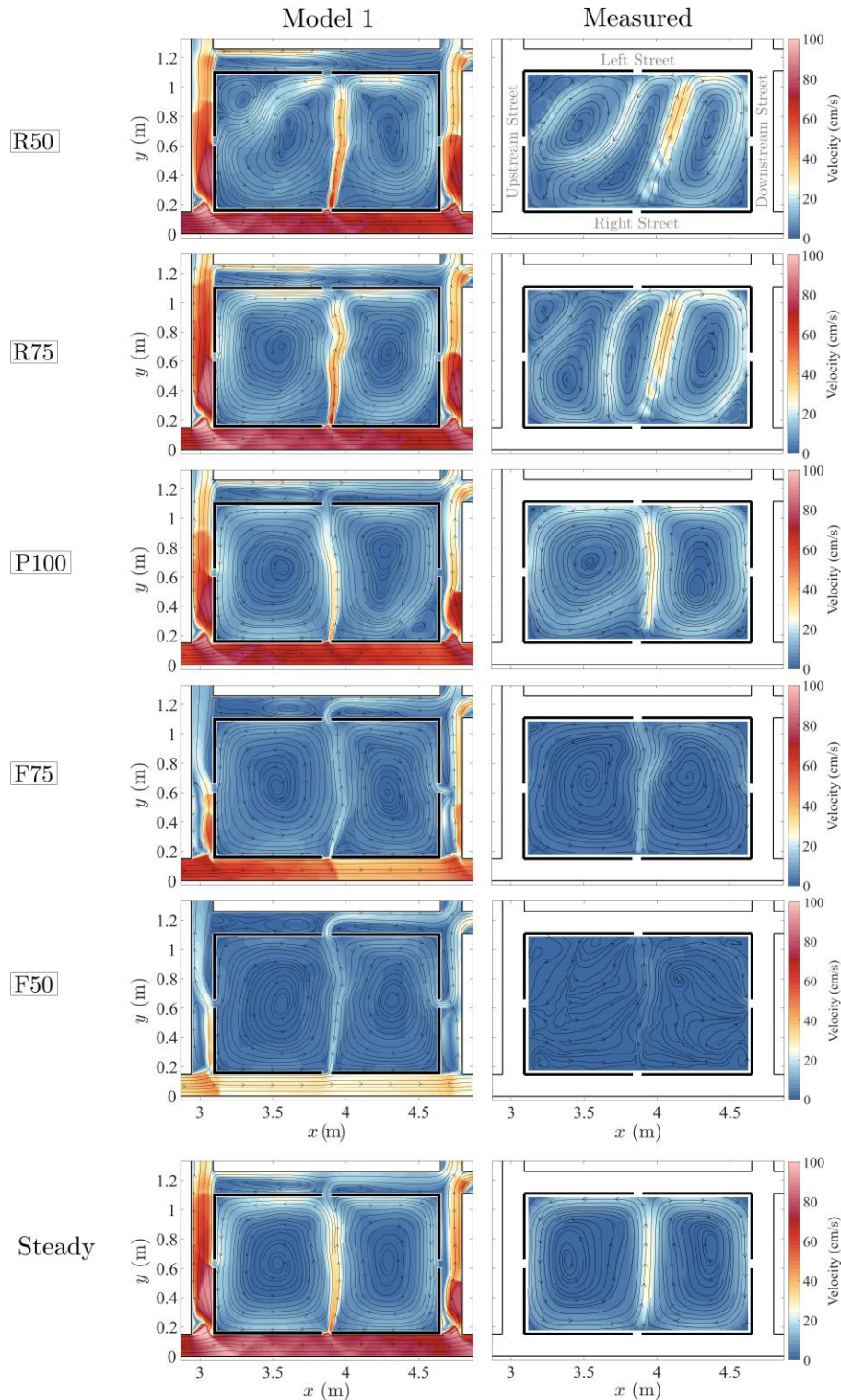


639
 640 **Figure 10.** Measured and calculated (with Model 1) peak discharges at the four outlets of the experimental
 641 setup of Figure 1b for the three cases with unsteady hydrographs (H.LSS, H.LLL, and H.SLS) and a steady
 642 flow case with inflow discharge of 5 l/s, which is equal to the peak value of each unsteady hydrograph at
 643 the inlet. The tested urban blocks and their respective porosities are shown in Figure 2c. The vertical dashed
 644 lines separate the data for each flow case.

645
 646 *3.3.3. Velocity flow fields*

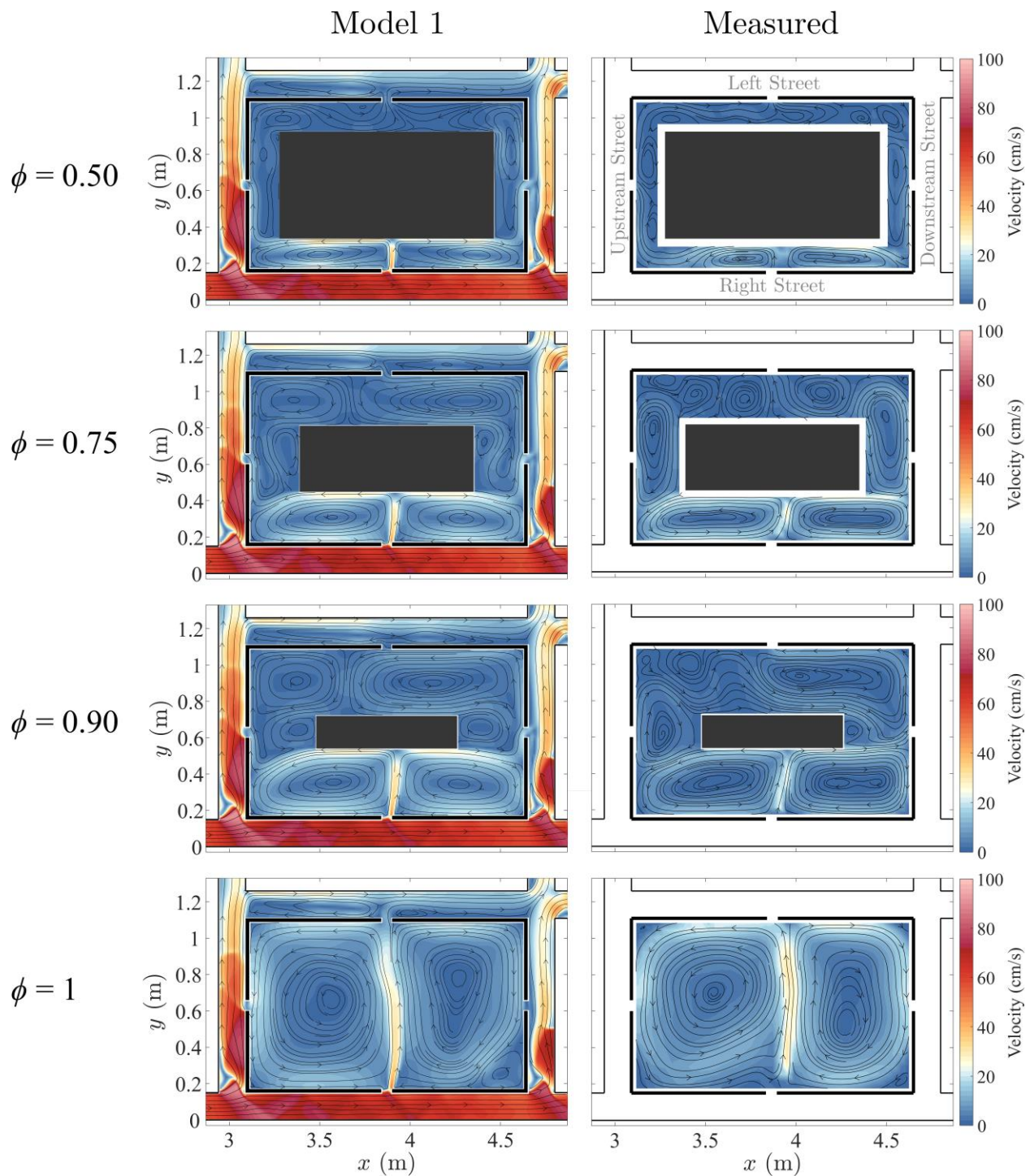
647 As in Section 3.2.3, the depth-averaged flow velocities modelled with 2D SWE are compared to the
 648 surface velocities measured with LSPIV. For $\phi = 1$ in steady flow, the flow pattern of the third series is
 649 similar to C06-04 with two main nearly symmetrical recirculation zones (Figure 11). For the unsteady case
 650 with the hydrograph H.LSS (with the greatest unsteadiness), after the flow peak the flow pattern remains
 651 quite similar for a long time. The initial part of this process is reproduced well by Model 1. Before the flow
 652 peak, the block is filling and the observed flow pattern comprises four main recirculation zones that are not
 653 reproduced by Model 1, which, instead, generates a flow pattern that tends more rapidly to a flow pattern
 654 with two main recirculation zones. Reducing ϕ leads to reduced water volume in the block and an increase

655 in the number of recirculation zones within the porous block, which are fairly well reproduced by Model 1
656 (Figure 12).



657

658 **Figure 11.** Quasi-instantaneous surface velocities modelled with Model 1 (left column) and measured (right
 659 column) for the hydrograph H.LSS and $\phi = 1$. All experimental configurations were obtained from Mejia-
 660 Morales et al. (2022a). In the first column, R, P, and F stand for rising, peak, and falling stage of the
 661 hydrograph, while the numbers 50, 75, and 100 show the ratio of the flow depth to the maximum flow depth
 662 within the porous block at that instant.



664

665 **Figure 12.** Quasi-instantaneous depth-averaged velocities modelled with Model 1 (left column) and surface
 666 velocities measured (right column) at the peak of the hydrograph H.LSS with various values of ϕ . All
 667 experimental configurations were obtained from Mejia-Morales et al. (2022a).

668

669 4. Conclusions

670 Accurate and fast computational tools for the estimation of urban flood hazard are of vital importance.
671 Although in such cases the flow can be 3D in parts of the urban layout, it is important from a management
672 perspective to understand when these 3D processes are dominant and when the flow can be reliably
673 modelled with 2D shallow water equations. In this paper, we demonstrated the capacity of two 2D shallow
674 water flow solvers to simulate urban floods involving flow exchanges with the interior of an urban block
675 in nineteen idealized urban layouts. The computations were compared against published and new
676 experimental observations in steady and unsteady conditions. The tested computational models differed
677 mostly by the turbulence closure used for estimating the eddy viscosity.

678 Both models reproduced accurately the measured flow depth for all cases. The prediction of the
679 discharge distribution and the flow velocity patterns within and around the urban block was in general
680 satisfactory but deteriorated when the flow exchanges between the urban block and the surrounding streets
681 increased and became asymmetrical. The average difference between the modelled discharge distributions
682 and the measurements at the outlets was 2.5% and 7.3% for Model 1 and Model 2, respectively. With
683 respect to the flow velocities, none of the two models outperformed consistently the other, which implies
684 that both tested turbulence closure models are suitable to model the flow patterns within and around an
685 urban block, although with different accuracy at different flow patterns.

686 For unsteady conditions, the difficulties increased because of the occurrence of hydraulic jumps and
687 the sequence of a filling phase and an emptying phase of the block. The error thus rose in parameters such
688 as the peak flow depths in the streets and the peak discharges at the outlets, which were miscalculated by
689 6.7% and 8.6%, respectively. However, the influence of the porosity of the urban block was generally
690 simulated in the right way and except during rapid filling of the block, the computed velocity pattern inside
691 the block reproduced sufficiently well the main process.

692 Even if the discharge partition at the outlets is only a little sensitive to a change in the urban block
693 openings, local modifications of the flow field can be particularly important for urban planning under
694 climate change scenarios, since the building density and the distance between neighboring buildings are the
695 most influential parameters affecting pluvial flooding (Bruwier et al., 2020).

696 The geometric configurations considered here are highly simplified compared to real-world urbanized
697 floodplains, which have considerably more intricate flowpaths, street profiles, opening shapes and indoor
698 arrangement of buildings. In addition, in reality the flow exchanges between the streets and the urban blocks
699 are influenced by obstructions near the openings such as parked cars and street furniture (Mignot et al.,
700 2020) and the interaction of surface flows with surcharging sewers (Kitsikoudis et al., 2021). These aspects
701 highlight the limitations of the present study and need to be investigated in future studies with either large
702 scale experiments or field data to additionally address potential scale effects that affected our results. In
703 practice, evaluating accurately the flow intrusion into buildings and building blocks would require
704 particularly fine mesh resolution in the near field of the opening, or the use of parametrizations such as weir
705 equations. Such aspects affect the operationality of models for simulating large urban floodplains and need
706 to be investigated. The performance of 1D modelling in the streets, combined with side discharge equations
707 for the exchanges through building opening, could also be investigated in a follow-up study.

708 **Acknowledgements**

709 The authors from INRAE and INSA Lyon acknowledge the financial support offered by the French National Research
710 Agency (ANR) for the project DEUFI (under grant ANR-18-CE01-0020). The authors gratefully acknowledge MSc
711 students Yann Nicol and Elliott Crestey who contributed to the numerical computations.

712 **Data availability**

713 All experimental observations used in this research are available at: <https://doi.org/10.57745/UJOCJ8> (Mejia-Morales
714 et al., 2022b).

715 **Authors' contributions**

716 The study was designed by A.P., B.D., S.P., and E.M., who also defined the methodology; all laboratory experiments
717 were conducted by M.M.M., under the supervision of S.P. and E.M.; computations with Model 1 were conducted by

718 A.P. and those with Model 2 by students under the guidance of P.A., B.D., S.E., and M.P. The original draft of the
719 manuscript was prepared by V.K. with the support of B.D., A.P., and M.M.M. It was revised by V.K., B.D., E.M. and
720 S.P.

721 References

- 722 Addison-Atkinson, W., Chen, A. S., Memon, F. A., Chang, T.-J. (2022). Modelling urban sewer flooding
723 and quantitative microbial risk assessment: A critical review. *Journal of Flood Risk Management*
724 **15**(4), e12844. <https://doi.org/10.1111/jfr3.12844>
- 725 Almeida, G. A. M. de, Bates, P., Ozdemir, H. (2018). Modelling urban floods at submetre resolution:
726 challenges or opportunities for flood risk management? *Journal of Flood Risk Management* **11**,
727 S855–S865. <https://doi.org/10.1111/jfr3.12276>
- 728 Arrault, A., Finaud-Guyot, P., Archambeau, P., Bruwier, M., Ercicum, S., Pirotton, M., Dewals, B.
729 (2016). Hydrodynamics of long-duration urban floods: experiments and numerical modelling.
730 *Natural Hazards and Earth System Sciences* **16**(6), 1413–1429. [https://doi.org/10.5194/nhess-16-](https://doi.org/10.5194/nhess-16-1413-2016)
731 [1413-2016](https://doi.org/10.5194/nhess-16-1413-2016)
- 732 Arrighi, C., Oumeraci, H., Castelli, F. (2017). Hydrodynamics of pedestrianstextquotesingle instability in
733 floodwaters. *Hydrology and Earth System Sciences* **21**(1), 515–531. [https://doi.org/10.5194/hess-](https://doi.org/10.5194/hess-21-515-2017)
734 [21-515-2017](https://doi.org/10.5194/hess-21-515-2017)
- 735 Bates, P. D. (2022). Flood Inundation Prediction. *Annual Review of Fluid Mechanics* **54**(1), 287–315.
736 <https://doi.org/10.1146/annurev-fluid-030121-113138>
- 737 Bazin, P.-H., Mignot, E., Paquier, A. (2017). Computing flooding of crossroads with obstacles using a 2D
738 numerical model. *Journal of Hydraulic Research* **55**(1), 72–84.
739 <https://doi.org/10.1080/00221686.2016.1217947>
- 740 Bazin, P.-H., Nakagawa, H., Kawaike, K., Paquier, A., Mignot, E. (2014). Modeling Flow Exchanges
741 between a Street and an Underground Drainage Pipe during Urban Floods. *Journal of Hydraulic*
742 *Engineering* **140**(10), 04014051. [https://doi.org/10.1061/\(asce\)hy.1943-7900.0000917](https://doi.org/10.1061/(asce)hy.1943-7900.0000917)
- 743 Bernardini, G., Quagliarini, E., D’Orazio, M., Brocchini, M. (2020). Towards the simulation of flood
744 evacuation in urban scenarios: Experiments to estimate human motion speed in floodwaters.
745 *Safety Science* **123**, 104563. <https://doi.org/10.1016/j.ssci.2019.104563>
- 746 Birkmann, J., Welle, T., Solecki, W., Lwasa, S., Garschagen, M. (2016). Boost resilience of small and
747 mid-sized cities. *Nature* **537**(7622), 605–608. <https://doi.org/10.1038/537605a>
- 748 Brown, R., Chanson, H. (2013). Turbulence and Suspended Sediment Measurements in an Urban
749 Environment during the Brisbane River Flood of January 2011. *Journal of Hydraulic Engineering*
750 **139**(2), 244–253. [https://doi.org/10.1061/\(asce\)hy.1943-7900.0000666](https://doi.org/10.1061/(asce)hy.1943-7900.0000666)
- 751 Bruwier, M., Ercicum, S., Archambeau, P., Pirotton, M., Dewals, B. (2017). Discussion of: Computing
752 flooding of crossroads with obstacles using a 2D numerical model. *Journal of Hydraulic*
753 *Research* **55**(5), 737–741. <https://doi.org/10.1080/00221686.2017.1326406>
- 754 Bruwier, M., Maravat, C., Mustafa, A., Teller, J., Pirotton, M., Ercicum, S., Archambeau, P., Dewals, B.
755 (2020). Influence of urban forms on surface flow in urban pluvial flooding. *Journal of Hydrology*
756 **582**, 124493. <https://doi.org/10.1016/j.jhydrol.2019.124493>
- 757 Camnasio, E., Ercicum, S., Archambeau, P., Pirotton, M., Dewals, B. (2014). Prediction of mean and
758 turbulent kinetic energy in rectangular shallow reservoirs. *Engineering Applications of*
759 *Computational Fluid Mechanics* **8**(4), 586–597.
760 <https://doi.org/10.1080/19942060.2014.11083309>
- 761 Chang, T.-J., Wang, C.-H., Chen, A. S., Djordjevic, S. (2018). The effect of inclusion of inlets in dual
762 drainage modelling. *Journal of Hydrology* **559**, 541–555.
763 <https://doi.org/10.1016/j.jhydrol.2018.01.066>

764 Chen, D., Acharya, K., Stone, M. (2010). Sensitivity Analysis of Nonequilibrium Adaptation Parameters
765 for Modeling Mining-Pit Migration. *Journal of Hydraulic Engineering* **136**(10), 806–811.
766 [https://doi.org/10.1061/\(asce\)hy.1943-7900.0000242](https://doi.org/10.1061/(asce)hy.1943-7900.0000242)

767 Chen, S., Huang, Q., Muttarak, R., Fang, J., Liu, T., He, C., Liu, Z., Zhu, L. (2022). Updating global
768 urbanization projections under the Shared Socioeconomic Pathways. *Scientific Data* **9**(137).
769 <https://doi.org/10.1038/s41597-022-01209-5>

770 Chen, W., Wang, X., Deng, S., Liu, C., Xie, H., Zhu, Y. (2019). Integrated urban flood vulnerability
771 assessment using local spatial dependence-based probabilistic approach. *Journal of Hydrology*
772 **575**, 454–469. <https://doi.org/10.1016/j.jhydrol.2019.05.043>

773 Chen, Y., Zhou, H., Zhang, H., Du, G., Zhou, J. (2015). Urban flood risk warning under rapid
774 urbanization. *Environmental Research* **139**, 3–10. <https://doi.org/10.1016/j.envres.2015.02.028>

775 Costabile, P., Costanzo, C., Lorenzo, G. D., Macchione, F. (2020). Is local flood hazard assessment in
776 urban areas significantly influenced by the physical complexity of the hydrodynamic inundation
777 model? *Journal of Hydrology* **580**, 124231. <https://doi.org/10.1016/j.jhydrol.2019.124231>

778 Dewals, B., Bruwier, M., Piroton, M., Erpicum, S., Archambeau, P. (2021). Porosity Models for Large-
779 Scale Urban Flood Modelling: A Review. *Water* **13**(7), 960. <https://doi.org/10.3390/w13070960>

780 Dewals, B., Erpicum, S., Archambeau, P., Piroton, M. (2012). Discussion of: Experimental study of
781 velocity fields in rectangular shallow reservoirs. *Journal of Hydraulic Research* **50**(4), 435–436.
782 <https://doi.org/10.1080/00221686.2012.702856>

783 Doocy, S., Daniels, A., Murray, S., Kirsch, T. D. (2013). The Human Impact of Floods: a Historical
784 Review of Events 1980-2009 and Systematic Literature Review. *PLoS Currents*.
785 <https://doi.org/10.1371/currents.dis.f4deb457904936b07c09daa98ee8171a>

786 Dottori, F., Figueiredo, R., Martina, M. L. V., Molinari, D., Scorzini, A. R. (2016). INSYDE: a synthetic,
787 probabilistic flood damage model based on explicit cost analysis. *Natural Hazards and Earth*
788 *System Sciences* **16**(12), 2577–2591. <https://doi.org/10.5194/nhess-16-2577-2016>

789 El Kadi Abderrezzak, K., Lewicki, L., Paquier, A., Rivière, N., Travin, G. (2011). Division of critical
790 flow at three-branch open-channel intersection. *Journal of Hydraulic Research* **49**(2), 231–238.
791 <https://doi.org/10.1080/00221686.2011.558174>

792 El Kadi Abderrezzak, K., Paquier, A. (2009). Discussion of “Numerical and Experimental Study of
793 Dividing Open-Channel Flows” by A. S. Ramamurthy, Junying Qu, and Diep Vo. *Journal of*
794 *Hydraulic Engineering* **135**(12), 1111–1112. [https://doi.org/10.1061/\(asce\)hy.1943-7900.0000009](https://doi.org/10.1061/(asce)hy.1943-7900.0000009)

795 Erpicum, S., Dewals, B. J., Archambeau, P., Piroton, M. (2010). Dam break flow computation based on
796 an efficient flux vector splitting. *Journal of Computational and Applied Mathematics* **234**(7),
797 2143–2151. <https://doi.org/10.1016/j.cam.2009.08.110>

798 Erpicum, S., Meile, T., Dewals, B. J., Piroton, M., Schleiss, A. J. (2009). 2D numerical flow modeling in
799 a macro-rough channel. *International Journal for Numerical Methods in Fluids* **61**(11), 1227–
800 1246. <https://doi.org/10.1002/flid.2002>

801 Fujita, I., Muste, M., Kruger, A. (1998). Large-scale particle image velocimetry for flow analysis in
802 hydraulic engineering applications. *Journal of Hydraulic Research* **36**(3), 397–414.
803 <https://doi.org/10.1080/00221689809498626>

804 Gems, B., Mazzorana, B., Hofer, T., Sturm, M., Gabl, R., Aufleger, M. (2016). 3-D hydrodynamic
805 modelling of flood impacts on a building and indoor flooding processes. *Natural Hazards and*
806 *Earth System Sciences* **16**(6), 1351–1368. <https://doi.org/10.5194/nhess-16-1351-2016>

807 Gross, M. (2016). The urbanisation of our species. *Current Biology* **26**(23), R1205–R1208.
808 <https://doi.org/10.1016/j.cub.2016.11.039>

809 Guo, K., Guan, M., Yu, D. (2021). Urban surface water flood modelling – a comprehensive review of
810 current models and future challenges. *Hydrology and Earth System Sciences* **25**(5), 2843–2860.
811 <https://doi.org/10.5194/hess-25-2843-2021>

812

813 Haltas, I., Tayfur, G., Elci, S. (2016). Two-dimensional numerical modeling of flood wave propagation in
814 an urban area due to Ürkmez dam-break, Izmir, Turkey. *Natural Hazards* **81**(3), 2103–2119.
815 <https://doi.org/10.1007/s11069-016-2175-6>

816 Heller, V. (2011). Scale effects in physical hydraulic engineering models. *Journal of Hydraulic Research*
817 **49**(3), 293–306. <https://doi.org/10.1080/00221686.2011.578914>

818 Hettiarachchi, S., Wasko, C., Sharma, A. (2018). Increase in flood risk resulting from climate change in a
819 developed urban watershed – the role of storm temporal patterns. *Hydrology and Earth System*
820 *Sciences* **22**(3), 2041–2056. <https://doi.org/10.5194/hess-22-2041-2018>

821 Huang, J., Weber, L. J., Lai, Y. G. (2002). Three-Dimensional Numerical Study of Flows in Open-
822 Channel Junctions. *Journal of Hydraulic Engineering* **128**(3), 268–280.
823 [https://doi.org/10.1061/\(asce\)0733-9429\(2002\)128:3\(268\)](https://doi.org/10.1061/(asce)0733-9429(2002)128:3(268))

824 Huggel, C., Stone, D., Auffhammer, M., Hansen, G. (2013). Loss and damage attribution. *Nature Climate*
825 *Change* **3**(8), 694–696. <https://doi.org/10.1038/nclimate1961>

826 Idel’cik, I. E. (1969). Mémento des pertes de charge. Eyrolles (translated to French by Meury M).

827 Jongman, B. (2018). Effective adaptation to rising flood risk. *Nature Communications* **9**, 1986.
828 <https://doi.org/10.1038/s41467-018-04396-1>

829 Khan, A. A., Cadavid, R., Wang, S. S.-Y. (2000). Simulation of channel confluence and bifurcation using
830 the CCHE2D model. *Proceedings of the Institution of Civil Engineers - Water and Maritime*
831 *Engineering* **142**(2), 97–102. <https://doi.org/10.1680/wame.2000.142.2.97>

832 Kitsikoudis, V., Becker, B. P. J., Huismans, Y., Archambeau, P., Erpicum, S., Piroton, M., Dewals, B.
833 (2020). Discrepancies in Flood Modelling Approaches in Transboundary River Systems: Legacy
834 of the Past or Well-grounded Choices? *Water Resources Management* **34**(11), 3465–3478.
835 <https://doi.org/10.1007/s11269-020-02621-5>

836 Kitsikoudis, V., Erpicum, S., Rubinato, M., Shucksmith, J. D., Archambeau, P., Piroton, M., Dewals, B.
837 (2021). Exchange between drainage systems and surface flows during urban flooding: Quasi-
838 steady and dynamic modelling in unsteady flow conditions. *Journal of Hydrology* **602**, 126628.
839 <https://doi.org/10.1016/j.jhydrol.2021.126628>

840 Kreibich, H., Bergh, J. C. J. M. van den, Bouwer, L. M., Bubeck, P., Ciavola, P., Green, C., Hallegatte,
841 S., Logar, I., Meyer, V., Schwarze, R., Thielen, A. H. (2014). Costing natural hazards. *Nature*
842 *Climate Change* **4**(5), 303–306. <https://doi.org/10.1038/nclimate2182>

843 Kreibich, H., Piroth, K., Seifert, I., Maiwald, H., Kunert, U., Schwarz, J., Merz, B., Thielen, A. H.
844 (2009). Is flow velocity a significant parameter in flood damage modelling? *Natural Hazards and*
845 *Earth System Sciences* **9**(5), 1679–1692. <https://doi.org/10.5194/nhess-9-1679-2009>

846 Leandro, J., Schumann, A., Pfister, A. (2016). A step towards considering the spatial heterogeneity of
847 urban key features in urban hydrology flood modelling. *Journal of Hydrology* **535**, 356–365.
848 <https://doi.org/10.1016/j.jhydrol.2016.01.060>

849 Li, X., Erpicum, S., Mignot, E., Archambeau, P., Piroton, M., Dewals, B. (2021a). Influence of urban
850 forms on long-duration urban flooding: Laboratory experiments and computational analysis.
851 *Journal of Hydrology* **603**, 127034. <https://doi.org/10.1016/j.jhydrol.2021.127034>

852 Li, X., Erpicum, S., Mignot, E., Archambeau, P., Rivière, N., Piroton, M., Dewals, B. (2020). Numerical
853 Insights Into the Effects of Model Geometric Distortion in Laboratory Experiments of Urban
854 Flooding. *Water Resources Research* **56**(7), e2019WR026774.
855 <https://doi.org/10.1029/2019wr026774>

856 Li, X., Kitsikoudis, V., Mignot, E., Archambeau, P., Piroton, M., Dewals, B., Erpicum, S. (2021b).
857 Experimental and Numerical Study of the Effect of Model Geometric Distortion on Laboratory
858 Modeling of Urban Flooding. *Water Resources Research* **57**(10), e2021WR029666.
859 <https://doi.org/10.1029/2021wr029666>

860 Lin, J., He, X., Lu, S., Liu, D., He, P. (2021). Investigating the influence of three-dimensional building
861 configuration on urban pluvial flooding using random forest algorithm. *Environmental Research*
862 **196**, 110438. <https://doi.org/10.1016/j.envres.2020.110438>

863 Liu, L., Sun, J., Lin, B., Lu, L. (2018). Building performance in dam-break flow – an experimental study.
864 *Urban Water Journal* **15**(3), 251–258. <https://doi.org/10.1080/1573062x.2018.1433862>

865 Luo, H., Fytanidis, D. K., Schmidt, A. R., Garcia, M. H. (2018). Comparative 1D and 3D numerical
866 investigation of open-channel junction flows and energy losses. *Advances in Water Resources*
867 **117**, 120–139. <https://doi.org/10.1016/j.advwatres.2018.05.012>

868 Luo, P., Luo, M., Li, F., Qi, X., Huo, A., Wang, Z., He, B., Takara, K., Nover, D., Wang, Y. (2022).
869 Urban flood numerical simulation: Research, methods and future perspectives. *Environmental*
870 *Modelling and Software* **156**, 105478. <https://doi.org/10.1016/j.envsoft.2022.105478>

871 Lv, H., Wu, Z., Meng, Y., Guan, X., Wang, H., Zhang, X., Ma, B. (2022). Optimal Domain Scale for
872 Stochastic Urban Flood Damage Assessment Considering Triple Spatial Uncertainties. *Water*
873 *Resources Research* **58**(7), e2021WR031552. <https://doi.org/10.1029/2021wr031552>

874 Martinez-Gomariz, E., Forero-Ortiz, E., Russo, B., Locatelli, L., Guerrero-Hidalga, M., Yubero, D.,
875 Castan, S. (2021). A novel expert opinion-based approach to compute estimations of flood
876 damage to property in dense urban environments. Barcelona case study. *Journal of Hydrology*
877 **598**, 126244. <https://doi.org/10.1016/j.jhydrol.2021.126244>

878 Martinez-Gomariz, E., Gómez, M., Russo, B., Djordjevic, S. (2018). Stability criteria for flooded
879 vehicles: a state-of-the-art review. *Journal of Flood Risk Management* **11**, S817–S826.
880 <https://doi.org/10.1111/jfr3.12262>

881 Mejia-Morales, M. A., Mignot, E., Paquier, A., Proust, S. (2022a). Laboratory investigation into the effect
882 of the storage capacity of a city block on unsteady urban flood flows. *Water Resources Research*
883 **(under review)**.

884 Mejia-Morales, M. A., Mignot, E., Paquier, A., Proust, S. (2022b). Data set of a laboratory experiment on
885 the impact of the conveyance porosity of an urban block on the flood risk assessment. Recherche
886 Data Gouv, UNF:6:Md2Yh9DNuCDyR13U3kNGCw== [fileUNF].
887 <https://doi.org/10.57745/UJOCJ8>

888 Mejia-Morales, M. A., Mignot, E., Paquier, A., Sigaud, D., Proust, S. (2021). Impact of the porosity of an
889 urban block on the flood risk assessment: A laboratory experiment. *Journal of Hydrology* **602**,
890 126715. <https://doi.org/10.1016/j.jhydrol.2021.126715>

891 Mejia-Morales, M. A., Proust, S., Mignot, E., Paquier, A. (2020). Experimental and Numerical Modelling
892 of the Influence of Street-Block Flow Exchanges During Urban Floods, in: *Advances*
893 *Hydroinformatics*. Springer Singapore, 495–505. https://doi.org/10.1007/978-981-15-5436-0_39

894 Mignot, E., Camusson, L., Riviere, N. (2020). Measuring the flow intrusion towards building areas during
895 urban floods: Impact of the obstacles located in the streets and on the facade. *Journal of*
896 *Hydrology* **583**, 124607. <https://doi.org/10.1016/j.jhydrol.2020.124607>

897 Mignot, E., Dewals, B. (2022). Hydraulic modelling of inland urban flooding: Recent advances. *Journal*
898 *of Hydrology* **609**, 127763. <https://doi.org/10.1016/j.jhydrol.2022.127763>

899 Mignot, E., Li, X., Dewals, B. (2019). Experimental modelling of urban flooding: A review. *Journal of*
900 *Hydrology* **568**, 334–342. <https://doi.org/10.1016/j.jhydrol.2018.11.001>

901 Mignot, E., Paquier, A., Haider, S. (2006). Modeling floods in a dense urban area using 2D shallow water
902 equations. *Journal of Hydrology* **327**(1-2), 186–199.
903 <https://doi.org/10.1016/j.jhydrol.2005.11.026>

904 Mignot, E., Paquier, A., Rivière, N. (2008). Experimental and numerical modeling of symmetrical four-
905 branch supercritical cross junction flow. *Journal of Hydraulic Research* **46**(6), 723–738.
906 <https://doi.org/10.1080/00221686.2008.9521918>

907 Mignot, E., Zeng, C., Dominguez, G., Li, C.-W., Rivière, N., Bazin, P.-H. (2013). Impact of topographic
908 obstacles on the discharge distribution in open-channel bifurcations. *Journal of Hydrology* **494**,
909 10–19. <https://doi.org/10.1016/j.jhydrol.2013.04.023>

910 Neal, J. C., Bates, P. D., Fewtrell, T. J., Hunter, N. M., Wilson, M. D., Horritt, M. S. (2009). Distributed
911 whole city water level measurements from the Carlisle 2005 urban flood event and comparison
912 with hydraulic model simulations. *Journal of Hydrology* **368**(1-4), 42–55.
913 <https://doi.org/10.1016/j.jhydrol.2009.01.026>

914 Neary, V. S., Sotiropoulos, F., Odgaard, A. J. (1999). Three-Dimensional Numerical Model of Lateral-
915 Intake Inflows. *Journal of Hydraulic Engineering* **125**(2), 126–140.
916 [https://doi.org/10.1061/\(asce\)0733-9429\(1999\)125:2\(126\)](https://doi.org/10.1061/(asce)0733-9429(1999)125:2(126))

917 Ozdemir, H., Sampson, C. C., Almeida, G. A. M. de, Bates, P. D. (2013). Evaluating scale and roughness
918 effects in urban flood modelling using terrestrial LIDAR data. *Hydrology and Earth System*
919 *Sciences* **17**(10), 4015–4030. <https://doi.org/10.5194/hess-17-4015-2013>

920 Perks, M. T., Russell, A. J., Large, A. R. G. (2016). Technical Note: Advances in flash flood monitoring
921 using unmanned aerial vehicles (UAVs). *Hydrology and Earth System Sciences* **20**(10), 4005–
922 4015. <https://doi.org/10.5194/hess-20-4005-2016>

923 Pfahl, S., O’Gorman, P. A., Fischer, E. M. (2017). Understanding the regional pattern of projected future
924 changes in extreme precipitation. *Nature Climate Change* **7**(6), 423–427.
925 <https://doi.org/10.1038/nclimate3287>

926 Postacchini, M., Bernardini, G., D’Orazio, M., Quagliarini, E. (2021). Human stability during floods:
927 Experimental tests on a physical model simulating human body. *Safety Science* **137**, 105153.
928 <https://doi.org/10.1016/j.ssci.2020.105153>

929 Qi, W., Ma, C., Xu, H., Zhao, K., Chen, Z. (2022). A comprehensive analysis method of spatial
930 prioritization for urban flood management based on source tracking. *Ecological Indicators* **135**,
931 108565. <https://doi.org/10.1016/j.ecolind.2022.108565>

932 Ramamurthy, A. S., Qu, J., Vo, D. (2007). Numerical and Experimental Study of Dividing Open-Channel
933 Flows. *Journal of Hydraulic Engineering* **133**(10), 1135–1144.
934 [https://doi.org/10.1061/\(asce\)0733-9429\(2007\)133:10\(1135\)](https://doi.org/10.1061/(asce)0733-9429(2007)133:10(1135))

935 Re, M., Kazimierski, L. D., Garcia, P. E., Ortiz, N. E., Lagos, M. (2022). Assessment of crowdsourced
936 social media data and numerical modelling as complementary tools for urban flood mitigation.
937 *Hydrological Sciences Journal* **67**(9), 1295–1308.
938 <https://doi.org/10.1080/02626667.2022.2075266>

939 Rodi, W. (2017). Turbulence Modeling and Simulation in Hydraulics: A Historical Review. *Journal of*
940 *Hydraulic Engineering* **143**(5), 03117001. [https://doi.org/10.1061/\(asce\)hy.1943-7900.0001288](https://doi.org/10.1061/(asce)hy.1943-7900.0001288)

941 Roger, S., Dewals, B. J., Erpicum, S., Schwanenberg, D., Schüttrumpf, H., Köngeter, J., Piroton, M.
942 (2009). Experimental and numerical investigations of dike-break induced flows. *Journal of*
943 *Hydraulic Research* **47**(3), 349–359. <https://doi.org/10.1080/00221686.2009.9522006>

944 Rosenzweig, B. R., Cantis, P. H., Kim, Y., Cohn, A., Grove, K., Brock, J., Yesuf, J., Mistry, P., Welty,
945 C., McPhearson, T., Sauer, J., Chang, H. (2021). The Value of Urban Flood Modeling. *Earth’s*
946 *Future* **9**(1), e2020EF001739. <https://doi.org/10.1029/2020ef001739>

947 Rubinato, M., Helms, L., Vanderlinden, M., Hart, J., Martins, R. (2022). Flow exchange, energy losses
948 and pollutant transport in a surcharging manhole linked to street profiles. *Journal of Hydrology*
949 **604**, 127201. <https://doi.org/10.1016/j.jhydrol.2021.127201>

950 Sanderson, B. M., Wobus, C., Mills, D., Zarakas, C., Crimmins, A., Sarofim, M. C., Weaver, C. (2019).
951 Informing Future Risks of Record-Level Rainfall in the United States. *Geophysical Research*
952 *Letters* **46**(7), 3963–3972. <https://doi.org/10.1029/2019gl082362>

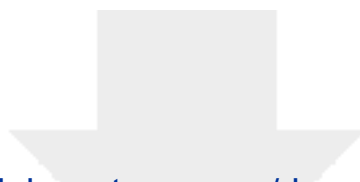
953 Schindfessel, L., Creëlle, S., Mulder, T. D. (2015). Flow Patterns in an Open Channel Confluence with
954 Increasingly Dominant Tributary Inflow. *Water* **7**(9), 4724–4751.
955 <https://doi.org/10.3390/w7094724>

956 Shettar, A. S., Murthy, K. K. (1996). A numerical study of division of flow in open channels. *Journal of*
957 *Hydraulic Research* **34**(5), 651–675. <https://doi.org/10.1080/00221689609498464>

958 Smith, G. P., Modra, B. D., Felder, S. (2019). Full-scale testing of stability curves for vehicles in flood
959 waters. *Journal of Flood Risk Management* **12**(S2). <https://doi.org/10.1111/jfr3.12527>

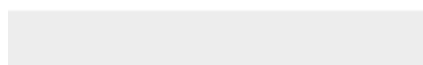
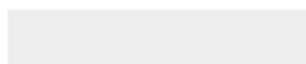
960 Sturm, M., Gems, B., Keller, F., Mazzorana, B., Fuchs, S., Papatoma-Köhle, M., Aufleger, M. (2018).
961 Experimental analyses of impact forces on buildings exposed to fluvial hazards. *Journal of*
962 *Hydrology* **565**, 1–13. <https://doi.org/10.1016/j.jhydrol.2018.07.070>

963 Van Emelen, S., Soares-Frazão, S., Riahi-Nezhad, C. K., Chaudhry, M. H., Imran, J., Zech, Y. (2012).
964 Simulations of the New Orleans 17th Street Canal breach flood. *Journal of Hydraulic Research*
965 **50(1)**, 70–81. <https://doi.org/10.1080/00221686.2011.642578>
966 Wu, W. (2008). *Computational River Dynamics*. Taylor and Francis.
967 Wüthrich, D., Pfister, M., Schleiss, A. J. (2020). Forces on buildings with openings and orientation in a
968 steady post-tsunami free-surface flow. *Coastal Engineering* **161**, 103753.
969 <https://doi.org/10.1016/j.coastaleng.2020.103753>
970 Xia, J., Falconer, R. A., Wang, Y., Xiao, X. (2014). New criterion for the stability of a human body in
971 floodwaters. *Journal of Hydraulic Research* **52(1)**, 93–104.
972 <https://doi.org/10.1080/00221686.2013.875073>
973 Xia, J., Teo, F. Y., Lin, B., Falconer, R. A. (2011). Formula of incipient velocity for flooded vehicles.
974 *Natural Hazards* **58(1)**, 1–14. <https://doi.org/10.1007/s11069-010-9639-x>
975 Yalcin, E. (2020). Assessing the impact of topography and land cover data resolutions on two-
976 dimensional HEC-RAS hydrodynamic model simulations for urban flood hazard analysis.
977 *Natural Hazards* **101(3)**, 995–1017. <https://doi.org/10.1007/s11069-020-03906-z>
978 Yen, B. C. (2002). Open Channel Flow Resistance. *Journal of Hydraulic Engineering* **128(1)**, 20–39.
979 [https://doi.org/10.1061/\(asce\)0733-9429\(2002\)128:1\(20\)](https://doi.org/10.1061/(asce)0733-9429(2002)128:1(20))
980 Zhou, Q., Leng, G., Huang, M. (2018). Impacts of future climate change on urban flood volumes in
981 Hohhot in northern China: benefits of climate change mitigation and adaptations. *Hydrology and*
982 *Earth System Sciences* **22(1)**, 305–316. <https://doi.org/10.5194/hess-22-305-2018>
983 Zhou, Q., Yu, W., Chen, A. S., Jiang, C., Fu, G. (2016). Experimental Assessment of Building Blockage
984 Effects in a Simplified Urban District. *Procedia Engineering* **154**, 844–852.
985 <https://doi.org/10.1016/j.proeng.2016.07.448>
986
987



[Click here to access/download](#)

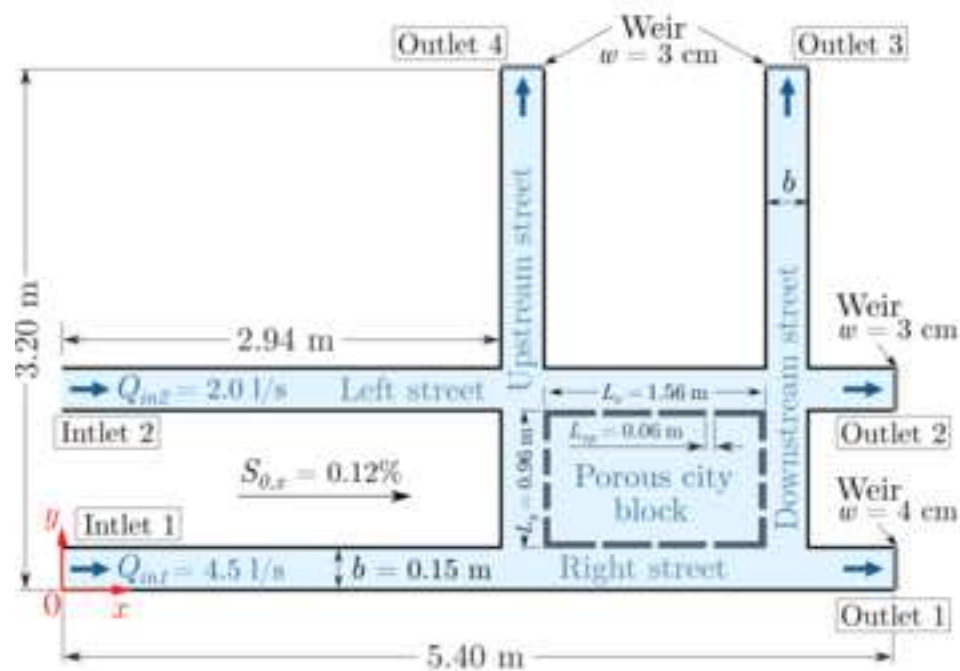
Supplementary material for on-line publication only
HYDROL48783_Supplement.pdf



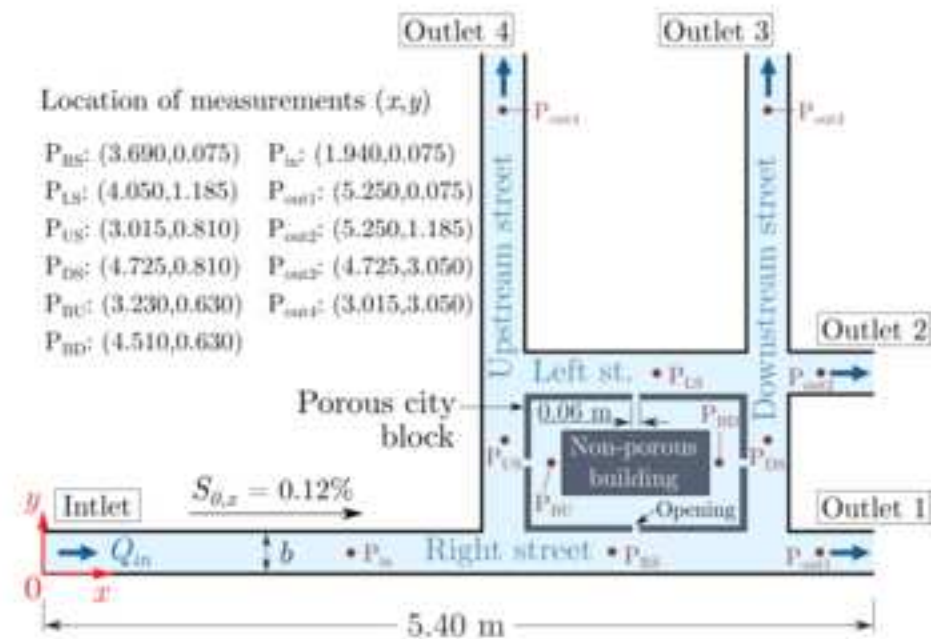
Authors' contributions

The study was designed by A.P., B.D., S.P., and E.M., who also defined the methodology; all laboratory experiments were conducted by M.M.M., under the supervision of S.P. and E.M.; computations with Model 1 were conducted by A.P. and those with Model 2 by students under the guidance of P.A., B.D., S.E., and M.P. The original draft of the manuscript was prepared by V.K. with the support of B.D., A.P., and M.M.M. It was revised by V.K., B.D., E.M. and S.P.

(a) Setup for steady flow experiments



(b) Setup for unsteady flow experiments



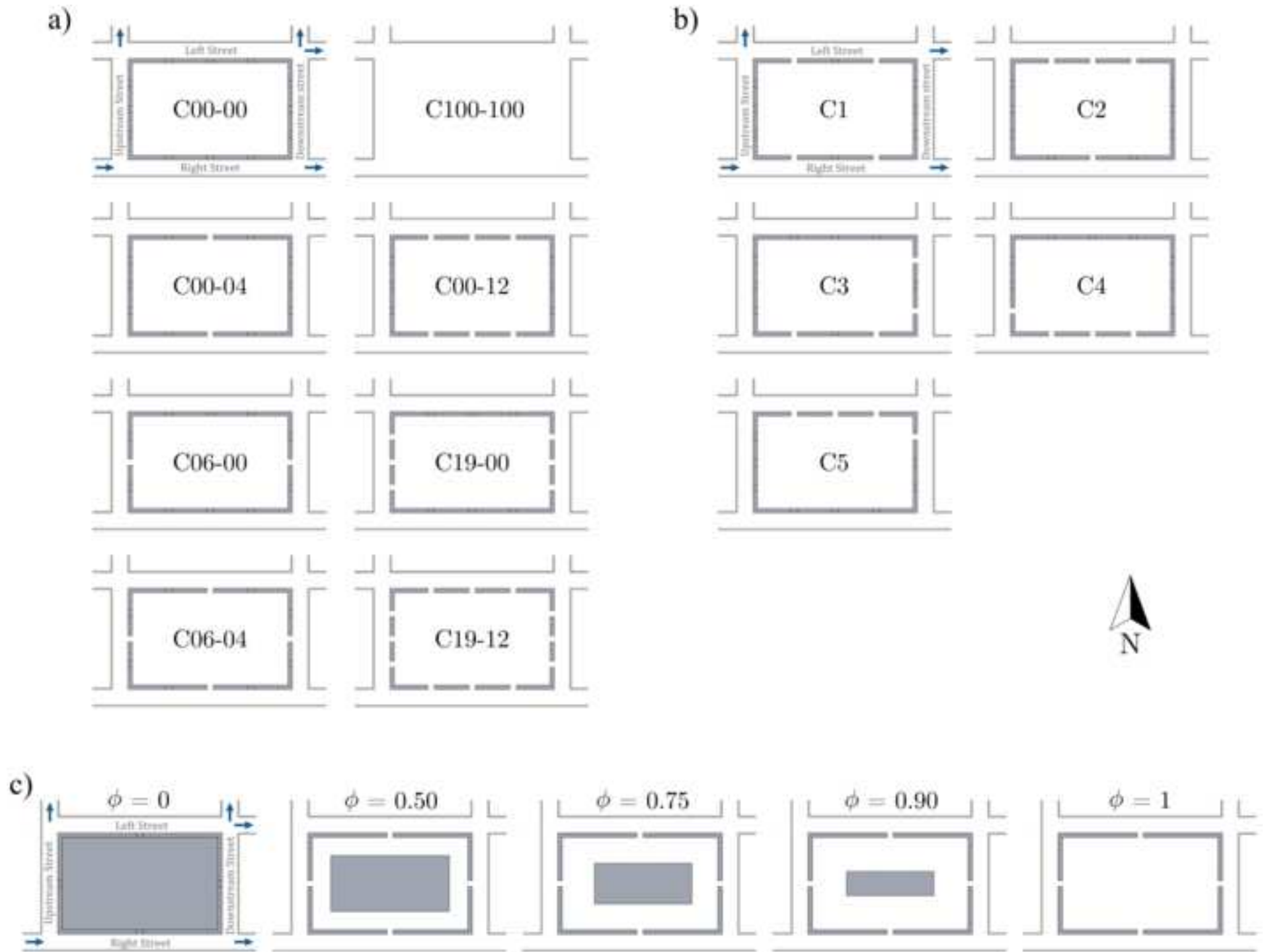
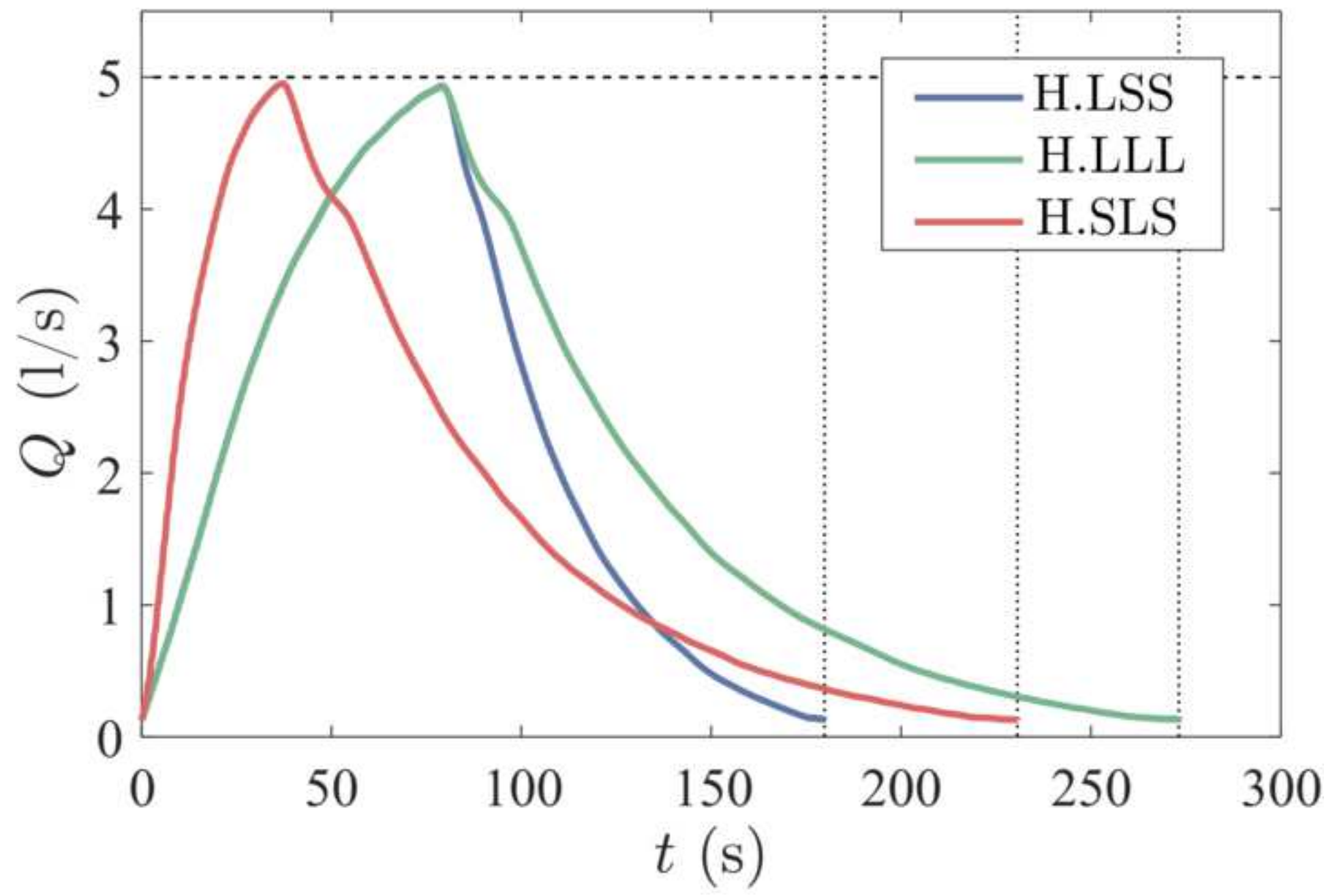
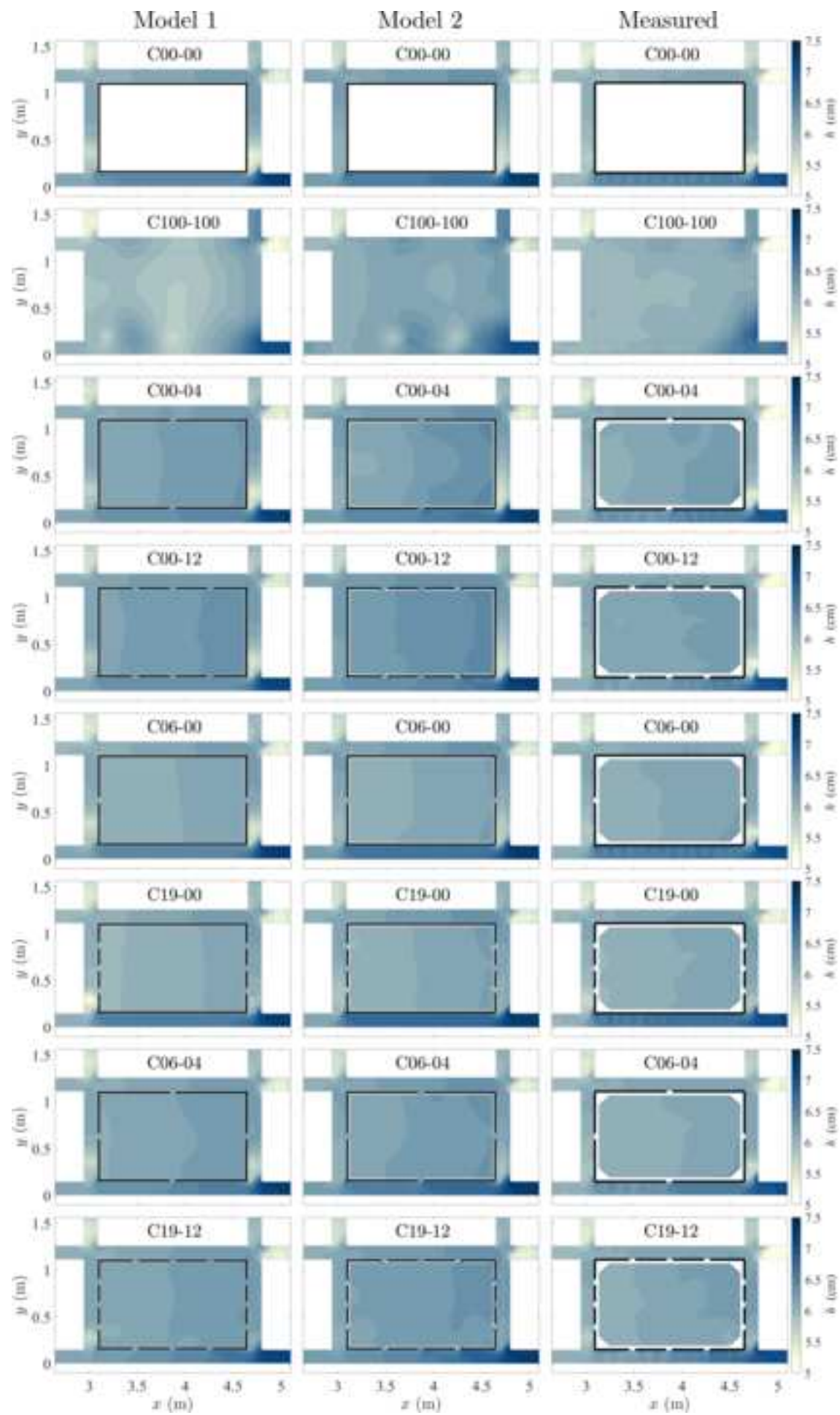
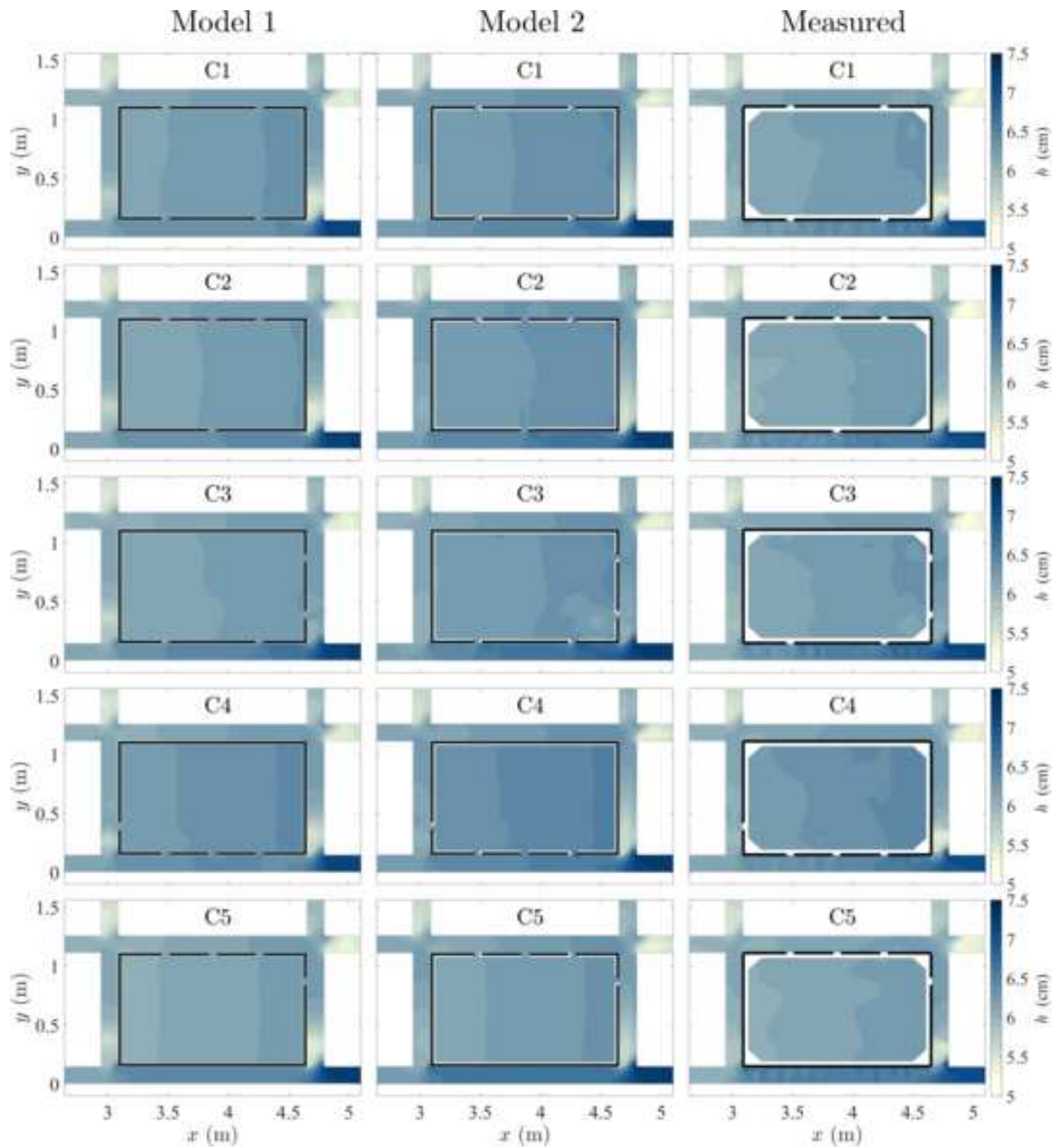
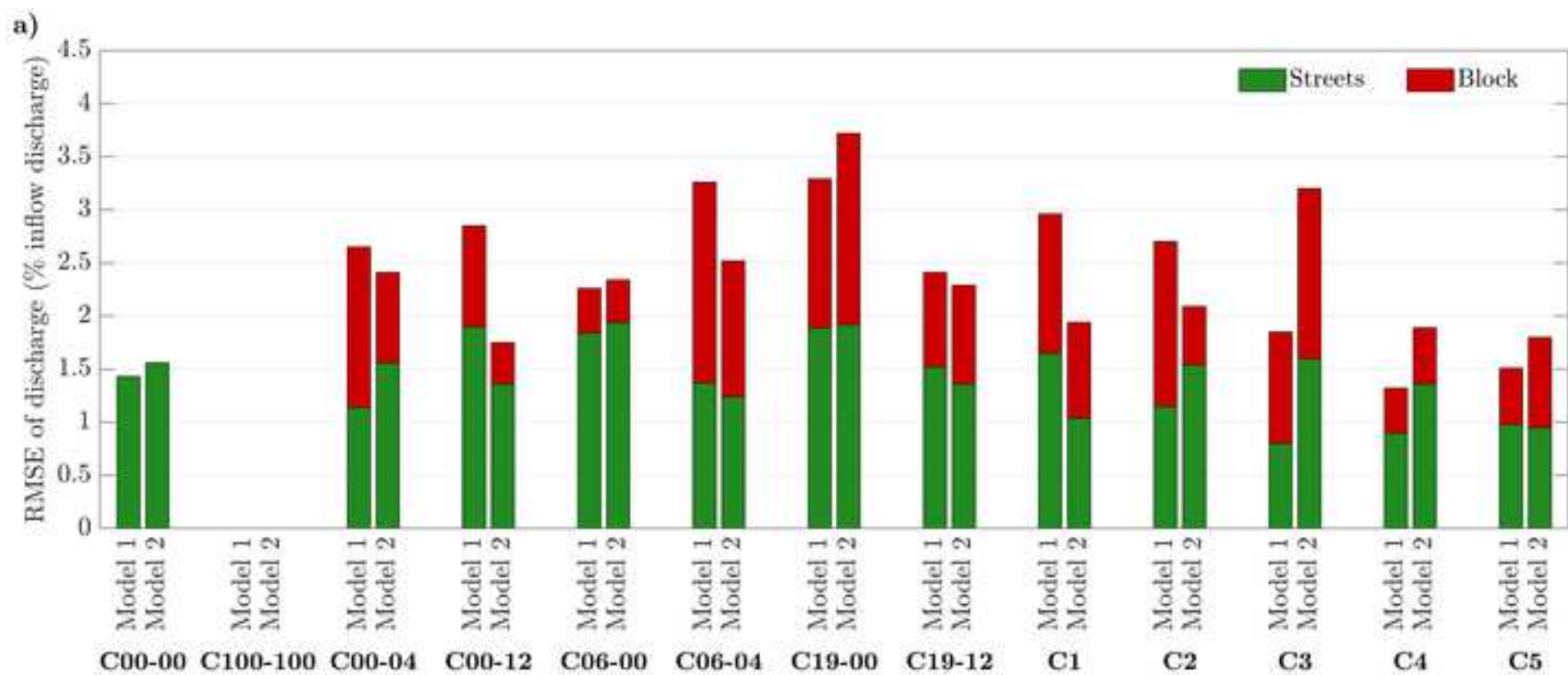


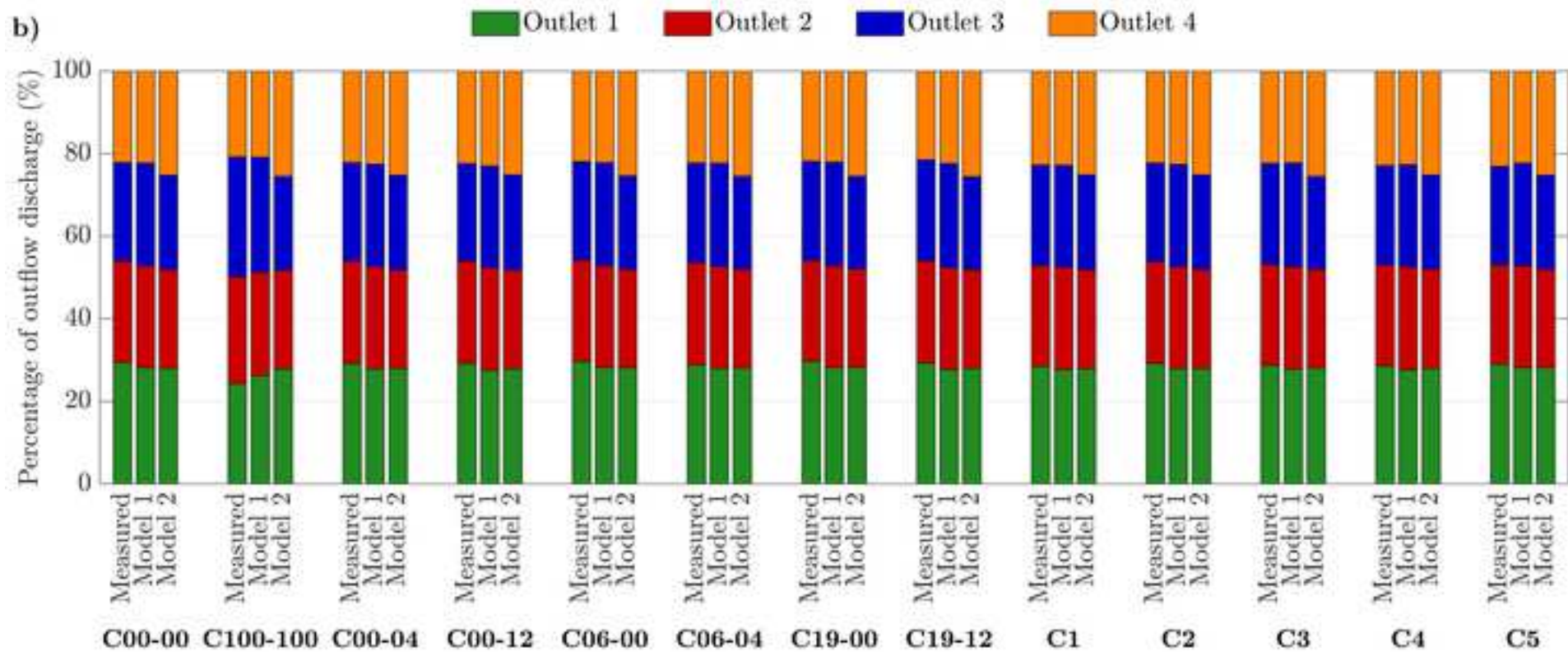
Figure 3

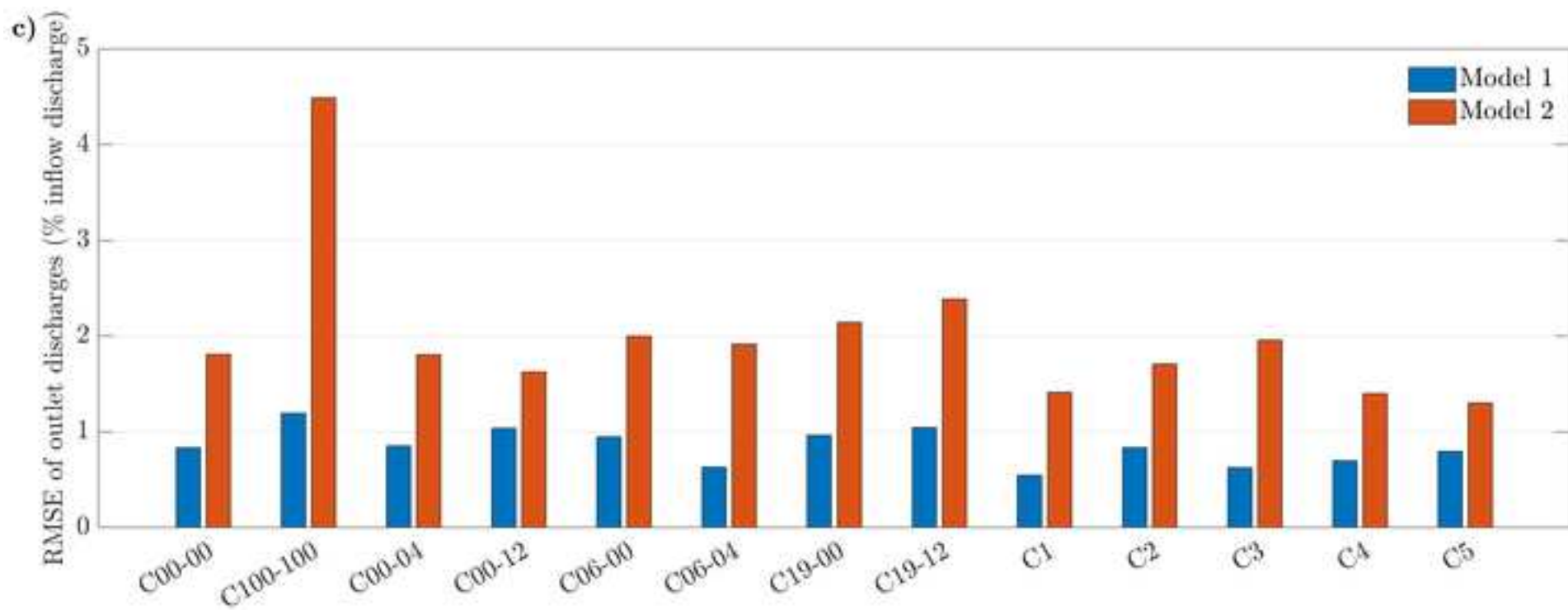


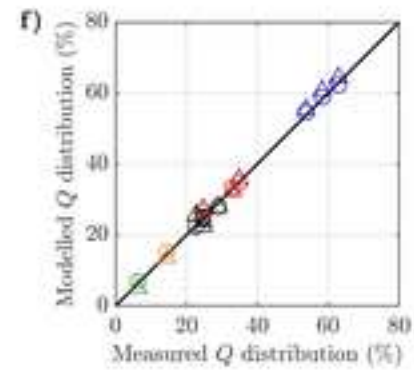
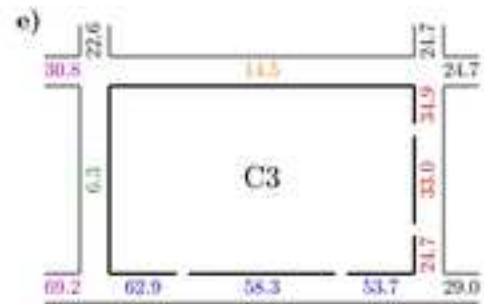
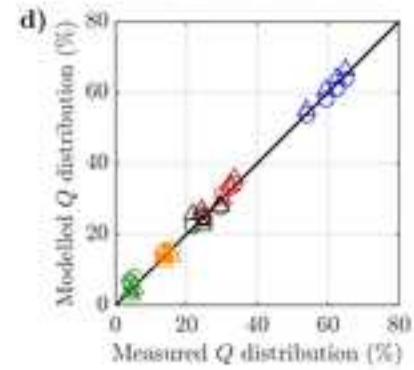
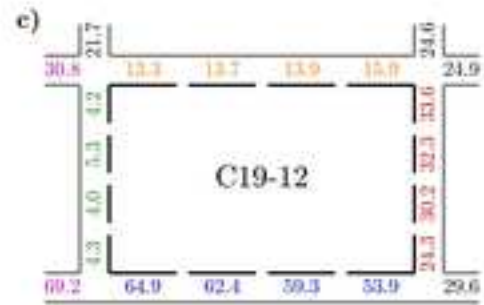
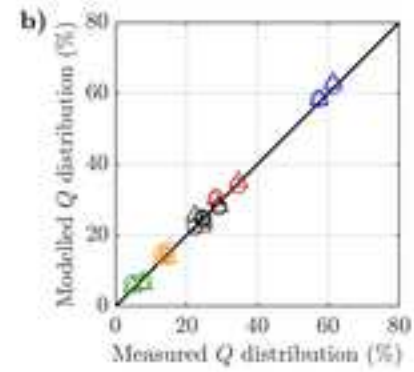
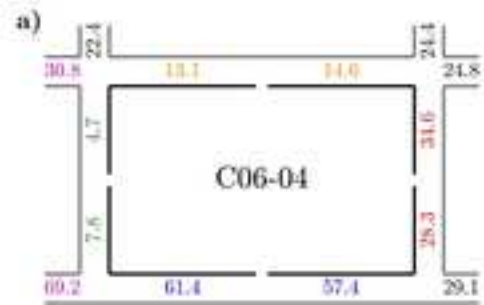


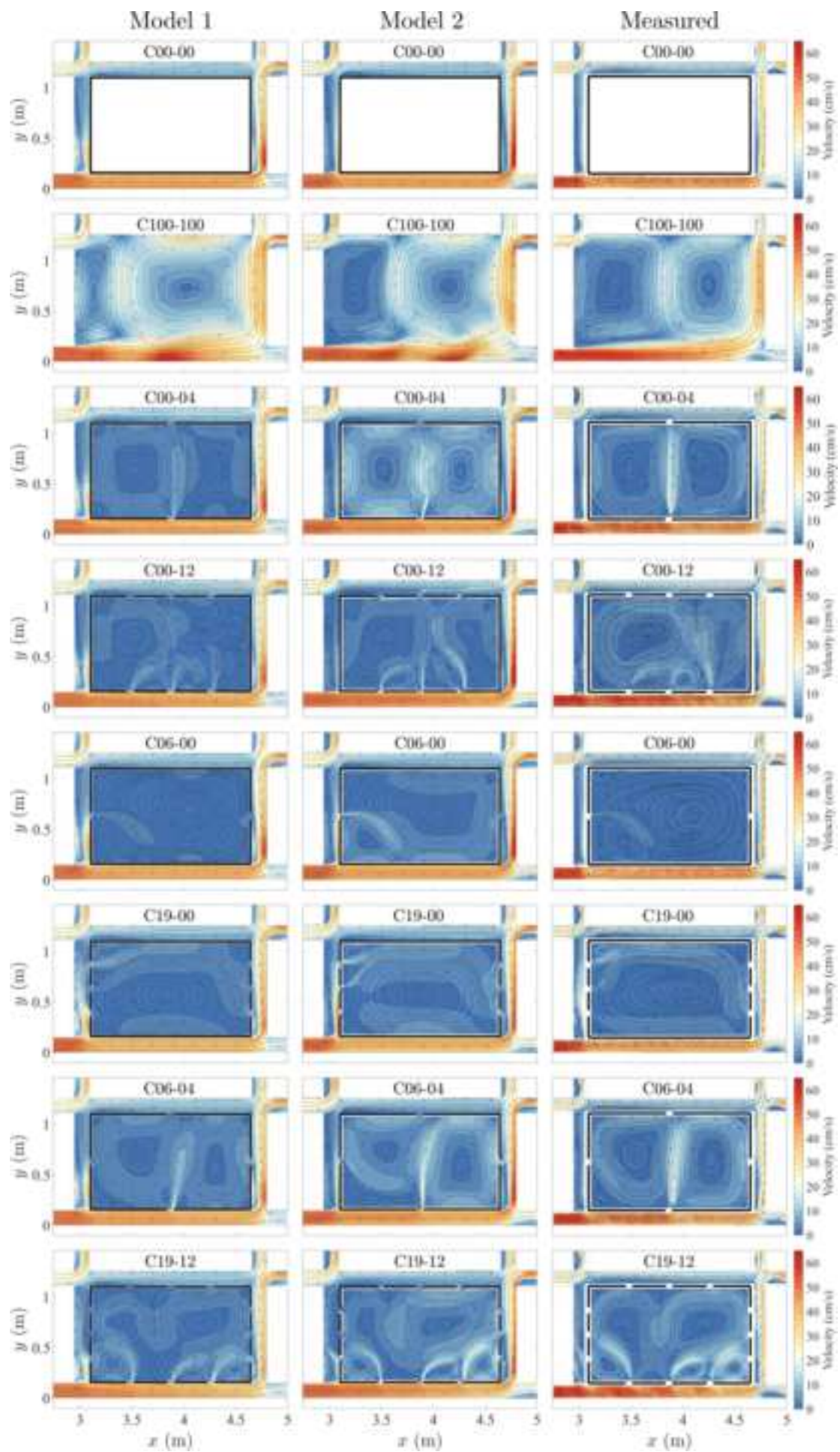


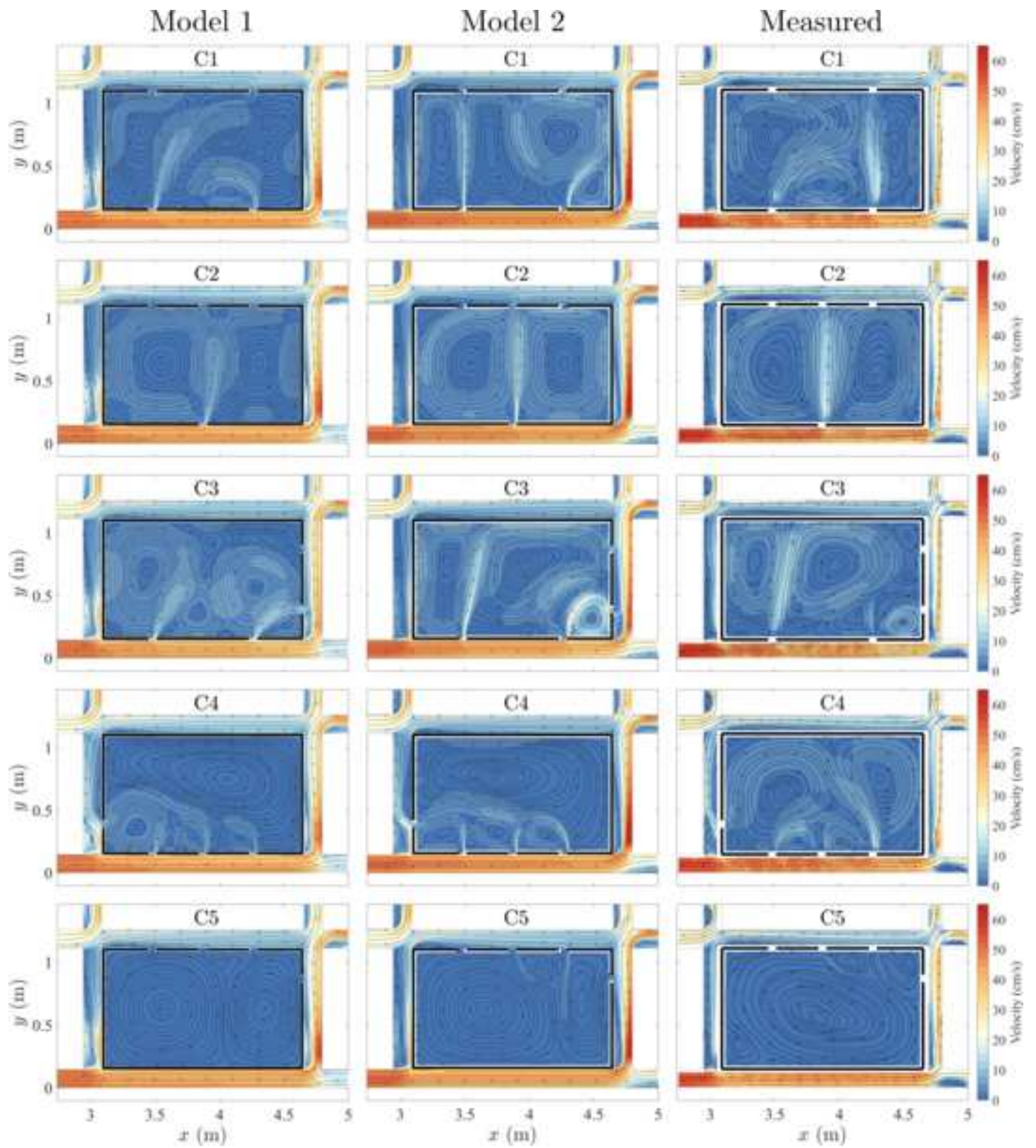












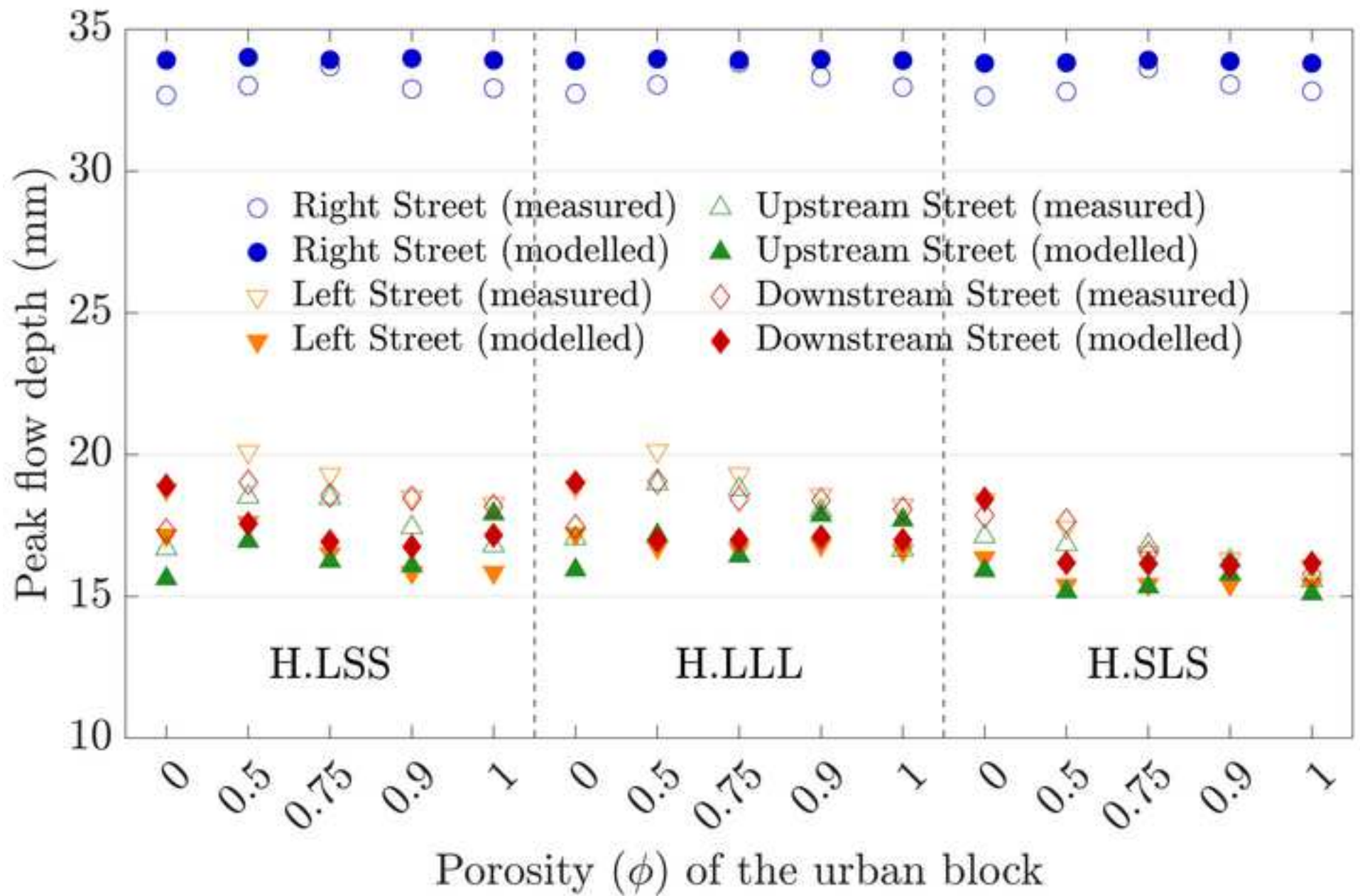


Figure 9

